

# **Development and characterization of a Fourier Transform based Quadrupole Ion Trap (FT-QIT) technique for process and residual gas analysis**

Dissertation submitted to the faculty 4 of the  
Bergische Universität Wuppertal in partial  
fulfillment of the requirements for the degree

**Doctor of Natural Science in Chemistry**  
**(Dr. rer. nat.)**

by

**M. Sc. Yessica Brachthäuser**

Wuppertal,  
May, 2017

Die Dissertation kann wie folgt zitiert werden:

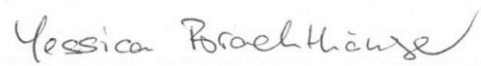
urn:nbn:de:hbz:468-20170717-144524-6

[<http://nbn-resolving.de/urn/resolver.pl?urn=urn%3Anbn%3Ade%3Ahbz%3A468-20170717-144524-6>]

## *Erklärung*

Ich versichere, dass ich die vorliegende Arbeit selbstständig im Arbeitskreis der Physikalischen und Theoretischen Chemie der Bergischen Universität Wuppertal unter der Anleitung von Prof. Dr. Thorsten Benter angefertigt und keine anderen als die angegebenen Quellen und Hilfsmittel verwendet habe.

Wuppertal, den 10.05.2017



Yessica Brachthäuser

Erstgutachter: Prof. Dr. Thorsten Benter

Zweitgutachter: Prof. Dr. Hans-Willi Kling



*Der Mensch muss bei dem Glauben verharren,  
daß das Unbegreifliche begreiflich sei:  
er würde sonst nicht forschen.*

*Johann Wolfgang von Goethe*



## *Acknowledgements*

Meinen ganz besonderen Dank möchte ich Prof. Dr. Thorsten Benter aussprechen, für die Möglichkeit in seiner Arbeitsgruppe und unter seiner Anleitung diese Doktorarbeit anzufertigen. Seine stets offene Tür und seine unfassbar positive Ausstrahlung haben mir während der gesamten Studienzzeit und insbesondere in der Promotionszeit sehr geholfen. Ich möchte mich bedanken für LEGO-Freude, interessante Diskussionen, eiskalte Ritas, Bälle über den Kickertisch jagen und eine einmalige Zeit als Teil der PTC.

Weiterhin gilt mein Dank:

... David Müller für die vielen gemeinsamen Stunden im Labor und im Büro, für geteilte Freude und geteiltes Leid im Hinblick auf die erzielten Messergebnisse.

... Dr. Hendrik Kersten für allzeit offene Ohren für Messergebnisse und die kritische Diskussion derselben, für interessante neue Ideen, für das Korrekturlesen dieser Arbeit und nicht zuletzt für das ehrgeizige Begleiten dieses Projektes.

... Dr. Klaus J. Brockmann†. Auf ein „Dankeschön“ würde ganz sicher ein „Dafür nicht!“ folgen. Vielen Dank für das Bereitstellen des Büros als Café Brockmann (das es bis in alle Ewigkeit geben wird), für jegliche organisatorische Hilfe sowie für so viele interessante Gespräche.

... Dr. Walter Wißdorf für die durchgeführten Simulationen sowie für seine kritische, aber interessierte Betrachtungsweise und den daraus folgenden sehr wertvollen Gesprächen.

... Ronald Giese für oft sehr spontane Hilfe bei zahlreichen technischen Fragen.

... Der Arbeitsgruppe der Physikalischen und Theoretischen Chemie, die meine Studien- und Promotionszeit zu einer unvergesslichen Zeit gemacht hat. Vielen Dank für viele intensive Diskussionen, eine wunderbare, familiäre Arbeitsatmosphäre sowie einmalige Aufenthalte in Minneapolis, Baltimore, St. Louis und San Antonio.

... Dem gesamten „GAMMA“-Team für die gute Zusammenarbeit sowie der Zeiss SMT GmbH für das entgegengebrachte Vertrauen in diesem Projekt und die Finanzierung meiner Promotionszeit.

... Prof. Dr. H.-W. Kling für die Übernahme des Zweitgutachtens dieser Arbeit.

... meiner Familie, die es mir überhaupt ermöglicht hat, diesen Weg zu gehen. Ihr habt mir immer den Rücken gestärkt, mir Vertrauen geschenkt und mich durch Höhen und Tiefen begleitet. Vielen Dank, dass ihr immer für mich da seid.





# Content

1.	<i>Aim of this work</i> .....	1
2.	<i>Introduction</i> .....	2
2.1.	<i>Mass Spectrometry</i> .....	2
2.1.1.	<i>General</i> .....	2
2.1.2.	<i>Ionization methods</i> .....	3
2.1.3.	<i>Miscellaneous mass analyzer systems</i> .....	7
2.1.4.	<i>Quadrupole based mass analyzer</i> .....	10
2.1.4.1	<i>Linear quadrupole instruments</i> .....	10
2.1.4.2	<i>Linear quadrupole ion traps</i> .....	13
2.1.4.3	<i>Three-dimensional quadrupole ion traps</i> .....	14
2.1.4.4.	<i>Detectors</i> .....	18
2.1.5.	<i>Fourier Transform based Mass Spectrometers</i> .....	20
2.1.5.1.	<i>Fourier Transformation</i> .....	20
2.1.5.2.	<i>Fourier transform Ion Cyclotron Resonance</i> .....	20
2.1.5.3.	<i>Orbitrap</i> .....	22
2.2.	<i>Semiconductors</i> .....	24
2.2.1.	<i>General: Basics and Applications</i> .....	25
2.2.2.	<i>Semiconductor manufacturing processes</i> .....	27
2.2.2.1.	<i>Bulk crystal growth and wafer fabrication</i> .....	27
2.2.2.2.	<i>Process flow in semiconductor fabrication</i> .....	28
2.2.2.3.	<i>Wafer inspection</i> .....	32
2.2.3.	<i>Zeiss SMT and semiconductor industry</i> .....	32
2.3.	<i>Zeiss-Project GAMMA: Gas multimode mass analyzer</i> .....	34
2.3.1.	<i>Required Specifications and operational parameters</i> .....	34
2.3.2.	<i>Fourier Transform Quadrupole Ion Trap</i> .....	35
2.3.2.1.	<i>Challenges: Electronics and first approaches</i> .....	35
2.3.2.1.	<i>Challenges: For analytical applications</i> .....	36
2.3.2.2.	<i>Advanced ion excitation schemes</i> .....	37
2.3.3.	<i>PTC and ipaMS within the project "GAMMA"</i> .....	38
3.	<i>Experimental</i> .....	39
3.1.	<i>Benchmarking instruments</i> .....	39
3.1.1.	<i>MKS Residual gas analyzer</i> .....	39

3.1.2.	<i>Time of Flight mass spectrometer (TOFWERK CTOF)</i> .....	41
3.2.	<i>FT-QIT: Zeiss Demotool</i> .....	46
3.2.1.	<i>Setup</i> .....	46
3.2.2.	<i>Gas inlet system</i> .....	47
3.2.3.	<i>Acquisition parameters</i> .....	48
3.2.3.1.	<i>Cycle Parameters</i> .....	48
3.2.3.2.	<i>Typical measurement sequence</i> .....	49
3.2.3.3.	<i>Further acquisition parameters</i> .....	50
3.2.4.	<i>Additional excitation schemes</i> .....	51
3.2.5.	<i>Measurement software: GammaProto</i> .....	52
3.2.6.	<i>Ion excitation</i> .....	54
3.2.7.	<i>Filament driven electron ionization</i> .....	55
3.2.8.	<i>Plasma coupling</i> .....	56
3.2.9.	<i>Measurements</i> .....	57
3.3.	<i>Analytes and sample preparation</i> .....	57
3.4.	<i>Simulations and data analysis</i> .....	58
4.	<i>Results and Discussion</i> .....	59
4.1.	<i>Basic FT QIT settings</i> .....	59
4.2.	<i>Variation of basic measurement parameters</i> .....	62
4.2.1.	<i>EI ion source</i> .....	62
4.2.2.	<i>Trapping field</i> .....	66
4.2.3.	<i>Rectangular ion excitation</i> .....	69
4.3.	<i>Physical-chemical effects on FT-QIT performance</i> .....	70
4.3.1.	<i>Space charge and ion suppression</i> .....	70
4.3.2.	<i>Ion molecule reactions affecting signal ratios</i> .....	76
4.3.3.	<i>Operation in pulsed gas mode, filament behavior</i> .....	78
4.4.	<i>Advanced excitation schemes</i> .....	79
4.5.	<i>Gas inlet: A crucial parameter</i> .....	85
4.5.1.	<i>Design I: Bended metal tube</i> .....	86
4.5.2.	<i>Design II: straight ceramic tube</i> .....	93
4.5.3.	<i>General results of pressure profile analysis</i> .....	95
4.5.4.	<i>Determination of the pressure inside the ion trap</i> .....	97
4.5.5.	<i>Signal loss with increasing sample pressure</i> .....	98

4.6.	<i>Optimization of operational conditions</i> .....	99
4.7.	<i>Analytical performance</i> .....	102
4.7.1.	<i>Analytical performance in residual gas mode</i> .....	103
4.7.2.	<i>Analytical performance in gas sampling mode</i> .....	107
4.8.	<i>SWIFT – a powerful tool needing further investigation</i> .....	119
4.9.	<i>Plasma-coupling</i> .....	121
4.10.	<i>Space charge induced ion coupling</i> .....	124
5.	<i>Summary and Conclusions</i> .....	126
6.	<i>Outlook</i> .....	131
7.	<i>Literature</i> .....	xii
8.	<i>Indexes</i> .....	vii

## *Notation and Terminology*

### **List of Acronyms**

ADC	Analog digital converter
AES	Auger electron spectroscopy
AFM	Atomic force microscopy
ALD	Atomic layer deposition
APCI	Atmospheric pressure chemical ionization
API	Atmospheric pressure ionization
APLI	Atmospheric pressure laser ionization
APPI	Atmospheric pressure photo ionization
B	Sector field mass spectrometer
CEM	Channel electron multiplier
CI	Chemical ionization
CMOS	Complementary metal-oxide semiconductors
CMP	Chemical mechanical planarization
CSA	Charge state amplifier
CT	Charge transfer
CVD	Chemical vapor deposition
DA-APPI	Dopant assisted atmospheric pressure photo ionization
DC	Direct current
EDS	Electron dispersive spectroscopy
EI	Electron ionization
ESI	Electrospray ionization
EUV	Extreme ultraviolet
FD	Field desorption
FFT	Fast Fourier transformation
FIA	Filter amplifier
FIB	Focuses ion beam
FT	Fourier transform
FT-ICR	Fourier transform ion cyclotron resonance mass spectrometer
FWHM	Full width at half maximum
GAMMA	Gas multimode mass analyzer
GC	Gas chromatography
GUI	Graphical user interface
IC	Integrated circuits
ID	Inner diameter
IE	Ionization energy
ipaMS	Institute for pure and applied mass spectrometry
LC	Liquid chromatography

LEC	Liquid-encapsuled Czochralski
LIT	Linear ion trap
LMCO	Lower mass cutoff
LOD	Limit of detection
M	molecule
MBE	Molecular beam epitaxy
MCP	Micro channel plate
MS	Mass spectrometry
MSn	Multiple MS experiments
OEM	Original equipment manufacturer
PA	Proton affinity
PT	Proton transfer
PTC	Physical and Theoretical chemistry
PVD	Physical vapor deposition
Q	Quadrupole mass filter
QIT	Quadrupole ion trap
REMPI	Resonance enhanced multiphoton ionization
RF	Radio frequency
RFA	RF amplifier
RGA	Residual gas analyzer
SEM	Secondary electron multiplier
SIMS	Secondary ion mass spectrometry
STM	Stimulus unit
SWIFT	Stored waveform inverse Fourier transform
TEM	Transmission electron microscopy
TOF	Time of flight mass spectrometer
UHV	Ultra-high vacuum
UV	Ultraviolet
XPS	X-ray photoelectron spectroscopy

## List of Physical quantities

$a$	Stability parameter in a quadrupolar field
$B$	Magnetic field strength [T]
$D$	Dehmelt potential [V]
$e$	Elementary charge: $1.602 \cdot 10^{-19}$ C
$E_{el}$	Electric energy [J]
$E_{kin}$	Kinetic energy [J]
$F_C$	Centripetal force [N]
$f_c$	Cyclotron frequency [Hz]
$f_{ion}$	Ion resonance frequency [Hz]
$F_L$	Lorentz force [N]
$k$	Field curvature (Orbitrap)
$m$	Mass [kg]
$m/z$	Mass to charge ratio [Da]
$m_H$	Mass of H-atom: $1.667 \cdot 10^{-27}$ kg
$q$	Charge, product of charge number $z$ and elementary charge $e$
$q$	Stability parameter in a quadrupolar field
$R$	Mass resolution
$r_0$	Radius [m]
$s$	Distance [m]
$S/N$	Signal to noise ratio
$t$	Time [s]
$T_p$	Duration of rectangular excitation pulse [s]
$U$	DC voltage [V]
$U_p$	Amplitude of rectangular excitation pulse [V]
$v$	Ion velocity [ $\text{m s}^{-1}$ ]
$V$	RF voltage [V]
$V_{pp}$	RF voltage peak – peak [V]
$V_{RF}$	RF voltage zero – peak [V]
$z$	Number of charges
$z_0$	Distance between trap center and endcap electrode [m]
$\beta$	Trapping parameter
$\tau$	Half period of the secular oscillation
$\Phi$	Potential [V]
$\omega$	Secular frequency [Hz]
$M$	Molecule
$M^+$	Molecule radical cation
$[M-H]^+$	Molecule with abstracted H-atom
$[M+H]^+$	Protonated molecular ion

## *1. Aim of this work*

In modern analytical instrumentation, mass spectrometry (MS) plays a predominant role. Mass spectrometers reveal insight into the structure and composition of matter in numerous fields of application, ranging from food inspection [1, 2] via anti-doping controls [2, 3] and analysis of pharmaceutical products [4] to air quality measurements [5], to name a few. A further important domain is process gas analysis [6, 7]. Monitoring of industrial processes with mass spectrometers improves the performance by increasing the quality and reproducibility of the optimum process conditions. Eventually, it is a matter of product quality, time and cost efficiency. Depending on the field of application, the requirements on the mass spectrometric setup significantly differ. In practice, the type of mass spectrometer, the sample and ionization method as well as the data processing need to be carefully aligned.

The present work is embedded in a project, which focuses on the development of a mass spectrometer for applications in process and residual gas analysis. The project goals pursue a number of demanding requirements: Instrument compactness, instrument robustness, fast and highly sensitive analysis of trace gas components, mass resolution well above nominal masses and affordability. The entire project can shortly be described by: “*From FT-QIT concept to the iTrap®*”. It is an interdisciplinary collaboration developing a mass spectrometer that is based on a three dimensional Quadrupole Ion Trap (QIT) using Fourier Transform (FT) technique. Members of this collaboration are the department for electrical engineering and the department for physical and theoretical chemistry of the University of Wuppertal, Plasma Applications Consulting GmbH and, as head of this collaboration, Zeiss SMT GmbH. Measurements carried out within the framework of this work are used to support the progress from a custom laboratory setup based on the *FT-QIT concept* to a salable device: the *iTrap®* [8].

Hence, this work focuses on the characterization of the laboratory setup to obtain input information for the development and operation of next generation instruments. Crucial operational parameters, the analytical performance, and comparisons with other mass spectrometric devices were carefully assessed. The potential of the FT-QIT as either a residual or a process gas analyzer within demanding gas matrices was proved with respect to a chemical understanding of the obtained mass spectra.

In short: The FT-QIT concept and the entire setup have to be put through their paces.

## *2. Introduction*

The first part of this chapter gives an introduction into mass spectrometry, in particular quadrupole ion traps and discusses the Fourier transform technique as a non-destructive ion detection method.

The second part presents typical processes in the semiconductor industry, an application field for which the developed instrument is designed in first instance. It will outline the essential requirements for a MS system to generate reliable and conclusive data under such demanding conditions.

The third part introduces the Zeiss-project GAMMA (short for “Gas multimode mass analyzer”) with respect to the envisioned device requirements, challenges, advantages, former approaches and the status quo.

### *2.1. Mass Spectrometry*

#### *2.1.1. General*

A mass spectrometric analysis allows the identification of masses or, to be more precise, the mass-to-charge ( $m/z$ ) ratios of compounds present in a sample [9–11]. That implies ionization, at least in part, of the neutral sample prior to analysis. In short, a mass spectrometric setup encompasses three basic elements [11]: i) an ion source to generate positive and/or negative gas phase charges of the sample, ii) an analyzer that separates the ions according to their  $m/z$  ratio and iii) a detector that generates an electronic signal proportional to the ion abundance of the particular  $m/z$  ratio [9, 10].

As mentioned before, the application fields for mass spectrometers are numerous, and so are the instrumental requirements. For example, air quality measurements and anti-doping control measurements obviously differ in the aggregate state of the sample - gaseous air and human blood, respectively. The latter with an elevated number of matrix components [12] obviously demands for a more proper sample preparation to generate the requisite gas phase ions: a preceding chromatography, the transfer of the analyte into the gas phase and a selective ionization - if possible [13, 14]. To meet the instrumental requirements for each analytical



problem, a large number of different methods with regard to ionization, analyzer and detection were developed since the introduction of mass spectrometry by J.J. Thomson in 1913 [15]. For the right choice of the system depending on the present analytical problem, it is indispensable to know the different types of mass spectrometers, their advantages and disadvantages as well as their characteristic performance.

In the following a brief introduction into ionization methods, analyzer systems and possibilities for ion detection is given.

### 2.1.2. Ionization methods

Electron ionization (EI) is the most common ionization method at high vacuum conditions [9, 10, 16, 17]. The collision of an energized electron with tens of electron volt kinetic energy leads to the generation of analyte radical cations if the transferred energy is greater than the ionization energy (IE). In that case an electron is removed from the analyte molecule (M) to form the radical cation ( $M^+$ ), as shown in (R.2.1) [9, 10, 16, 17].



Depending on the primary energy of the electrons even multiply charged ions are observed [18, 19].



Additional ionization pathways can lead to further ionic species of the analyte beside the molecular cation. Dissociative ionization and dissociative rearrangement lead to the formation of positively charged fragment ions, while electron capture and dissociative electron capture processes generate negatively charged analyte ions. Even the generation of ion pairs is possible. The ion yield essentially depends on the interaction between the analyte and the electrons [17, 18]. It is a function of the electron energy, as exemplarily shown for methane in Figure 1, with the ionization cross section plotted with respect to the electron energy [18]. Most compounds show qualitatively similar curves – they start with a steep increase at an electron energy corresponding to the IE, level off between 40 to 100 eV and slowly decrease again [18].

Due to the broad invariance in the ionization cross section at 70 eV this energy established to a standard and allowed to setup an instrument independent database for EI mass spectra.

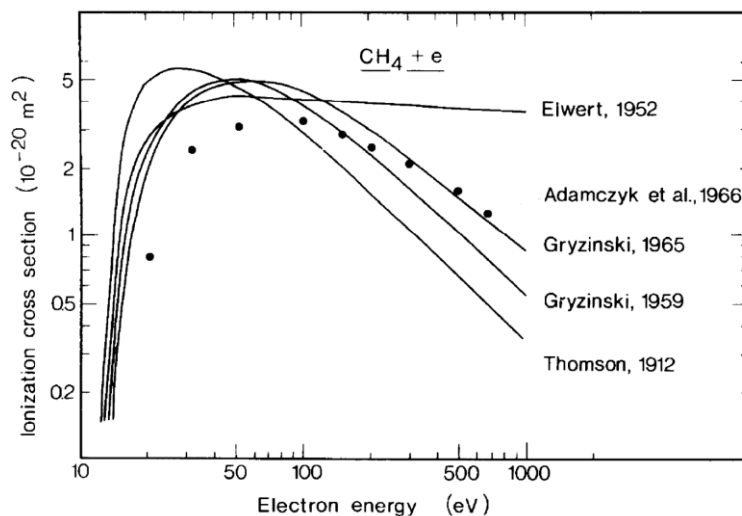
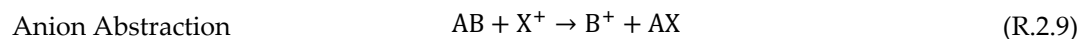
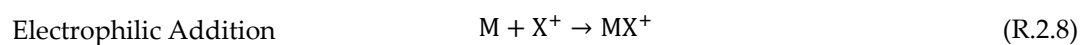
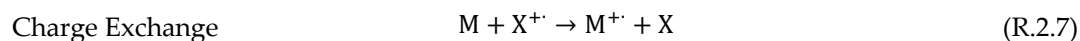
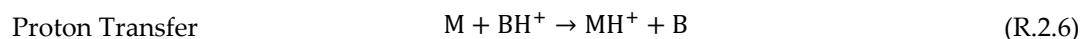


Figure 1: Ionization cross sections determined for the ionization of  $\text{CH}_4$  with electron impact [18].

An additional high vacuum ionization pathway is penning ionization [9, 20]. First, the interaction of an electron with a neutral rare gas atom (A) partially leads to electronically excited and radiative stable species, so called metastables ( $A^*$  or  $A^M$ ). Subsequent collisions with molecules of lower IE than the excess energy of  $A^*$  lead to ionization of these analytes according to reactions R.2.4 and R.2.5. In case of helium metastables the energy of the excited state is around 19 eV [21–23]. This is essentially higher than the ionization energies of most compounds and can lead to severe fragmentation such as in classical EI [24].

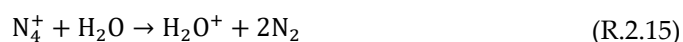


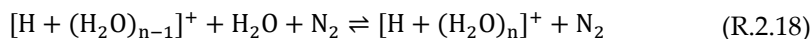
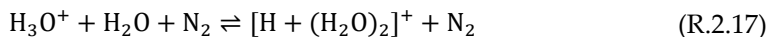
On search for a more gentle ionization method under high vacuum conditions chemical ionization (CI) was brought up, initially introduced by Munson and Field in 1966 [13, 25]. At first, reagent ions are generated by, e.g., electron impact ionization within an ion source operated at approximately 1 mbar. Subsequently sample ions are produced by ion-molecule reactions with the reagent ions. The reactions between positively charged reagent ions and sample molecules are generally grouped into four categories [13]:



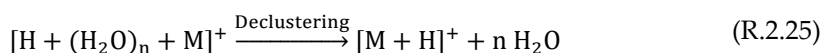
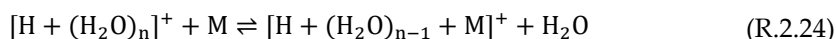
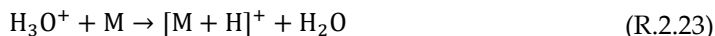
Methane is commonly used as reagent gas forming  $\text{CH}_5^+$  and  $\text{C}_2\text{H}_5^+$  by electron impact at 1 mbar [13]. Compared to EI ion generation CI leads to less excess energy transferred to the analyte molecules and thus less fragmentation.

The development of atmospheric pressure ionization (API) methods allowed combining the analytically important liquid chromatography with mass spectrometry [26]. In all API methods the ions need to be transferred from ambient pressure conditions to the high vacuum conditions in the mass analyzer. The application of so-called ion transfer stages, with ion optical elements such as, e.g. einzel lenses, multipoles and funnels allows ion guidance along a (stepwise) reduced pressure profile [26–28]. Furthermore, those ion optics are regularly used for selective removal or shielding of unwanted matrix and background ions [29]. Among the vast variety of API methods are, e.g., atmospheric pressure chemical ionization (APCI), atmospheric pressure laser ionization (APLI), atmospheric pressure photo ionization (APPI) and electrospray ionization (ESI). APCI, usually used for analytes with intermediate polarity, is typically initiated by a corona discharge [10, 17, 30]. Primary ions are generated in the plasma zone and subsequently produce reactant ions by charge transfer to matrix molecules. The following reactions for the generation of reactant ions are typically prevalent in API sources with abundant  $\text{H}_2\text{O}$  present [31, 32]:





In principle the analytes are subsequently ionized by charge transfer or by protonation in case of higher proton affinities (PA) than of the reactant ions (cf. R.2.19 – R.2.23) [34]. However, in most cases these processes comprise a more complex cluster chemistry in which the molecules of interest readily take part. That means it is more probable for analytes (here M) to enter the mass spectrometer in a clustered state than as the bare ion. The ion transfer stages in the MS ensure the declustering and eventually pass on the naked ion  $[\text{M}+\text{H}]^+$  to the analyzer (cf. R.2.24 – R.2.25) [34–36].



APLI [17, 37] as well as APPI [38, 39] are both photoionization methods and typically used for ionization of non-polar organic compounds such as polyaromatic hydrocarbons [17, 40]. Ionization energies of those compounds range between 5 and 10 eV. Krypton discharge lamps, as commonly used in APPI, emit light at 10 and 10.6 eV [38], enabling direct photo ionization (R.2.26).



A variation of APPI is called dopant-assisted APPI (DA-APPI) and essentially promotes the ionization process [41]. Owing to mixing ratios in the percent regime, the dopant (e.g., toluene,

anisole or acetone) is primarily photo ionized. Similar to the processes shown earlier for APCI, these primary charge carriers subsequently ionize the molecules of interest in diverse ion-molecule-reactions [35, 41]. APLI is based on multiphoton ionization and was developed as a highly sensitive ionization method in particular for polyaromatic hydrocarbons. The photon energies delivered by the laser system are typically lower than 6 eV, which necessitates at least two photons to ionize organic molecules [17]. The first photon elevates the analyte molecule into an excited state and the second photon, if applied within the lifetime of the excited state, promotes the electron into a continuum state and leaves the positively charged molecule. In case of a resonant excitation of the first state, this process is called resonance enhanced multiphoton ionization (REMPI) [9, 17, 42]. Particularly suitable for large, non-volatile organic molecules is electrospray ionization (ESI) [43, 44]. In most cases, this additional API method allows the formation of fragment-free and multiply charged ions of, e.g., proteins and nucleic acids [43–45].

This list can certainly be extended, however, it briefly emphasizes the most relevant ionization methods for this work.

### 2.1.3. *Miscellaneous mass analyzer systems*

All mass analyzers spatially separate ions with respect to their  $m/z$  ratios [9, 10, 46]. However, the physical background of each functional principle is clearly distinct. The most established systems are time of flight (TOF) instruments, magnet sector field devices (B), linear quadrupole instruments (Q), linear quadrupole ion traps (LIT) as well as three-dimensional quadrupole ion traps (QIT), FT ion cyclotron resonance mass spectrometers (FT-ICR) and the Orbitrap [9, 47].

#### **Time of flight instruments**

In time of flight mass spectrometers a temporal dispersion of a pulsed ion beam is observed. Ions experience an acceleration voltage for a collision- and field-free flight inside a drift tube [9, 48, 49]. Their kinetic energy ( $E_{kin}$ ) directly corresponds to the electrical acceleration ( $E_{el}$ ) according to:

$$E_{el} = e z U = \frac{1}{2} m \bar{v}^2 = E_{kin} \quad (2.1)$$

Herein  $e$  is the elementary charge,  $z$  the number of charges,  $U$  the applied voltage,  $m$  the ion mass and  $\bar{v}$  the ion velocity. Conversion of equation (2.1) shows that the ion velocity is inversely proportional to the square root of the ion mass:

$$\bar{v} = \sqrt{\frac{2ezU}{m}} \quad (2.2)$$

With a defined flight distance  $s$  and the velocity as a distance in a certain time  $t$ , equation (2.2) is reformulated as:

$$t = \frac{s}{\sqrt{2eU}} \sqrt{\frac{m}{z}} \quad (2.3)$$

Thus, the flight time is directly proportional to the square root of the ion mass divided by the number of charges. Mass resolution in TOF instruments is enhanced by an increasing time interval  $\Delta t$  between ions of different  $m/z$  ratios. As  $\Delta t$  is proportional to  $s \cdot ((m_1/z_1)^{1/2} - (m_2/z_2)^{1/2})$  an increase in flight distance results in higher mass resolution [48]. The application of reflectrons, as initially described by Mamyrin et. al. [48, 50], allows a prolongation of the flight distance by electrical reflection of ions within the drift tube, without suffering a dramatic increase of the entire system. Thus, the maximum reachable mass resolution is significantly enhanced. Since TOF instruments are typically operated with spectral save rates of some kHz, a single mass spectrum is obtained in less than a ms [49].

Table 1 summarizes typical figures of merit for TOF mass analyzers [9, 47].

Table 1: Typical figures of merit for TOF mass analyzer [9, 47].

<b>Mass resolution</b>	1,000 – 40,000
<b>Mass range</b>	> 100,000 Da
<b>Mass accuracy</b>	5 – 50 ppm
<b>Spectral save rate</b>	10,000 spectra/s

### Magnet sector field instruments

In magnet sector field instruments charged particles in an accelerated ion beam are  $m/z$ -separated by a perpendicular magnetic field [9, 10]. With the magnetic field vector  $\vec{B}$  orthogonal to the velocity vector  $\vec{v}$  of the moving particle, Lorentz force  $F_L$  is given as:

$$F_L = q\vec{v}\vec{B} = ez\vec{v}\vec{B} \quad (2.4)$$

In a homogenous magnetic field the charged particle moves in a circular orbit with radius  $r$ . Thereby Lorentz force  $F_L$  and centripetal force  $F_C$  are in equilibrium:

$$F_L = ez\vec{v}\vec{B} = \frac{m\vec{v}^2}{r} = F_C \quad (2.5)$$

Solving equation (2.5) to  $r$  results in:

$$r = \frac{m\vec{v}}{ez\vec{B}} \quad (2.6)$$

The radius of the spherical orbit is directly proportional to the momentum of the charged particle. Substituting the velocity  $\vec{v}$  according to equation (2.5) shows that the radius  $r$  is proportional to the square root of the  $m/z$  ratio:

$$r = \frac{m}{ez\vec{B}} \sqrt{\frac{2ezU}{m}} = \frac{1}{\vec{B}} \sqrt{\frac{2mU}{ez}} \quad (2.7)$$

Table 2 summarizes typical figures of merit for double focusing sector mass analyzers [47, 51].

Table 2: Typical figures of merit for double focusing sector mass analyzer [47, 51].

<b>Mass resolution</b>	100,000
<b>Mass range</b>	10,000 Da
<b>Mass accuracy</b>	< 1 ppm
<b>Temporal resolution</b>	0.1 s per decade

### 2.1.4. Quadrupole based mass analyzer

Quadrupole instruments, including linear quadrupole mass analyzers, linear quadrupole ion traps as well as three-dimensional quadrupole ion traps form a large group of mass analyzer systems [52].

#### 2.1.4.1 Linear quadrupole instruments

Linear quadrupole devices are made of four either hyperboloid (ideally) or cylindrical bar electrodes. Opposing electrodes form pairs of equal potential, which is composed of a direct and an alternating current (cf. Figure 2) [9, 10].

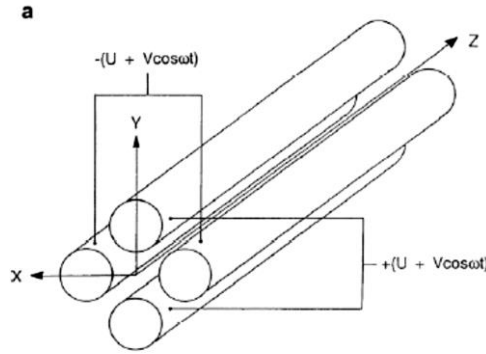


Figure 2: Schematic of a linear quadrupole analyzer [9].

Ions enter the linear quadrupole in  $z$ -direction and are immediately exposed to a periodically attracting and repulsive voltage, which forces them to move back and forth in the  $x,y$ -plane [9, 53, 54]. With the applied DC voltage  $U$  and the radio frequency (RF) voltage  $V$  of frequency  $\omega$ , the time dependent total potential  $\Phi_0$  is given by:

$$\phi_0 = U + V\cos(\omega t) \quad (2.8)$$

Equations (2.9) and (2.10) hold for the motion in  $x$ - and  $y$ -direction:

$$\frac{d^2x}{dr^2} + \frac{e}{m_i r_0^2} (U + V\cos(\omega t))x = 0 \quad (2.9)$$

$$\frac{d^2y}{dr^2} + \frac{e}{m_i r_0^2} (U + V\cos(\omega t))y = 0 \quad (2.10)$$



An ion passes the quadrupole analyzer in  $z$ -direction without contacting the electrode rods if its motion around the  $z$ -axis is stable in the  $x, y$ -plane. The stability conditions are derived from Mathieu's equations [9, 52, 55]. In dimensionless form equations (2.9) and (2.10) yield:

$$\frac{d^2x}{d\tau^2} + (a_x + 2q_x \cos 2\tau)x = 0 \quad (2.11)$$

$$\frac{d^2y}{d\tau^2} + (a_y + 2q_y \cos 2\tau)y = 0 \quad (2.12)$$

A comparison of equations (2.9)-(2.10) and equations (2.11)-(2.12) gives the parameters  $a$  and  $q$ :

$$a_x = -a_y = \frac{4eU}{m_i r_0^2 \omega^2} \quad (2.13)$$

$$q_x = -q_y = \frac{2eV}{m_i r_0^2 \omega^2} \quad (2.14)$$

$$\tau = \frac{\omega t}{2} \quad (2.15)$$

Ions that oscillate within a distance of  $2r_0$  between the electrodes move on stable trajectories. Stability or instability of ion movement within the quadrupole analyzer depends on  $U$ ,  $V$  and  $\omega$ . Plotting  $a$  versus  $q$  leads to a stability diagram as shown in Figure 3 (left) presenting different areas with i) stable  $x$ - and  $y$ -trajectories, ii) either stable  $x$ - or stable  $y$ -trajectories or iii) no stable ion trajectories [53]. For the operation of linear quadrupole devices only a small section of the stability diagram is relevant as shown in Figure 3 (right) [56].

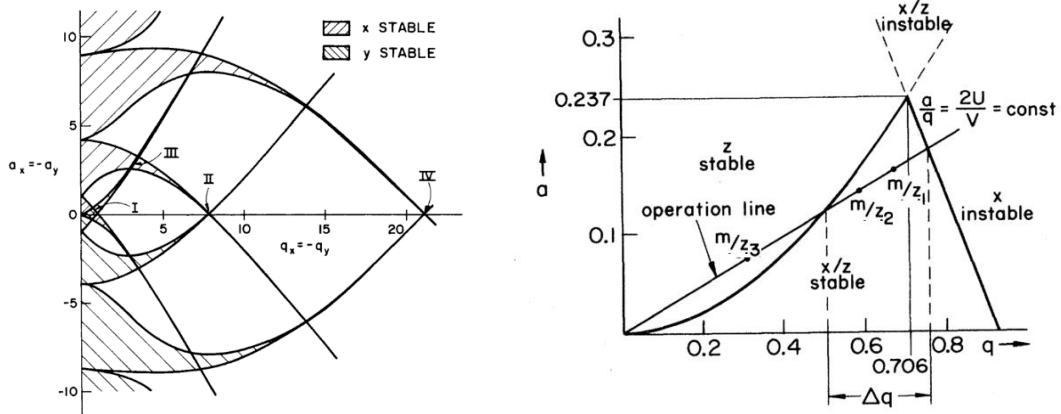


Figure 3: Left: Stability diagram [53]; right: Enlargement of stability diagram (reproduced from [56]).

The additional straight line (operation line) in the diagram, with a slope defined by the  $a/q$  ratio, readily depicts the  $m/z$  range that is hold by the quadrupole field. Therefore, it is looked at the intersecting part with the stability diagram [56, 57]. As can easily be seen, a slope of  $a/q = 0.237/0.706 = 0.336$ , corresponding to twice the DC voltage relative to the RF amplitude ( $2U/V$ ), reduces the intersecting part to a point of an infinitesimally small stable  $m/z$  range. Slowly decreasing this ratio leads to an increasing field-captured  $m/z$  range, starting with the smallest value. This principle applies to all scanning linear quadrupole mass filters, where the continuous  $a/q$  ratio decrease allows to consecutively transmit ions with increasing  $m/z$  value [10, 47, 54]. In theory, the ramped incremental step size of  $a/q$  determines the mass resolution of these devices – the smaller the increment the higher the resolution. In praxis, however, the mechanical accuracy of the rod electrodes, retainer, etc. are the factors that in most available devices limit the resolution to nominal mass [54]. Nowadays linear quadrupoles are standard mass filters for mostly residual gas analyzer (RGA) or routine GC-MS applications, since they are reasonably priced, rugged and compact [14]. In more sophisticated MS systems they are integrated as simple ion transfer and  $m/z$  range preselection devices [53, 58, 59].

Typical figures of merit for the application of linear quadrupole mass analyzers are summarized in Table 3 [47, 60].

Table 3: Typical figures of merit for linear quadrupole mass analyzers [47, 60].

<b>Mass resolution</b>	100 – 1,000
<b>Mass range</b>	4,000 Da
<b>Mass accuracy</b>	100 ppm
<b>Temporal resolution</b>	100 – 1,000 ms

### 2.1.4.2 Linear quadrupole ion traps

Linear quadrupoles are also operated as ion storage devices. In contrast to the above described transmitting mode, the  $a/q$  ratio is set to zero, which captures a broad  $m/z$  range in the  $x,y$ -plane between the rods (cf. Figure 3 left) [9, 10, 61]. In  $z$ -direction two electrodes at each end of the rods form an additional potential barrier to create a trapping volume. In praxis, a continuous ion current first enters the quadrupole through the lowered entrance electrode and is reflected by the raised exit electrode, while the RF field of the rods traps in the  $x,y$ -plane. After accumulation of a defined amount of charge, the entrance electrode is pulled to high and closes the trapping volume [61, 62]. Additional collisional cooling with a buffer gas (e.g., argon or nitrogen) at pressures of around  $10^{-3}$  to  $10^{-2}$  mbar focuses the ions on the LIT axis. Hence, the probability of storing faster ions correlates with the background pressure. As  $m/z$  separating devices, LITs enable either radial or axial ion ejection. The latter mode uses the coupled axial and radial ion movement, owing to stray fields at the LIT exit. If the radial secular frequency of a particular ion species coincides with an auxiliary AC voltage, these ions are excited well above the axial trapping potential. Consequently, this particular  $m/z$  range is axially ejected from the LIT. The radial ejection of ions is accomplished with a slit in one of the electrode rods and an applied bi-phase alternating voltage along the  $x$ -rods [61].

Owing to their versatile operation, LITs are often integrated in more complex mass analyzer systems i) as trapping devices to control the amount of charge, ii) for ion cooling or iii) for ion manipulation, such as fragmentation or specific ion-molecule reactions (e.g., H/D exchange with  $D_2O$ ) to reveal important structural information [61–63].

Table 4 summarizes typical figures of merit for linear quadrupole ion traps [47, 62].

Table 4: Typical figures of merit for linear quadrupole ion traps [47, 62].

<b>Mass resolution</b>	1,000 – 10,000
<b>Mass range</b>	4,000 Da
<b>Mass accuracy</b>	50 – 100 ppm
<b>Temporal resolution</b>	1 – 2 s

### 2.1.4.3 Three-dimensional quadrupole ion traps

Paul and Steinwedel introduced the three-dimensional RF driven quadrupole ion trap as a mass spectrometric analyzer in 1953 [64]. In their patent from 1960, detailed operational features are described [65]. QITs consist of a ring electrode and two end cap electrodes with hyperboloid surfaces. A RF voltage with a frequency of approx. 1 MHz is applied to the ring electrode. Depending on their  $m/z$  ratio ions move on different stable trajectories in the trapping volume [52, 66, 67]. Hence separation or selected detection of charged particles allows the application of QITs for mass spectrometric studies, isolation of isotopes, for partial pressure measurements or as leak detectors, to name a few [56, 65].

A comprehensive understanding of the ion motion within the electrodynamic field of a three-dimensional quadrupole trap is essential for the technical realization of QITs as mass spectrometers [52, 68, 69]. Similar to linear quadrupole instruments, Mathieu's equations form the basis for the mathematical description of these ion trajectories [55]. Definitions of the  $r$ - and  $z$ -coordinates, electrode arrangement and the resulting electric field are depicted in Figure 4.

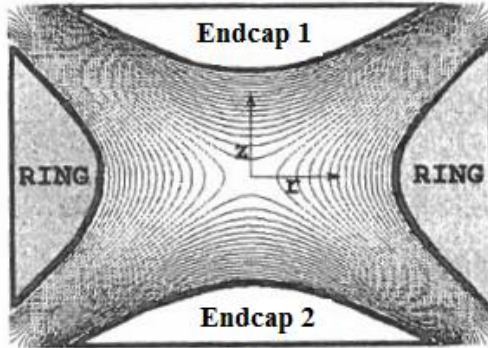


Figure 4: Potential curve inside the quadrupole ion trap (reproduced from [70]).

In the case of grounded endcap electrodes, the potential inside the trap depends on the DC voltage  $U$  and the RF voltage  $V$  with  $\Omega = 2\pi f$  and  $f$  as the fundamental RF frequency, resulting in [52, 66]:

$$\Phi_0 = U + V \cos \Omega t \quad (2.16)$$

The transformation of Cartesian coordinates into cylindrical coordinates gives:

$$\Phi_{x,y,z} = \frac{\Phi_0}{r_0^2} (r^2 \cos^2 \theta + r^2 \sin^2 \theta - 2z^2) \quad (2.17)$$

With  $\cos^2 + \sin^2 = 1$ , equation (2.17) is simplified to:

$$\Phi_{r,z} = \frac{\Phi_0}{r_0^2} (r^2 - 2z^2) \quad (2.18)$$

The equations of ion motion are written as:

$$\frac{d^2 z}{dt^2} - \frac{4e}{m_i r_0^2 + 2z_0^2} (U - V \cos \Omega t) z = 0 \quad (2.19)$$

$$\frac{d^2 r}{dt^2} + \frac{2e}{m_i r_0^2 + 2z_0^2} (U - V \cos \Omega t) z = 0 \quad (2.20)$$

The similarity to Mathieu's equations enables the solution of this differential equations, giving  $a$ - and  $q$ -parameters in  $z$ - and  $r$ -direction:

$$a_z = -2a_r = -\frac{16eU}{m_i r_0^2 + 2z_0^2 \Omega^2} \quad (2.21)$$

$$q_z = -2q_r = -\frac{8eV}{m_i r_0^2 + 2z_0^2 \Omega^2} \quad (2.22)$$

Operation in ion storage mode requires stable trajectories in  $z$ - as well as in  $r$ -direction, otherwise ions are lost due to collision with the inner surfaces or due to ejection from the QIT volume. Similar to linear quadrupole mass filters, the stability of ions in the applied trapping field is illustrated in  $a_z$  vs.  $q_z$  diagrams. Here the stability of ion trajectories is represented by the parameters  $\beta_r$  and  $\beta_z$ , which themselves are complex functions of the  $a$ - and  $q$ -values. Figure 5 shows the first stability region, which is the most important section for operating a QIT [52, 68].

The trapped  $m/z$  range is characterized by the intersection between the diagram and a straight line defined by the slope  $U/V$ . This approach is similar to the theory of linear quadrupoles as discussed previously. In praxis, however, most QITs operate in RF-only mode that means  $a_z$  equals zero and the intersecting part is simply represented by the  $q_z$ -axis from  $q_z = 0$  up to  $q_z = 0.908$ . The latter defines the smallest amenable  $m/z$  ratio and is called the lower mass cutoff (LMCO) [52]. Theoretically, there is no upper  $m/z$  limit for this mode. In praxis, however, ions with  $m/z$  values of 20-30 times the LMCO are not efficiently trapped.

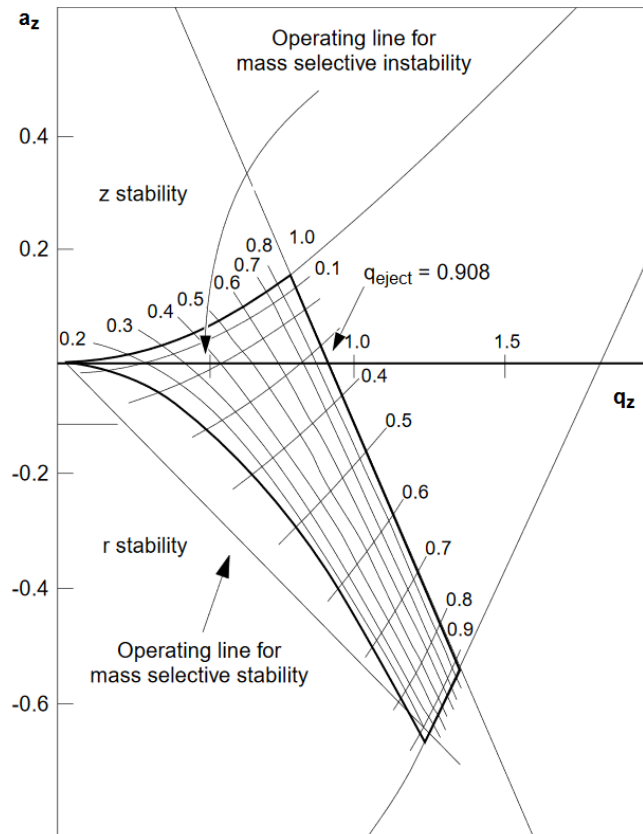


Figure 5: Zoom into the stability diagram [68].

In the early days of the QIT development ions were initially generated inside the trap, so called in-trap electron ionization. Nowadays, ions are in most applications generated externally, which necessitates electrically driven ion guiding into the trapping volume. Consequently, the charged species obtain kinetic energies well above thermal distribution, which means that without any decelerating force they simply fly through the QIT and are not trapped. To increase the trapping efficiency the background pressure is usually maintained at roughly  $10^{-5}$  mbar of helium. These conditions enhance the collisional cooling effect and thus significantly increase the trapping efficiency [52, 66, 67].

The ion motion inside a 3D-trap is roughly comparable with a ball in the middle of a rotating saddle [71]. Depending on the inertial mass and the rotation frequency the ball moves on a stable trajectory inside the saddle. In a more precise visualization, these trajectories are described as Lissajous-trajectories [72] (cf. Figure 6). This particular motion results from a superposition of the ion secular vibrations in  $r$ - and in  $z$ -direction.

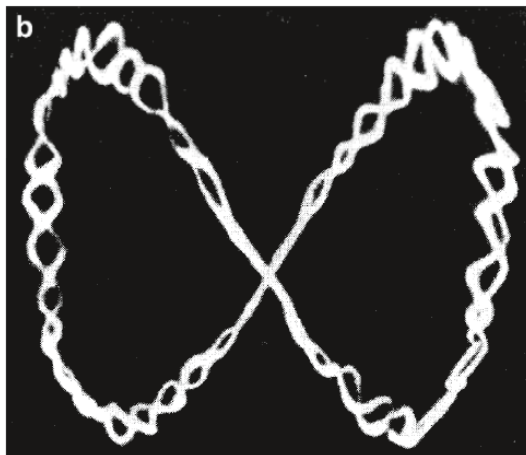


Figure 6: Photograph of the ion trajectories of charged particles in a quadrupole ion trap [72].

Once a certain ion population is stored, QITs offer three different scanning options for selective  $m/z$  ejection and subsequent external detection: i) the mass-selective stability mode, ii) the mass-selective instability mode, and iii) resonant ion ejection [9, 52, 68]. In the mass-selective stability mode, the QIT first accumulates a very narrow  $m/z$  range, in the ideal case a single  $m/z$  value. Subsequently, a negative voltage pulse on one of the endcap electrodes ejects this specific ion species for external detection. To record an entire mass spectrum this cycle has to be repeated for every single  $m/z$  value, which makes the mass-selective stability mode a very slow procedure. Consequently, its application nowadays is rather limited. In the mass-selective instability mode a broader  $m/z$  range is first accumulated. For subsequent ejection, the endcap electrodes are kept at ground and the applied RF voltage is incrementally raised. This causes the consecutively ejection in the order of increasing  $m/z$  ratios, as shown by the stability diagram in Figure 5. The resonant ion ejection mode also accumulates a broad  $m/z$  range in the first instance. Ideally, ion motion in radial and axial direction are independent. Thus vibrations are described by radial and axial secular frequencies, each a function of the trapping parameters  $a$  and  $q$ . An additionally applied RF voltage that is equal to the axial resonance frequency allows the resonant ejection of ions with a specific  $m/z$  ratio [9, 52, 66].

QITs with nominal mass resolution are well priced and typically equipped with EI or CI [9, 52]. More expensive systems reach up to five-fold of nominal mass resolution, are designed for a broader mass range and are typically combined with API sources [9]. An outstanding feature of ion traps is the capability of performing  $MS^n$  (sequential mass analysis) experiments

due to sequential ion isolation and CID (collision induced dissociation) processes. Thus, MS<sup>n</sup> analysis provides structural information on parent ions as well as on fragment ions [47, 66].

Table 5 summarizes typical figures of merit for three-dimensional quadrupole ion traps [47, 61].

Table 5: Typical figures of merit for three-dimensional quadrupole ion traps [47, 61].

<b>Mass resolution</b>	1,000 – 10,000
<b>Mass range</b>	4,000 Da
<b>Mass accuracy</b>	50 – 100 ppm
<b>Temporal resolution</b>	100 ms

#### 2.1.4.4. Detectors

Once the analyzer separated a certain ion population according to more or less distinct  $m/z$  values, the charge is converted with a detector into an electronic signal in relation to time or space. The easiest kind of detector is the Faraday cup. Here, the ions simply collide with a metal cup, lose their charge and consequently cause a measurable electric current that is proportional to the number of collected ions. This type requires the balance between sensitivity and time resolution – an increasing resistance for the cup to discharge, increases the sensitivity, however, at the cost of time resolution to detect separated ion clouds. More frequently used are secondary electron multipliers (SEM), which are fast and sensitive. Here, energetic particles collide with the surface of a SEM and liberate secondary electrons, depending on the initial particle velocity and the work function of the surface. A successive series of electrodes with a significant potential gradient further accelerates the electrons and causes an avalanche process. Eventually an electric current is detectable with a sensitive preamplifier. Depending on the applied voltages, the amplification of the current is in the range of  $10^6$  to  $10^9$  [57, 73].

The avalanche process of an electron current is also used in Channeltrons and micro channel plates (MCP), as illustrated in Figure 7 and 8. Channeltrons or channel electron multipliers (CEM) are more compact than SEMs. The resistance of the semiconductive



material of the CEM has to be high enough to resist a voltage of approx. 2 kV that decreases continuously along the tube. The emission material is a silicon dioxide layer over a lead oxide layer on the lead doped glass tube. As shown in Figure 7, CEMs are produced either in a straight or in a bended version. The latter amplify up-to  $10^8$ .

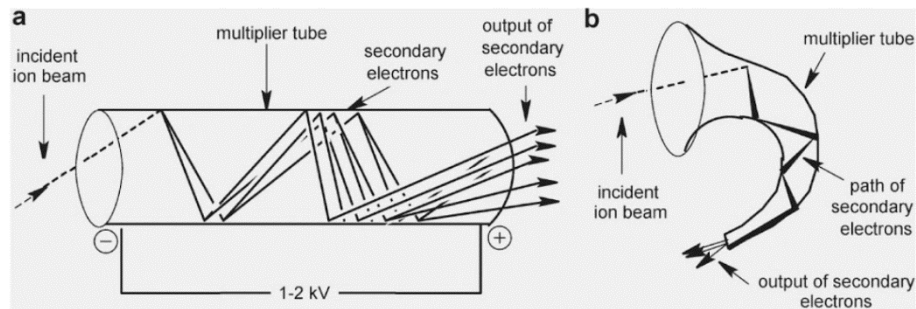


Figure 7: CEM in either a) straight or b) bended form [57].

The inner diameter of a linear channeltron can be reduced to some micrometers. An array of millions of micro channels compensates for the quite small cross section. Those micro channels are slanted for some degrees relative to the plate surface to prevent ions from entering the channel coaxially. The amplification of a single MCP is in the range of  $10^3$ - $10^4$ . Often two MCPs are combined allowing an amplification factor of  $10^6$ - $10^7$  (Chevron-plate, see Figure 8 center) or with three MCPs in a z-stack an amplification of  $10^8$  (see Figure 8 right) [57, 73, 74].

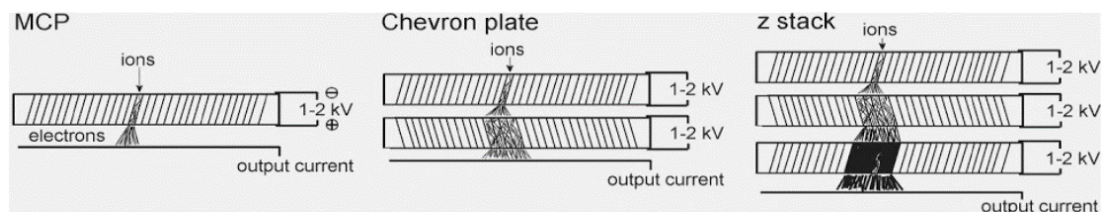


Figure 8: Different varieties of MCPs. Left: Single MCP. Center: Chevron plate. Right: z-stack configuration [57].

### 2.1.5. Fourier Transform based Mass Spectrometers

The following section addresses analyzers that encompass the mass separation volume and the ion detection unit in the same device. These systems use the induced image current of mass separated and periodically cycling ion clouds and convert them with Fourier transformation into a mass spectrum. This principle of operation is classified as a “*non-destructive*” ion detection method, in contrast to the systems described above [73].

#### 2.1.5.1. Fourier Transformation

Fourier transformation (FT) is a mathematical operation traced back to the work of Jean-Baptiste Joseph Fourier. It allows to calculate a continuous spectrum from an aperiodic signal, e.g., the frequency spectrum from the superimposed transient time signal. Thus, the domain of the initial function is time whereas the domain of the Fourier transformed function is frequency. The function in the frequency domain reflects all frequencies with their amplitudes contained in the initial function. It is noted that the resolution of the frequency spectrum significantly scales with the observation time of the initial signal. In other words: the longer the transient signal, the better the resolution in the frequency spectrum [9].

#### 2.1.5.2. Fourier transform Ion Cyclotron Resonance

The operation principle of FT-ICR instruments is based on ion cyclotron resonance, known since the early 1930’s. Charged particles circulate in a transversal electrical trapping field ( $z$ -direction) and orthogonally to an applied magnetic field ( $x,y$ -plane). The latter trajectory with radius  $r$  is mathematically derived from equating the Lorentz and the centrifugal force, both acting on a charged particle with mass  $m$ , charge  $q=z \cdot e$  and velocity  $\vec{v}$  [9, 75]:

$$r = \frac{m\vec{v}}{ze\vec{B}} \quad (2.23)$$

With  $\vec{v} = r\omega$  the cyclotron angular frequency  $\omega_c$  is written as:

$$\omega_c = \frac{ze\vec{B}}{m} \quad (2.24)$$

Introducing the cyclotron frequency  $f_c = \omega_c/2\pi$  gives:

$$f_c = \frac{z}{m} \cdot \frac{e\vec{B}}{2\pi} \quad (2.25)$$

This so-called cyclotron equation shows that the ion cyclotron frequency is independent of the initial ion velocity but proportional to the charge and the magnetic field and inversely proportional to the ion mass. Initially, ions with identical  $m/z$  values thus cycle in the  $x,y$ -plane with the same  $f_c$ , however, they are randomly distributed with respect to their kinetic energy and spatial position according to the relationship between  $v$  and  $r$  in equation (2.23). In order to obtain a mass dependent signal, a coherent, macroscopic cyclotron motion of identical species is induced with an electrical pulse orthogonal to the magnetic field direction. In the early days ICR devices were operated in energy scanning mode. Here the ions move with their cyclotron frequency in increasing helical trajectories upon resonant RF acceleration perpendicular to the magnetic field. Owing to the constant kinetic energy uptake ions will at some point meet the condition  $r_{ion} = r_{cell}$ , and discharge at the wall, which can be measured with a connected electrometer. Disadvantages of this method are: i) limitation of the mass accuracy and mass resolution to  $1/N_c$  with  $N_c$  as number of half-cycles, ii) unamplified charge detection and iii) removal of ions from the cell, which renders MS/MS experiments impossible. The ICR performance was enormously improved by changing from destructive to non-destructive ion detection with measuring image currents. In case of positively charged ion clouds passing by the detector electrodes, the electrons inside the electrode are attracted. This results in a small image current for each ion cloud each time the ion cloud passes by. These image currents are amplified and converted into voltage signals. Hence, a transient signal with superimposed ion frequencies is obtained. As explained above, this signal is transformed into a frequency spectrum by Fourier transformation and subsequently converted into a  $m/z$  spectrum according to equation (2.25) [9, 75].

FT-ICR instruments are often used in combination with LITs or other trapping devices. Those trapping devices prepare the ion population to deliver a suitable number of ions to the FT-ICR analyzer. Strong superconducting magnets are required for FT-ICR mass spectrometers, since the mass resolution, scan rate and mass range scale with the applied magnetic field strength. Typical field strengths are 7 T or 9.4 T, but even 12 T, 15 T and 21 T [76] instruments are used more frequently nowadays. These magnets need helium cooling and

for descent mean free pathways elaborate vacuum conditions of at least  $10^{-9}$  mbar are required [76] – constraints that make FT-ICR instruments quite large and expensive. However, they obtain unprecedented mass resolution of  $R = 1 \cdot 10^5 - 2 \cdot 10^6$  [47, 76].

Table 6 sums up the figures of merit typically reachable with FT-ICR instruments [47, 77].

Table 6: Typical figures of merit for FT-ICR instruments [47, 77].

<b>Mass resolution</b>	10,000 – 1,000,000
<b>Mass range</b>	> 10,000 Da
<b>Mass accuracy</b>	1 – 5 ppm
<b>Scan rate</b>	1 Hz

### 2.1.5.3. Orbitrap

The Orbitrap is another mass analyzer with FT signal processing. The principle of ion trapping is based on the Kingdon trap as introduced in the early 1920's [78, 79]. This first design was made of a cylindrical and a coaxially centered thin wire electrode. Two plane electrodes on each side of the cylinder closed the trapping volume, similar to the trapping in z-direction of LIT and ICR-cells. The balance between the electrostatic field and centrifugal force determines the concentric rotation in the  $x,y$ -plane around the wire. This configuration, however, was not practical for  $m/z$  separation. In 1981 Knight slightly changed the field geometry with a bisected and spindle-like shaped outer electrode [80]. Although this modification added an additional,  $m/z$  dependent harmonic motion in z-direction, Knight was still not able to practically detect distinct mass-to-charge ratios. It was not until 1999 when Makarov leveraged this analyzer type owing to three substantial modifications [81]: i) smoother field geometry with precisely defined quadrupole and logarithmic field portions, ii) image current detection on the bisected outer electrode and iii) injection of spatially and kinetically well confined ion packages with an upstream, second trapping device, the so called *c-trap* [81]. The c-trap is a curved quadrupole that allows trapping and collisional cooling of a well-defined number of ions [82, 83]. A short high voltage pulse injects the ions into the orbitrap; at the same time the potential of the central electrode is lowered and the ions are trapped and directed onto their spherical orbits.

Figure 9 shows a cutaway of the commercial Orbitrap from Thermo Fisher Scientific [83].

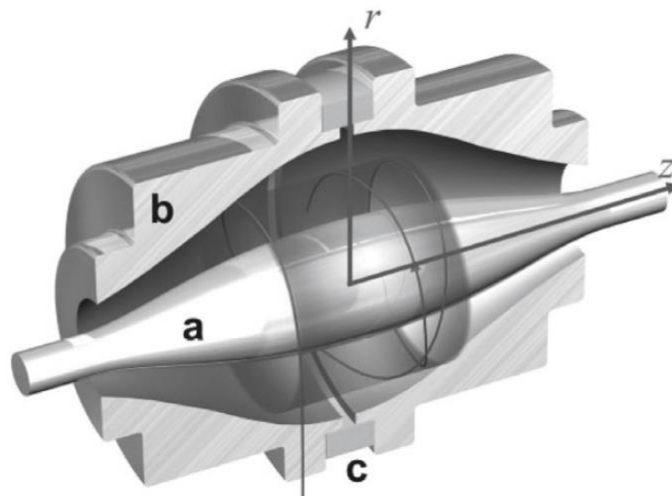


Figure 9: Cutaway of the commercial Orbitrap from Thermo Fisher Scientific [83].

The quadrologarithmic field is given by:

$$U(r, z) = \frac{k}{2} \left( z^2 - \frac{r^2}{2} \right) + \frac{k}{2} (R_m)^2 \ln \left[ \frac{r}{R_m} \right] + C \quad (2.26)$$

Wherein  $r$  and  $z$  are cylindrical coordinates,  $k$  is field curvature,  $R_m$  is the characteristic radius and  $C$  is a constant. The field described by equation (2.26) forces the ions in the Orbitrap on helical trajectories. Stable trajectories result from a combination of rotation around the central axis and axial vibrations [79, 81]. The axial vibrational frequency  $\omega_z$  is given by:

$$\omega_z = \sqrt{k \left( \frac{ze}{m_i} \right)} \quad (2.27)$$

It is only a function of the ion charge, the ion mass and the field curvature, thus independent of the tangential velocity and the spatial ion distribution. Axial frequencies are measured as image currents on both halves of the outer electrode and subsequently analyzed with fast Fourier transformation. The Orbitrap demonstrated outstanding performance in terms of mass resolution and accuracy, comparable to 12 T and 15 T FT-ICR instruments [84]. The axial frequency  $\omega_z$  in the Orbitrap is proportional to  $(z/m)^{1/2}$  compared to the cyclotron frequency  $\omega_c$  in FT-ICR devices, which is proportional to  $z/m$ . Hence, FT-ICR enables greater mass resolution for ions with low  $m/z$  whereas the Orbitrap shows better performance at higher  $m/z$ .

ratios [84]. Equation (2.27) also shows that lighter ions pass more oscillations for a given transient signal than heavier species. This means that the resolving power is mass dependent, since the resolution in the FT transformed frequency spectrum is proportional to the number of recorded oscillations. As noted above, longer transient signals significantly enhance the resolving power, however, at the cost of the analyzer speed and the requirements for the vacuum system. For standard operation, at least  $10^{-9}$  mbar are necessary to prevent collisional dephasing [84]. With that, resolving powers of 240,000 (at  $m/z$  400) for about 1s long transients were obtained [85].

Table 7 sums up the figures of merit that are typically reachable with Orbitrap mass analyzers [10, 86].

Table 7: Typical figures of merit for Orbitrap mass analyzers [10, 86].

<b>Mass resolution</b>	100,000 – 250,000
<b>Mass range</b>	> 10,000 Da
<b>Mass accuracy</b>	< 5 ppm
<b>Scan rate</b>	1 – 10 Hz

## 2.2. Semiconductors

The omnipresence of semiconducting materials is shaping our daily lives, be it in smartphones, televisions or computers, just to name a few [87]. All these devices are equipped with sophisticated electronics, usually comprised of several semiconducting elements in so-called integrated circuits (IC). In 1965 Gordon Moore, co-founder of Intel, predicted that the number of components on chips would double every 12 month, later revised to two years [88, 89]. Moore’s Law is an inspiration for engineers to push the technology of semiconducting materials to astonishingly ongoing performance. Figure 10 relates the number of transistors on new developed processor chips to the launched year – in accordance to Moore’s Law [90]. This rapidly increasing progress in electronic devices demands for elaborate manufacturing processes, which will be issued in a later chapter.

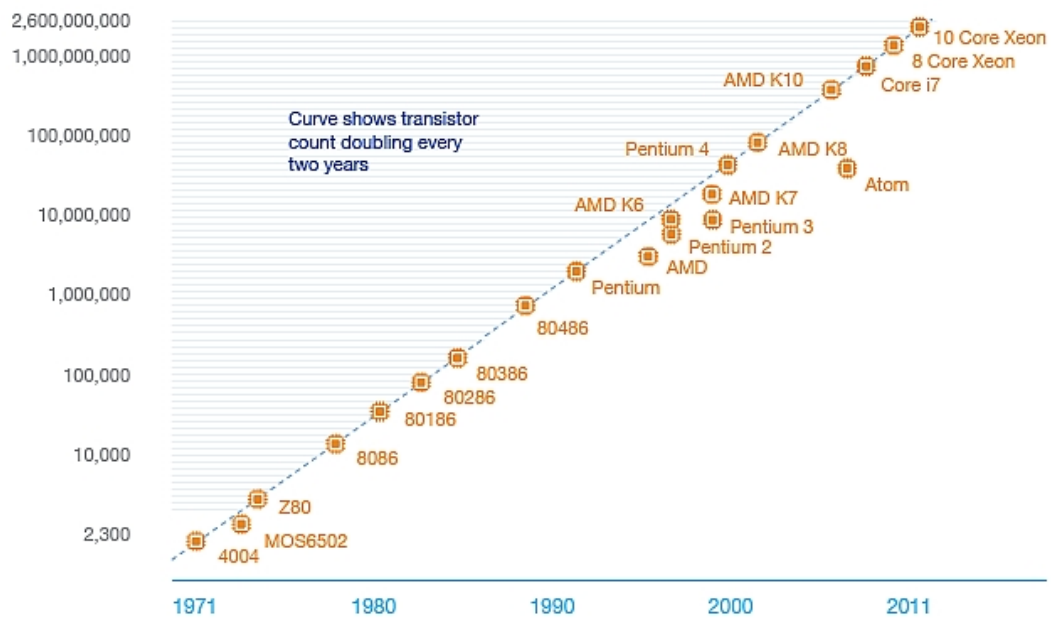


Figure 10: Number of transistors on newly developed processor chips in dependence of the launched year - in accordance with Moore's Law [90].

### 2.2.1. General: Basics and Applications

The energy gap between the valence and the conduction band is the characteristic quantity of semiconductors. It essentially determines the specific properties of different materials, in particular their conductivity. In stark contrast to the overlying bands in metals, semiconductors require partially unoccupied bands to pass an electrical current [91, 92]. As a result, the temperature dependency of the conductivity between metals and semiconductors runs in the exact opposite. At 0 K the valence band of a semiconductor is fully occupied and the conduction band is empty. An increase in temperature shifts the energy distribution of the electrons in the valence band to higher energies, which causes some electrons to overcome the gap to the conduction band [91]. It follows that the number of available electrons in the conduction band as well as the number of electron holes in the valence band increase – the resistance of the material decreases. In principal, the conduction of electrical current in semiconductors is thus based on electrons and/or electron holes as charge carriers [91].

Semiconductors are roughly divided into the following three groups: i) elementary, ii) compound, and more recently iii) organic semiconductors. The most noted one is silicon, which belongs to the group of elementary semiconductors with four valence electrons [91, 92].

Materials of the compound group are mixtures of elements with four valence electrons on average. Those are combinations of elements of the III. and V., II. and VI., I. and VII. main group of the periodic table. Though not necessarily equipped with four valence electrons on average, materials with specific resistances between  $10^2 \Omega \text{ cm}$  and  $10^8 \Omega \text{ cm}$  are allocated to this second group as well [93]. Organic semiconductors include small molecules as well as semiconductive polymers that are mainly containing carbon and hydrogen [93].

Carefully modifying the crystal structure with dopants in very low concentrations allows to deliberately alter the electrical and optical properties. In particular, the addition of III. and V. group elements effectively changes the conduction behavior. The latter, such as phosphorus, add an additional electron to the intrinsic semiconductor, which results in a slight excess of negative charge – thus known as an n-doped semiconductor. Likewise, adding third group elements, e.g. boron, results in positive excess charge and is thus known as p-doping, respectively. To remain in the picture of the band structure, in n-doped semiconductors the donor energy level is close to the conduction band, which effectively lowers the band gap for donor electrons to overcome. For p-doped materials the electron-hole energy level is close to the valence band electrons and allows them to occupy the acceptor level at lower energies than in the intrinsic semiconductor. Especially the combination of n- and p-doped semiconductive materials is of interest for microelectronics. Those materials exhibit new properties as for example one-directional current conduction [91, 94, 95].

The applications of semiconductors within the field of electronics are manifold. The combination of differently doped materials allows designing discrete semiconductor devices, such as diodes and transistors. Even the preparation of more complex integrated circuits with various devices are possible. Integrated circuits include microprocessors, microcontroller, as well as devices of power electronics (i.e., insulated-gate bipolar transistors, thyristors and diodes) [96]. Organic semiconductors, however, are usually applied for light-emitting diodes or photovoltaic cells [93].

The possibility and the desire for the generation of powerful electronic devices equipped with integrated circuits on the one hand, causes complex and expensive manufacturing processes on the other hand.



### 2.2.2. Semiconductor manufacturing processes

The fabrication of integrated circuits starting from raw materials embraces several steps. Beginning with wafer preparation and wafer fabrication, followed by wafer testing, assembly and packaging, and a final testing.

#### 2.2.2.1. Bulk crystal growth and wafer fabrication

The standard method to grow single crystals, including silicon, was introduced by Czochralski in 1918 [97]. A schematic diagram of this technique is given in Figure 11. Herein, the raw material is first melted in a crucible. A seed crystal, mounted in a suspension on top of the melt surface, is slowly rotated upward, which causes a continuous crystallization process. A surrounding inert gas flow (Ar) is usually used to restrain impurities. With this method, cylindrical, single crystals of up to 30 cm in diameter are reported [94]. A variation is the Liquid-Encapsulated Czochralski (LEC) method, particularly suited for GaAs and InP crystals. Here, a layer of molten boron oxide separates the melt from air to prevent volatile anion vapor from escaping [98, 99]. The Bridgman technique is another variation based on the Czochralski method. It applies an additional temperature gradient along the crucible and holds the temperature around the seed crystal slightly below the melting point [92, 99].

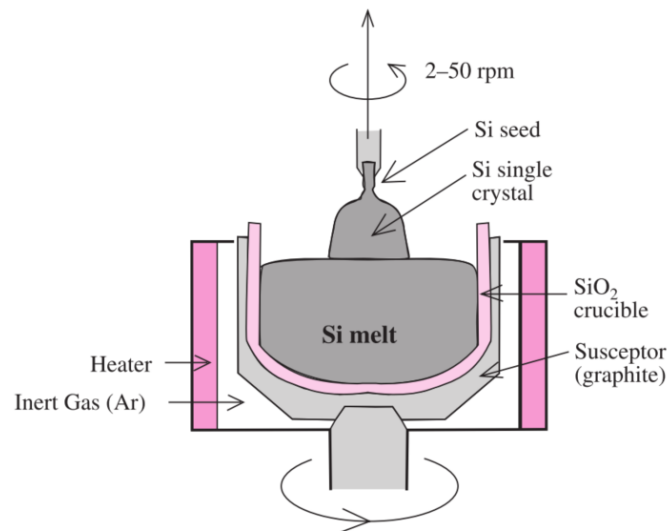


Figure 11: Schematic of Czochralski technique for growing of Si single crystals [92].



*Wet oxidation:*



Wet conditions result in higher SiO<sub>2</sub> growth rates, however, lead to lower densities due to trapped hydrogen molecules in the oxide lattice [94].

High quality metal films require outstanding conductivity, excellent adhesion to the wafer surface, high-resolution patterning, high corrosion resistance and reasonable mechanical strength. The most common materials are aluminum, aluminum-copper alloys, copper and silicides. The simplest method for metal deposition is evaporation of the material in a vacuum chamber, however, physical vapor deposition (PVD) through sputtering of the target material, metal chemical vapor deposition (CVD) and copper electroplating are the methods of choice nowadays [100, 101].

## 2. *Polishing*

A smooth surface is essential for the reproducibility of the device properties. The most common polishing technique is chemical mechanical planarization (CMP). It uses a slurry with certain chemicals and abrasive particles in which the wafer is precisely rotated between polishing platen [102].

## 3. *Diffusion: Epitaxial techniques*

As mentioned before, in many cases only doped semiconductors and their specific combination lead to the unique and characteristic properties of electronic devices. From an economical point of view, it is more favorable to apply these high-quality compositions in thin layers on bulk substrates of lower quality. The epitaxial technique helps to grow such layers on substrates and facilitates nearly identical lattice-parameters between both to reduce strain-related issues. Depending on the similarity or dissimilarity of the chemical composition of layer and substrate, this method is known as homo-epitaxy or hetero-epitaxy, respectively [87, 92]. Epitaxial layers are applied with less than 1 μm thickness, starting from either solid, liquid or gas phase precursors. The latter, however, are the most precise to control the process. E.g., the chemical vapor deposition according to the following reaction yields silicon films of outstanding purity [92]:



The reaction is quantitative, H<sub>2</sub> is easily removed and side reactions are virtually absent. Furthermore, the gas phase composition is easily varied with dopants, such as the pentavalent element phosphor and arsenic in their hydrogenated forms phosphine (PH<sub>3</sub>) and arsine (AsH<sub>3</sub>), respectively. In case of GaAs, the gaseous metal-organic trimethyl gallium [Ga(CH<sub>3</sub>)<sub>3</sub>] is commonly added for elemental gallium insertion into the lattice structure. Hence GaAs films are grown according to the reaction R.2.31 [103, 104].



CVD processes are typically operated at pressures above 1 mbar [92, 103, 105]. A modification under vacuum conditions is the Molecular Beam Epitaxy (MBE) [106], which introduces the reagents in form of molecular beams. Those are generated by vaporization of the precursor within a cell and subsequent escape through a small nozzle into the UHV (ultra-high vacuum) region as well-collimated beams. However, the reactant concentration at the substrate and thus the crystal stoichiometry is difficult to control in MBE [92].

#### 4. Photolithography

Photolithography allows to precisely structure wafer surfaces with three-dimensional patterns [87, 107]. In short, the desired geometry is transferred with an intense light source from a photomask to a photoresist layer on the wafer. The illuminated areas become more or less soluble, known as positive or negative resists, respectively. Subsequent washing out leaves the desired structure. Photolithography is a multi-step process as shown in Figure 13 [100, 107, 108].



Figure 13: Flow chart of the photolithography multi-step process.

In more detail, the wafer surface is first cleaned, released from moisture and primed (**vapor prime**). A **spin coating** technique evenly applies the photoresist layer on the wafer surface

with a precisely defined thickness. Commonly, the photoresist is a polymer resin with a light sensitive additive, e.g., novolak in combination with DNQ (Diazonaphthoquinone) [107, 109]. Once coated, a **soft bake out** removes residual solvent and enhances the adhesion to the substrate. The following **alignment and exposure** step renders the actual imprint. Here, the photomask is precisely aligned to the wafer within the optical pathway of an intense UV-light source. This can be either an excimer laser (ArF: 193 nm or KrF: 248 nm) or a mercury arc lamp at 365 nm, 405 nm, 436 nm [109]. Lower wavelength for higher spatial resolution are still subject to current research. Depending on the type of photoresist, the UV light increases or decreases the solubility of the illuminated areas, which is known as positive and negative lithography, respectively. A **Thermal post exposure bake** is used to stabilize and harden the developed photoresist. Additionally, remaining traces of the coating solvent or developer are removed [87, 107, 109]. Within the **develop** process the photoresist and its residues are removed. Non-postbaked positive photoresists are treated with acetone, trichloroethylene and phenol-based strippers, whereas negative photoresists are developed with methyl ethyl ketone or methyl isobutyl ketone [110]. Another effective method for the removal of organic polymers is plasma etching with O<sub>2</sub> [87]. Finally, any residual solvent is evaporated and the resist is hardened with a post-development thermal **hard bake** [100, 107, 109].

### 5. *Dry and wet etching*

As mentioned earlier, etching removes unneeded material from the wafer surface, either chemically or physically. The two crucial figures of merit for this process are selectivity and isotropy of the removed material. In some cases, etches undercut the masking layer, which results in so called bias. Isotropic etchants show large bias as they erode the substrate in horizontal as well as in vertical direction [87, 111]. Those two figures of merit significantly depend on the chosen process (dry or wet etching) and on the combination of used chemicals, masking layer and substrate material. In a dry etching process, a plasma at around 10<sup>-3</sup> to 5 mbar [112] generates sufficient chlorine or fluorine radicals from precursors, such as CHF<sub>3</sub>, to react with surface molecules and gradually remove them [111]. In wet etching processes, the wafer is immersed in a bath of a liquid-phase etchant, for which a wide range of different specialized types is available. The right etchant depends on the surface and substrate material [87]. For silicon dioxide on a silicon substrate, e.g., buffered hydrofluoric acid is the most common one [113].

## **6. Ion Implantation**

This technique allows to implant dopant material very precisely into the crystal structure of semiconductors. The concentration and penetration depth are well controllable, however, the latter is rather restricted to a few nanometers, in contrast to CVD [114]. The process is operated at high vacuum conditions, with an accurately collimated and accelerated ion beam, which is scanned across the wafer surface. The ions penetrate the surface, are slowed down by collisions with substrate molecules and eventually stop in the lattice. The dissipated kinetic energy locally destroys the crystal structure. This requires a subsequent annealing procedure to finally enclose and electrically activate the implanted atoms [101, 114, 115].

### *2.2.2.3. Wafer inspection*

A number of different analytical methods is available for the inspection of the fabricated wafers. Secondary-ion mass spectrometry (SIMS) is a method of eroding a wafer surface with accelerated ions to analyze the surface material composition with mass spectrometry. Atomic force microscopy (AFM) allows to map the topography of the wafer surface. Auger electron spectroscopy (AES) and X-ray photoelectron spectroscopy (XPS) are used to identify surface chemical species with penetration depth of up-to 2 nm [101]. Beneath AES further scanning electron microscopy (SEM) methods are known using different detectors. Silicon crystal point defects and other small features are analyzed and quantified by the application of transmission electron microscopy (TEM). Element identification is possible with energy-dispersive spectrometers (EDS) [116]. This method uses an electron beam to excite atoms in the probe and detect the emitted, element specific X-ray [117]. Similar to SEM a focused ion beam (FIB) carves thin cross sections from the wafer surface and allows to analyze the removed material [87, 101].

### *2.2.3. Zeiss SMT and semiconductor industry*

Some of the main aspects in wafer treatment with photolithography have only been briefly touched, such as the spatial resolution dependency on the wavelength. With an excimer laser at 193 nm, structures of minimum 38 nm are obtained [118]. For lower critical dimensions more sophisticated systems are needed. A recent development, impelled by

ASML<sup>1</sup>, is Extreme Ultraviolet (EUV) photolithography [119, 120]. The light source in EUV is a laser-induced plasma emitting light at 13.5 nm, which offer the potential of structures on the wafer below 10 nm [118]. The particular challenge in EUV photolithography is that all matter absorbs EUV light. Hence, all optical elements for imaging must be made of reflective lenses (mirrors) instead of refractive lenses. This requires alternating molybdenum and silicon coatings with up-to 100 layers, which reflect the light through interlayer interferences [121]. Theoretically, such mirrors reflect 72 % of the incident EUV light. However, this requires certain precautionary measures, such as precisely flattened mirrors with less than 2 nm deviation from planarity over 30 cm mirror diameter, low vacuum conditions and prior outgassing of any material that is introduced to the chamber. Contamination that may affect the system's optical transmission has to be avoided by all means. "A single fingerprint on the wall of the vacuum chamber could put the whole system out of specifications." [118]. This clearly emphasizes the importance of highest purity throughout the entire process.

Incidentally, the role of Carl Zeiss SMT within the semiconductor industry gains in importance. Carl Zeiss SMT provides optical elements with lenses for photolithographic systems operating with light sources at 248 nm and 193 nm. As Carl Zeiss SMT and ASML connects a long-standing strategic partnership since 1992, the mirror system needed for EUV applications are manufactured in collaboration as well.

---

<sup>1</sup> ASML with its headquarters in Veldhoven (the Netherlands) was founded in 1984 and is one of the world's leading manufacturers of chip-making equipment.

## 2.3. Zeiss-Project GAMMA: Gas multimode mass analyzer

As pointed out in the previous chapters, manufacturing processes in the semiconductor industry are rather sophisticated and expensive. In this context, profitability demands for careful and elaborate process control in particular with respect to the purity of chemicals, contamination of chambers and the exact timing of process steps, e.g., the switch between CVD gases. Advanced control means advanced process monitoring as well. In this regard, the application of appropriate analytical instrumentation is indispensable. In particular, the development in the field of mass spectrometry has seen tremendous improvement in recent years and is still growing. Its application in process monitoring, however, is still in the launch. Thus far, analysis, especially residual gas analysis of processes, are commonly carried out with simple quadrupole devices. Those benefit from compact designs and cost-effectiveness. However, they are insensitive and mostly restricted to nominal mass resolution.

The GAMMA project by Carl Zeiss SMT GmbH develops a novel mass spectrometric system for process gas analysis – the iTrap®. The primary field of application is focused on the semiconductor industry, which is largely related to the general closeness of the Carl Zeiss group to the modern realm of semiconducting research and manufacturing (cf. chapter 2.2.3).

### 2.3.1. Required specifications and operational parameters

The discussed process environments stipulate the required specifications and operating conditions for such a mass spectrometer. i) A slim and compact design is necessary to directly attach the instrument to a process chamber. This avoids long sample lines. ii) The control of processes requires analytical results within real-time, in order to facilitate an appropriate responding cybernetic system. iii) The vacuum system, the sampling procedure and the built-in materials need to be suitable for chemically rather demanding matrices, such as  $\text{AsH}_3$ ,  $\text{SiH}_4$ ,  $\text{B}_2\text{H}_6$ , or  $\text{Ga}(\text{CH}_3)_3$  in  $\text{H}_2$ . iv) The sample pressure is typically at medium and high vacuum conditions. v) Information about trace contamination, e.g., from outgassing materials or solvent residuals, as well as main gas components are of interest. This necessitates a dynamic range over several orders of magnitude. vi) The instrument should feature appropriate mass resolution and mass accuracy.



### 2.3.2. *Fourier Transform Quadrupole Ion Trap*

A number of different MS systems were discussed in chapter 2.1. Undoubtable, the diversity of available instruments covers a wide range of application fields. At least one of the known devices on the market can certainly as well fulfill the required specifications for the targeted application in the semiconductor industry with regard to mass range, mass resolution and sensitivity. For appropriate process gas analysis, however, instrument compactness, robustness as well as the costs for the entire system are equally important factors. For example, enhancing the mass resolution of simple quadrupole devices inevitably increases the manufacturing costs for more sophisticated rods. This consequently weakens the price argument. In addition, most commercially available instruments are not designed for the chemically rather reactive conditions.

The GAMMA project tries to address all the required specifications with a quadrupole ion trap that deploys Fourier transform based non-destructive ion detection. In-trap electron ionization and the absence of an external detector keep the setup slim and compact. Furthermore, the image current detection with subsequent FT analysis, as already discussed for FT-ICR instruments and the Orbitrap, enable favorable mass resolution. To address the chemically demanding environments, a layer of inert metal coats the entire QIT surface.

#### 2.3.2.1. *Challenges: Electronics and first approaches*

The FT-QIT development faces several challenges concerning the technical details as well as the analytical application to real-world samples. These are discussed in the following.

Since the mid-eighties, several approaches for ion traps with non-destructive detection techniques and subsequent Fourier transformation were reported. However, all currently available commercial ion traps operate in the scanning mode with external ion detection. This fact clearly indicates that the establishment of FT based ion traps is a challenging task. In 1987, Syka and Fies were one of the first to meet this challenge [122]. They deployed a sinusoidal voltage pulse between the two endcap electrodes for ion excitation and detected the resulting image current with subsequent FT analysis of this transient signal. With an amplifier bandwidth of only 2.3 kHz only a small mass range is detectable (approx. 1-2 Da) [122]. Goeringer et al. conducted experiments with repeated measurement efficiencies of the same

ion population of 99% [123]. They used a resonant ion excitation scheme (79 kHz), which only enabled the detection of a specific  $m/z$  ratio within a single mass spectrum. Ramping of the RF amplitude and hence sweeping the secular frequencies of the trapped ions through the resonance excitation frequency allowed the record of a full mass spectrum (52 – 169 Da) [123]. In 1996 Cook's group presented a broad-bandwidth ion detection with up-to 400 kHz detector bandwidth [124]. Their system comprised a small detector electrode embedded in one of the endcap electrodes. This design allowed narrow-band AC, as well as broadband SWIFT (stored waveform inverse Fourier transform) excitation. In subsequent work, Cook's group filed a patent on a FT-QIT, in which the ion trap electrodes are used for image current detection in combination with a wide-bandwidth low-impedance preamplifier and a RF trapping voltage filter [125]. Aliman et al. have also realized a broadband excitation of ions and broadband image current detection on the endcap electrodes. Their approach, however, focused on the high crosstalk between the high-frequency storage field and the detector electrodes. In this regard, it is noteworthy that currents induced by the RF field are in the range of mA, whereas ion signal currents are in the fA range [70, 126]. This results in complete saturation of the charge amplifier owing to the interfering capacities. Aliman et al. worked around this crosstalk and applied a compensation current equally to the noise current with inversed sign. A low-noise amplifier subsequently amplified the compensated current signal [70, 126].

### *2.3.2.2. Challenges: For analytical applications*

The overall instrument compactness with direct inlet of the neutral sample into the ion trap and subsequent in-trap ionization, ion excitation, as well as FT-based ion detection is the most challenging task for analytical applications. Especially the pressure conditions brought along by the direct gas inlet and necessitated for the different steps within a measurement cycle are strongly contrasting. A pulsed direct gas inlet with upstream pressures in the lower mbar range leads to an elevated gas and thus an elevated analyte density, which allows an efficient ionization by filament driven electron ionization. FT-based mass analyzers, however, require pressures of at least  $10^{-6}$  mbar (for ultra-high mass resolution in FT-ICR and Orbitrap instruments even  $10^{-10}$  mbar) during the period of ion storage and current detection. These conditions enable sufficient coherent ion movement to record transient signals for appreciable

mass resolution [9, 75, 76]. Hence, pressure conditions for efficient ionization and optimum FT analysis are in stark contrast. Furthermore, the elevated particle density present within the ion trap favors the occurrence of ion-molecule reactions modifying the initial ion population. An additional critical parameter is given by the total amount of ions present within the ion trap. Since EI is known as a non-selective ionization method [9, 10], any matrix ions will be ionized in large abundance. The influence of the electrical fields on the ion population is then affected, potentially causing space charge induced effects [127–130]. At low analyte mixing ratios these effects will gain in importance as elevated ionization times are required and thus matrix ions are generated in large excess. A FT phenomenon known from FT-ICR is coalescent coupling of different ion species, especially at elevated charge densities [131–133]. At least, a spatially distributed ion generation inside the ion trap volume is expected since the electron beam will be strongly affected by the applied RF field.

The above mentioned operational conditions and resulting effects will strongly affect several analytical figures of merit, such as mass resolution, sensitivity, detectable mass range, as well as the dynamic range of the signal response.

### 2.3.2.3. *Advanced ion excitation schemes*

Once trapped, the ions orbit with defined frequencies inside the trapping volume. This condition enables advanced excitation schemes that stimulate the entire ion population or just certain  $m/z$  ranges. A short rectangular DC pulse of some  $\mu\text{s}$  causes a broadband excitation of the entire ion population [52, 134], whereas a sinusoidal signal excites ions of a specific  $m/z$  ratio [122, 135]. The applied signal length and signal amplitude, which correspond to the transferred energy, strongly determine if the ions are simply promoted on higher, stable orbits or even forced against the wall where they discharge [66, 136].

A further, powerful tool in ion excitation is SWIFT [136–138]. Those signals are so called chirps and are superposed by a large number of different ion resonant frequencies or frequency ranges. It is possible to adjust the applied energy for selected sections of the frequency spectrum to either excite or eliminate certain ion species [136]. To some extent, SWIFT allows suppressing unwanted matrix ions and promoting signal intensities of minor components.

### 2.3.3. *PTC and ipaMS within the project "GAMMA"*

As part of the "GAMMA" project, the Physical and Theoretical Chemistry (PTC) and the Institute for pure and applied mass spectrometry (ipaMS) at the University of Wuppertal assume the task of detailed examination of the developed FT-QIT. These investigations encompass the technical boundaries (compactness, etc.) of the entire system, the in-trap electron ionization method and its comparability to common spectra databases, the occurrence and extent of ion-molecule chemistry, the impact of space charge effects, and the impact of transient pressures along sampling, ionization, storing and detection. The findings will lead to a better understanding of the adjustable parameters and their weighing within the measurement cycle. Eventually, benchmark experiments with process gases will demonstrate the analytical performance in particular with respect to i) sensitivity, ii) dynamic range, iii) mass resolution, and iv) mass accuracy. This performance is compared to two commercially available mass spectrometers, a TOF instrument and a quadrupole based RGA, all connected to the same sample chamber.

The validation of the FT-QIT performance and the feasible coupling to an ion transfer stage with external ionization are ongoing tasks handled by PTC/ipaMS.

### 3. Experimental

The entire setup consists of a dynamic dilution stage and a mixing chamber for gaseous sample preparation. The benchmark instruments - a residual gas analyzer and a time of flight mass spectrometer – as well as the Fourier transform based quadrupole ion trap are coupled to this mixing chamber.

#### 3.1. Benchmarking instruments

##### 3.1.1. MKS Residual gas analyzer

###### *Instrument specifications*

A commercially available residual gas analyzer that is currently applied for routine analysis in the semiconductor manufacturing industry is the Microvision 2 residual gas analyzer manufactured by MKS (cf. Figure 14) [60]. It is a quadrupole analyzer equipped with a pre-filter to protect the main filter from contaminations and is used as one of the benchmark devices in this work. The mass analyzer is connected via a CF flange to a process chamber. The overall compact and robust design allows the application even in processes under harsh conditions. The RGA is equipped with two independent filaments to minimize monitoring downtime. The electron energy is adjustable in the range of 20 – 100 eV, allowing to record EI spectra matching database entries (e.g. NIST Chemistry WebBook [139]). Data acquisition speed is less than 3 ms per point for analogue scanning. The mass range is up-to 300 Dalton. A Faraday cup and a microchannel plate detector allow the measurement of partial pressures<sup>2</sup> of  $2 \cdot 10^{-11}$  mbar and  $5 \cdot 10^{-14}$  mbar, respectively. With the maximum operating pressure given by  $1 \cdot 10^{-4}$  mbar the partial pressures can be converted into mixing ratios, resulting in 2 ppmV for the Faraday cup and 5 ppbV with the MCP. Mass resolution is limited to nominal masses with a resolution better than 10 % valley for peaks of similar height. Operating temperatures up-to 200 °C are tolerable while keeping the temperature of the electronics in the range of 10 – 40 °C.

---

<sup>2</sup> The declaration of partial pressures is an established quantity used within the residual gas analyzing community.



Figure 14: MKS Microvision 2 residual gas analyzer [140].

The residual gas analyzer is mounted in a separately pumped vacuum chamber that is connected to the analyte mixing chamber via a small orifice ( $5\ \mu\text{m}$ ). This allows suitable operating pressures for the RGA with the analyte present at elevated pressures of several mbar up-to 1 atm within the mixing chamber.

#### *Analytical Performance*

Since the residual gas analyzer is applied as it is commercially available, analytical performance can hardly be enhanced. Measurements carried out with toluene diluted in nitrogen show an analytical performance that is almost reaching the instrument specifications given by MKS. The analysis of 100 ppbV arsine in hydrogen, however, was not successful. The exact position of the RGA in the second vacuum chamber has not been determined. The RGA ion source can be positioned closer to the inlet orifice allowing an incident flow that may provide an improved analytical performance, but this was not within the scope of the present work.

Despite the limited analytical performance with regard to mass resolution and limit of detection (LOD) there is a number of advantages of the RGA especially for the envisioned applications. Since the analysis time is 3 ms per data point, measurements for a narrow, defined mass ranges are quite fast. Furthermore the RGA is a compact, and cost-effective device delivering mass spectra that are searchable in standard databases.

### 3.1.2. Time of Flight mass spectrometer (TOFWERK CTOF)

#### *Instrument specifications*

TOFWERK is delivering OEM (*Original Equipment Manufacturer*) solutions to the mass spectrometry market. The TOFWERK CTOF [141] impresses by its small size with regard to the analyzer system. The TOF chamber dimensions are 26.5 x 17.5 x 11.5 cm<sup>3</sup> (length x width x height). Referring to the system specifications a mass range up-to 4,000 Dalton is reachable with a mass resolution of approx. 1,000, depending on the application. The specification list is extended by a mass accuracy of 4 ppm, an acquisition rate of 2,000 spectra/s in continuous mode and a high dynamic range over 7 orders of magnitude. For ion detection microchannel plates are used.

#### *Plasma-based ion source*

The modular design of TOFWERK instruments enables the coupling of the CTOF with a custom ion transfer stage and thereby with a large number of different ion sources. For the benchmark measurements discussed in this work a direct current (DC) helium plasma ion source was used. Helium metastables with electronic energies exceeding 19 eV [21, 22] are generated within the plasma region. As ionization energies of most compounds are generally far below 20 eV, helium metastable induced penning ionization enables ionization of a wide range of compounds. In addition to the direct analyte ion generation via penning ionization (cf. R.2.4/R.2.5), charge transfer processes from matrix and background ions, that are typically also generated in large amounts, have to be taken into account. In case of nitrogen as matrix gas and in the presence of water at typical mixing ratios of several ppmV, reaction cascades as discussed for APCI in chapter 2.1.2 occur. The primary plasma region and the ion source are separated by an orifice of 100  $\mu\text{m}$ . The flow conditions within the plasma source lead to an ion source pressure of approx. 1 mbar.

#### *Custom ion transfer stage*

Ions which are generated in the source chamber need to be transferred from the 1 mbar region into the analyzer region, held at 10<sup>-6</sup> mbar. Figure 15 shows a schematic of the interface used in this work.

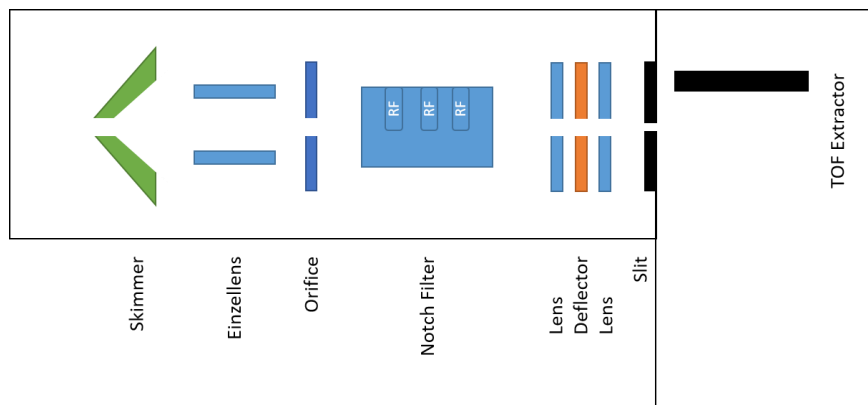


Figure 15: Schematic of the custom CTOF interface.

Differential pressure reduction to  $10^{-3}$  mbar is maintained by gas flow restriction [skimmer (1) with an orifice of 1 mm]. Downstream, ions are collimated by an Einzel lens (2) and delivered to the next pressure stage ( $10^{-5}$  mbar) via an orifice of 2 mm diameter. Ion optical elements are not only used for ion guidance along the differentially reduced pressure, but also enable a targeted manipulation of the ion population. As mentioned He plasma based chemical ionization leads to a large amount of background and matrix ions. If those large ion ensembles impinge on the MCP detector, a recovery time is necessary until the MCPs are discharged. Within that time the detector is called to be *blind*. Therefore a quadrupole notch filter (3) is applied, allowing the removal of up-to four different  $m/z$  ratios. Attention should be paid on the influence on other  $m/z$  ratios, especially when higher removal energies are applied. Before entering the analyzer region ions are focused within a lens – deflector – lens arrangement.

#### *Coupling to the mixing chamber*

Analyte sampling was achieved in two ways: i) Either by coupling the CTOF sampling stage with an orifice of 300  $\mu\text{m}$  to the mixing chamber or ii) via a 18 cm metal capillary (ID 0.5 mm). In both cases upstream pressures up-to 1 atm are tolerated. The capillary in the latter is mounted in a 6 mm tube allowing the addition of a sheath gas flow coaxially to the analyte gas stream (cf. Figure 16). Depending on the sheath gas used either the operation of the ion source in charge transfer (CT) or proton transfer (PT) mode is possible. In case of CT the analyte is either directly ionized by penning ionization (cf. R.2.4/R.2.5) or by charge transfer from reactant ions as discussed in R.2.19 – R.2.21. Upon addition of hydrogen to the sheath gas the operation in PT mode is enabled since penning ionization leads to the formation of  $\text{H}_3^+$



ions according to the reactions R.3.32 – R.3.36. As  $\text{H}_3^+$  is a very strong gas phase acid the protonation of any analyte with a higher proton affinity than  $\text{H}_2$  is energetically favorable.

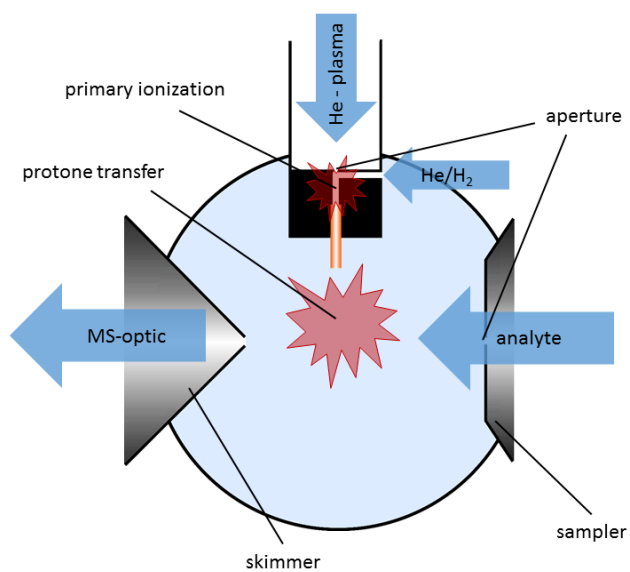


Figure 16: Schematic of the capillary based analyte inlet to the ion source enabling measurements in CT and PT mode [142].

### Analytical Performance

Total ion currents measured within the ion transfer (between Einzel lens and Notch filter) reached several nano Amperes, necessitating the removal of background ions within the Notch filter on the one hand but allowing an efficient ionization of the analyte on the other hand. With the above depicted setup 5 pptV toluene diluted in nitrogen at 500 mbar total pressure are measured in charge transfer mode as well as 50 pptV toluene in nitrogen in proton transfer mode. The spectra integration time is set to 60 s. Since the  $S/N$  ratios are still high ( $> 20$ ), LODs are assumed to be below 5 pptV (CT-mode) and 50 pptV (PT-mode), respectively.

As the number of reactant ions is exceedingly high a linear dynamic range over 5 orders of magnitude is reached. Figure 17 shows a measurement carried out in a combined CT and PT mode. The xenon mixing ratio is kept constant at 10 ppmV whereas the mixing ratio of toluene is increased from 10 ppbV to 400 ppmV, both diluted in nitrogen. The protonation rates of xenon and toluene remain constant (Figure 17, secondary axis) over the full range of the toluene mixing ratios. This strongly suggests that the protonation capacity is even much higher; otherwise reactions leading to an increasing  $Xe^+/[Xe+H]^+$  ratio occur. The mass resolution of the investigated ion peaks is on average 1,000 fulfilling the above mentioned device specifications.

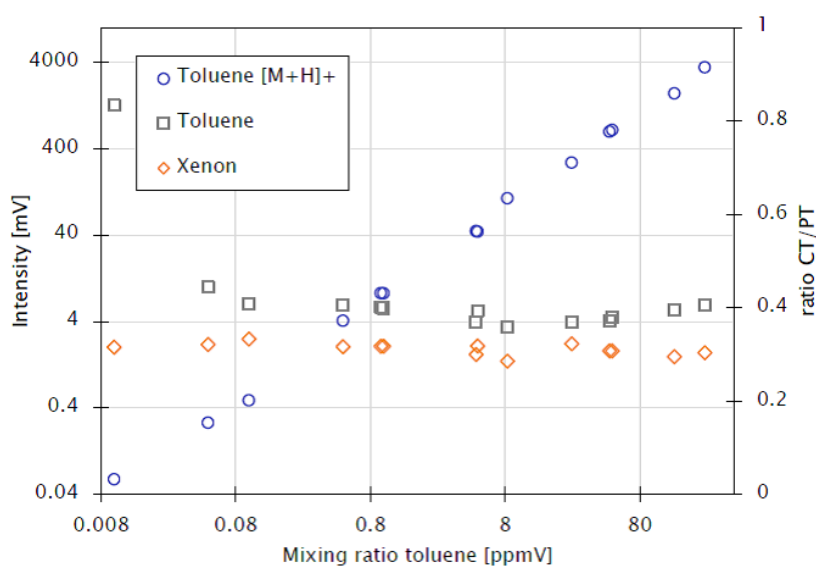


Figure 17: Signal response of toluene  $[M+H]^+$  in dependence of the analyte mixing ratio. The ratio of CT vs PT products observed for xenon and toluene are plotted on the secondary axis [143].

The analytical performance parameters obtained for the benchmark analyte toluene in nitrogen are outstanding. A transfer of this performance to process specific gas mixtures is also possible. However, two issues need to be considered:

1. An analysis of potentially occurring degradation processes on the multichannel plates while continuous operation in hydrogen with process gases such as HCl has not been carried out, as the majority of measurements was examined in nitrogen.
2. The above presented measurements are carried out with a sample pressure of 500 mbar. Thus, optimum operation conditions within the ion source are reached. In addition significant viscous drag into the ion transfer region is present. Some of the targeted applications, however, only offer pressures up-to 10 mbar. Sampling from lower pressure results in lower analyte signal responses and thus higher limits of detection, since the absolute number of generated ions and the viscous drag is reduced.

A detailed description of the micro-plasma based chemical ionization source including the coupling stage to the CTOF is given in the dissertation of David Müller [144].

## 3.2. FT-QIT: Zeiss Demotool

### 3.2.1. Setup

A three-dimensional quadrupole ion trap (similar to a Paul trap, cf. Figure 18) represents the heart of the entire FT-QIT setup. An almost ideal electrical quadrupole field is established due to the application of hyperbolic electrodes. Two endcap electrodes and a ring electrode embrace a trapping volume of approx.  $3 - 5 \text{ cm}^3$ . The RF trapping field is applied onto the ring electrode with a frequency of 1 MHz and voltages ranging from  $0 - 500 \text{ V}_{\text{RF}}$ , which is  $0 - 1,000 \text{ V}_{\text{pp}}$ . Endcap electrodes are tied to ground potential, leading to an  $a$ -value of zero. Comparison to Figure 5 (p.16) shows that in this case the widest mass range is achievable with the operating line along the  $q$ -axis. The ion trap is equipped with a filament mounted on the ring electrode for in-trap electron ionization. Ion detection is realized by recording image currents induced by ions approaching the endcap electrodes. As already mentioned, such image currents are very small with values in the range of femto Amperes. Thus, equally important than the QIT itself are *QIT-near electronics*.

QIT-near electronics are custom made and include an RF amplifier (RFA), a charge state amplifier (CSA), a filter amplifier (FIA) and a stimulus unit (STM). As overall control unit an Atmega16 microcontroller board is used.

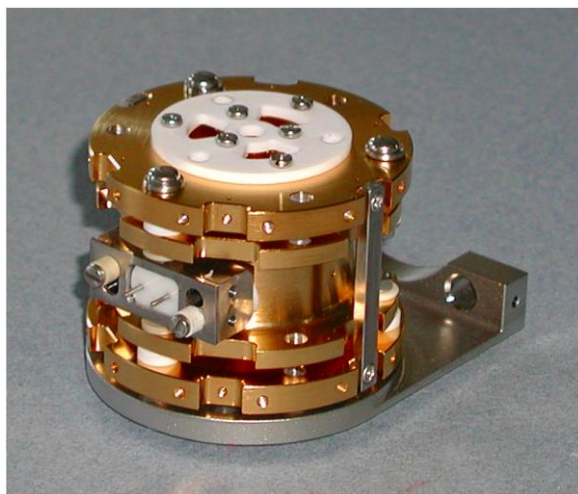


Figure 18: Photograph of the ion trap with gold coated surfaces [145].

The transient ion signals are recorded with an Agilent Technologies oscilloscope (Model: DSO7054A, Agilent Technologies, Munich, Germany) operated in high resolution mode. RF

signal as well as applied SWIFT signals are delivered by an arbitrary waveform generator (Model: 81150A, Agilent Technologies, Boeblingen, Germany).

The FT-QIT is mounted on a CF-flange in a vacuum recipient. Optimum vacuum conditions are provided by a Pfeiffer turbo molecular pump (Model: HiPace 300, Pfeiffer Vacuum GmbH, Wertheim, Germany). All electrical leads are provided via connections on the basis flange.

### 3.2.2. Gas inlet system

Principally the FT-QIT is used in two different operational modes, either residual gas monitoring mode or gas sampling mode. In case of the residual gas monitoring mode the trap is directly mounted into the process chamber that is operated at ultra-high vacuum conditions. No external ionization and ion transfer stage are used. A continuous gas sampling is not possible as ultra-high vacuum conditions in the QIT recipient must be maintained for optimum ion storage and ion detection, especially due to the application of the Fourier transform technique. Thus a pulsed gas sample mode is favored, allowing the injection of a certain gas amount. This gas load is pumped away reaching optimum pressure conditions for FT-QIT measurements within short time. Appropriate short gas pulses are only reachable by the application of fast switching valves. In this work a pneumatically driven Atomic Layer Deposition (ALD) valve (Swagelok, Neuss, Germany) is used with opening times adjustable down to 10 ms. Although other fast switching valves allow shorter opening times, the ALD valve is favored due to a small leak rate ( $1 \cdot 10^{-9}$  std cm<sup>3</sup>/s for helium), an upstream pressure tolerance up-to 10 bar and especially due to the clean and non-outgassing stainless steel sealing diaphragm and valve body [146].

The QIT basis flange features a drilled duct which can be used as additional gas inlet into the QIT recipient with an upstream pulsed valve. Figure 19 shows the two gas delivery stages: Gas inlet via a bended metal tube towards a hole in one of the QIT endcap electrodes (left), and gas inlet via a straight ceramic tube towards a hole in the ring electrode (right).

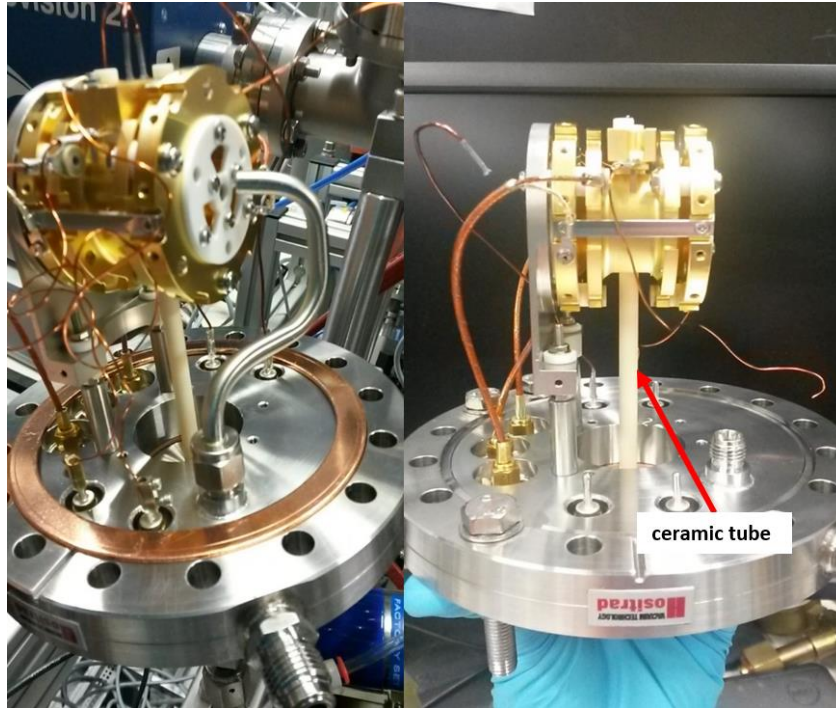


Figure 19: Photographs of the two applied gas inlet designs. Left: Bended metal tube pointing towards the hole in the endcap electrode. Right: Straight ceramic tube pointing towards the hole in the ring electrode.

### 3.2.3. Acquisition parameters

#### 3.2.3.1. Cycle Parameters

FT-QIT measurements depend on a large number of acquisition parameters. One important sub-set constitutes measurement cycle parameters. These parameters are typically defined by a start and a stop time within the entire measurement cycle. In the following the cycle configuration parameters are listed:

*Filament current:* The filament can be turned on and off within the measurement cycle. Most commonly, however, it is turned on for the whole time.

*Gas inlet:* Depending on the inlet valve type, gas inlet times are adjustable down to 10 ms. The upper value is only determined by the gas inlet pressure.

*Anode electron beam:* Defines the gating time for the ionization process. The anode “opens” for a defined time, enabling electrons to enter the trap volume.

*Eject function:* The eject function is needed when further signals, e.g. SWIFT signals, are applied on the endcap electrodes. Within the timeframe given by the eject function such signals can be passed to the endcap electrodes.

*RF gating:* The RF gating is used to empty the trap from ions of a previous measurement by turning the RF trapping field off for several milliseconds at the beginning of a measurement cycle.

*Stimulus time:* The software allows to set up-to two stimulus/excitation pulses. The first excitation pulse is always used as trigger signal for data acquisition with the digital oscilloscope.

*Pulse width:* The pulse width defines the length of the applied rectangular excitation pulse. Typically the applied pulse widths are in the range of a few microseconds.

### 3.2.3.2. *Typical measurement sequence*

Usually the trap is operated in a single cycle acquisition rather than multi-cycle ion accumulation mode. Thus, each measurement cycle begins with turning off the trapping RF for a few ms to empty the trap from remaining ions.

For measurements in the sample mode, the gas inlet valve is opened. Subsequently ionization occurs inside the trap by turning off the anode blocking potential for a selected time. Generated ions are stored inside the trap before being excited by the stimulus (excitation) pulse. Eventually the transient ion signal is recorded and data are transmitted to the measurement software.

With the trap operated in residual gas mode gas inlet is not required and the time for ionization is typically longer, in correspondence to the lower analyte ion density due to the lower pressure conditions.

Two measurement cycles are schematically shown in Figure 20 (top: sample mode, bottom: residual gas mode).

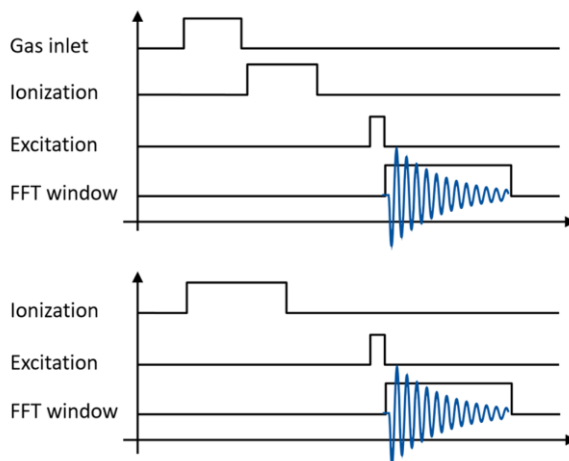


Figure 20: Schematic of the measurement sequence in sample gas mode (top) and residual gas mode (bottom).

### 3.2.3.3. Further acquisition parameters

In addition to the above discussed cycle parameters adjusted within the measurement software, there is a number of further operational parameters.

*Trapping field:* As already mentioned above the trapping field is driven with a frequency of 1 MHz. The voltage amplitude of the trapping field is adjustable between 0 – 500  $V_{RF}$  depending on the mass range of interest.

*Length of transient:* The length for data acquisition of the transient signal is adjusted at the oscilloscope. Typical values are tens of milliseconds in the sample mode and several hundreds of milliseconds in the residual gas mode.

*Filament current:* The applied filament current is dependent on the present filament type. It is noted that the electron emission current is not in linear correspondence to the applied filament current, and thus the latter is not proportional to the amount of generated ions.

*Sample pressure:* The sample pressure is strongly affecting the total gas load of the trap and thus affecting the overall time for data acquisition. This is caused by the required low pressure for the ion detection phase. Sample pressures up-to several mbar are tolerable. Higher sample pressures are handled by an optional upstream pressure reduction unit.



*Background pressure:* The importance of optimum pressure conditions for the ion storage and detection phase has been mentioned several times. The background pressure reached between two measurement cycles is strongly impacting on the trap performance, especially in dependence of the gas composition. If necessary, the dwell time between two measurements needs to be much longer than the typical value of 1 s to avoid a continuous rise of the background pressure with time.

### 3.2.4. Additional excitation schemes

Additional excitation schemes, such as resonant excitation or SWIFT excitation can be applied to the trap at any time within the measurement cycle. The associated waveforms are generated by the arbitrary waveform generator and coupled to the endcap electrodes. Whereas e.g. sine or rectangular signals are already implemented in the waveform generator, SWIFT signals need to be processed before data acquisition. A MATLAB script based on the Goodman algorithm [147] generates SWIFT signal data files of selected mass or frequency ranges with defined relative excitation amplitudes. The data files are loaded via a waveform generating program (Keysight BenchLink Waveform Builder, Keysight Technologies, Böblingen, Germany) into the arbitrary waveform generator. Signal amplitudes up-to 6 V can be applied to the trap electrodes. The lengths of typical SWIFT signals are in the range of several milliseconds depending on the number of transformed ion frequencies. Figure 21 exemplarily demonstrates the resulting chirp signal designed to excite frequencies in the range of 10 to 100 and 200 to 400 kHz.

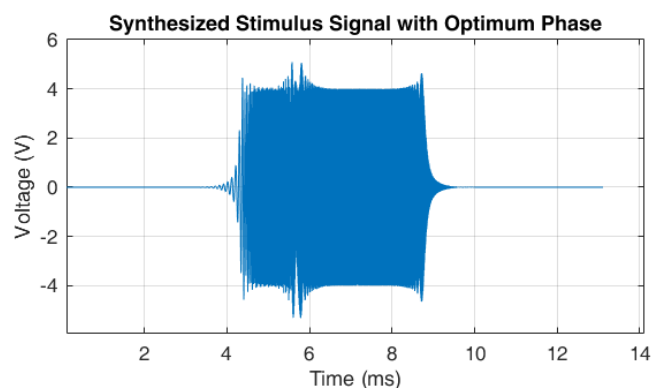


Figure 21: Exemplary SWIFT signal for the excitation of a desired frequency range. Duration of the entire signal is 13 ms.

### 3.2.5. Measurement software: GammaProto

A screenshot of the graphical user interface (GUI) of the GammaProto software is shown in Figure 22. The GUI is divided into two parts: The *ProtoBox Setup* and the *GammaProto main window*. Cycle configuration parameters are set in *ProtoBox Setup* as well as the definition of COM-ports for the communication between software and microcontroller, and the set of mass calibration coefficients. Cycle parameters can either be defined by start and stop values or declared as time intervals with differences between specific events within the measurement cycle.

#### *GammaProto main window*

Within the GammaProto main window a selection of the used devices (oscilloscope, waveform generator, etc.) is possible. In addition to performing new measurements access to previous measurements is enabled. Currently available measurements are contained in the session list (a). On the upper right side the recorded transient ion signal is shown (b). The user may choose the length or area of the transient signal of interest. This part of the transient is analyzed via fast Fourier transformation to generate a frequency or mass spectrum (depending on the user choice) displayed on the bottom right (c). Implemented FFT window functions such as rectangular, Hann or Blackman-Harris can be applied to the transient (d). The software allows the selection of a background spectrum as well as displaying a second mass spectrum (e). Further data analysis is not possible within the acquisition software.

For this purpose the transient signal and a text file, that includes all measurement and data acquisition information, are saved to disk. This allows subsequent external analysis with Fourier transformation methods. Nevertheless even the frequency and mass spectra, calculated within GammaProto, can be exported directly. FFT analysis in GammaProto, however, is less precise.

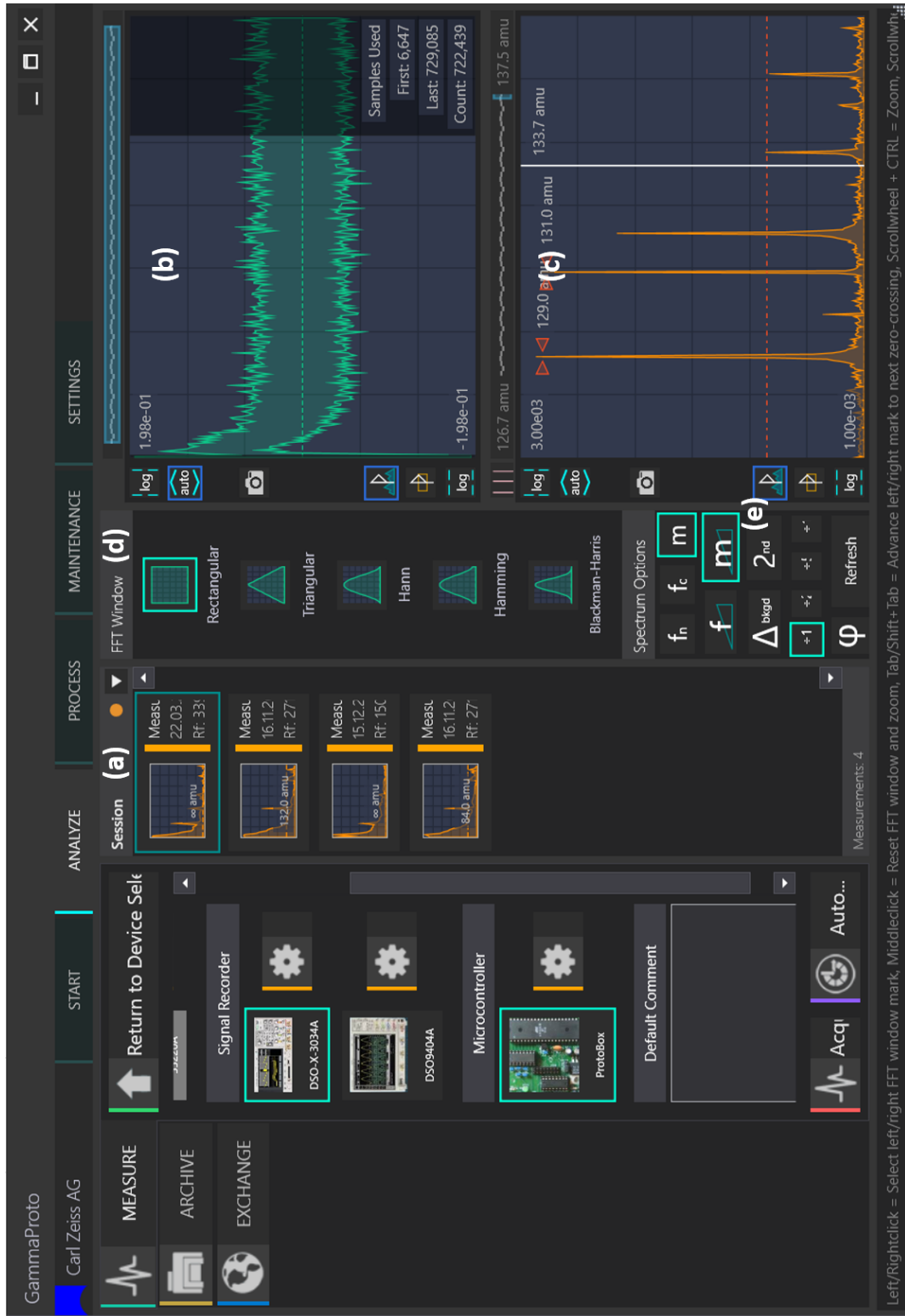


Figure 22: Screenshot of the GUI of the measurement software GammaProto. ProtoBox Setup is not displayed.

### 3.2.6. Ion excitation

Basically there are three different possibilities for ion excitation: i) broadband, ii) narrow bandwidth and iii) resonant ion excitation. Resonant ion excitation is commonly used in scanning ion trap devices ejecting single  $m/z$  ratios for external detection.

In case of the FT-QIT broadband ion excitation is more suitable since typically not only a specific  $m/z$  ratio but a wider  $m/z$  range is of interest. Broadband ion excitation can be reached by the application of a short (some  $\mu\text{s}$ ) rectangular DC pulse or a SWIFT waveform.

Ideally, the ion population is trapped close to the center of the ion trap. Then the excitation pulse should lead to a maximum displacement, so that ions come as close to the endcap electrodes as possible inducing maximum image currents without hitting the electrodes.

From theory and from first experiments it is known that SWIFT excitation brings along a number of advantages as compared to DC pulse excitation. For example,  $m/z$  ratios of interest can be excited while other  $m/z$  ratios are either only weakly excited or even over-excited and therefore removed from the trap. First results on SWIFT application and the usage of SWIFT for the stimulus pulse are presented further below.

Reliable ion excitation is reached by the application of rectangular DC pulses of several Volts. It is noted though that the excitation rate  $\phi$  is a function of ion frequency  $f_{ion}$ . The transformation of a rectangular pulse into the frequency domain via Fourier transformation gives a sinc-function [9, 148]. Herein  $U_p$  is the amplitude of the DC pulse ( $U_p = 12\text{ V}$ ) and  $T_p$  is the pulse duration.

$$\phi(f_{ion}) = U_p \cdot T_p \cdot \text{sinc}(f_{ion} \cdot T_p) \quad (3.28)$$

Figure 23 shows the normalized absolute excitation rate ( $\phi(f_{ion})/U_p \cdot T_p$ ) for a 2  $\mu\text{s}$  and a 4  $\mu\text{s}$  excitation pulse depending on the ion frequency. It is clearly evident that ions of different  $m/z$  ratios will not be excited with the same rate.

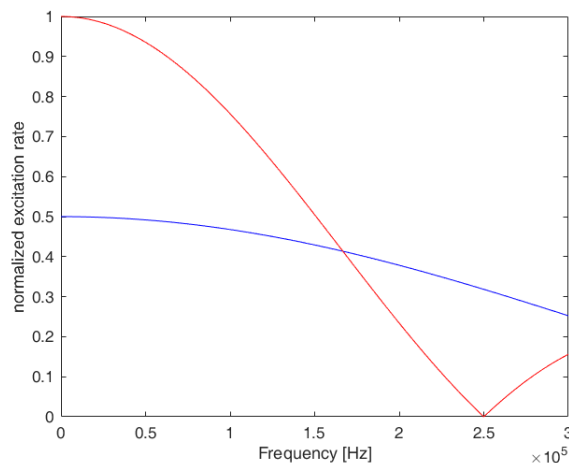


Figure 23: Dependency of the excitation rate on the ion frequency for a 2  $\mu\text{s}$  (blue) and a 4  $\mu\text{s}$  (red) rectangular excitation pulse.

For the application of rectangular excitation pulses further boundary conditions need to be taken into account. For the suitable length of the excitation pulse Aliman suggested [70]:

$$T_p \leq \frac{0.44}{f_{ion,max}} \quad (3.29)$$

Under consideration of the electrical field and trap dimensions the total excitation energy as product of DC voltage and pulse length for ions that are trapped in the center of the trap follows:

$$U_p \cdot T_p \leq \frac{1.905 \cdot V_{RF}}{2\pi \cdot f_{RF}} \quad (3.30)$$

If  $U_p \cdot T_p$  is greater than the expression on the right hand side, overexcitation and subsequent ion loss is expected (a derivation of this equation is given in [70]).

### 3.2.7. Filament driven electron ionization

Ionization within the ion trap is reached by a filament driven electron ionization. The design of the EI source is in analogy to the design of electron guns, with the filament mounted within a Wehnelt cylinder [149]. The anode electrode acts as electron gate and a further electrode is used for focusing the electrons into the entrance hole of the ring electrode of the

QIT. For all measurements two different filament types were used. Most measurement were carried out with a tungsten filament; more recent experiments were performed with an yttrium coated filament with tantalum disc. A comparison of the performance of both filament types remains to be done in future experiments.

### 3.2.8. Plasma coupling

In contrast to the generally used EI source a few experiments were carried out using helium plasma induced penning ionization. A direct coupling of ion trap and plasma source became possible by the application of a T-piece arrangement and the use of a fused silica GC column (ID 0.5 mm) as inlet. A schematic drawing and a photograph are given in Figure 24.

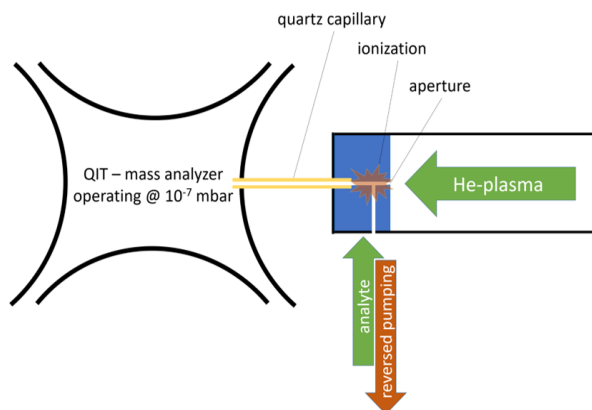


Figure 24: Schematic of the plasma source - QIT coupling [150].

Compared to the plasma source applied for measurements with the CTOF, the plasma source used for QIT experiments is equipped with an additional lid. This lid embraces a small volume (ionization/reaction zone) and is equipped with a lateral gas lead. The primary plasma region is separated from reaction zone with a 10  $\mu\text{m}$  orifice. Via the lateral gas lead the gas sample is introduced into the reaction zone, where analyte molecules interact with helium metastables. The generated analyte ions are transported into the trap via viscous drag through the GC column that connects plasma source and ion trap. Again, gas load is a crucial factor for the QIT performance. Pumping the entire gas load (plasma source gas and sample gas) through the strongly flow restricting GC column requires an extended amount of time until a reasonable pressure for ion storage and ion detection is reached. Thus, for the sample gas inlet

a three-way-valve was utilized, allowing both the inlet of the gas sample and reversed pumping of the gas load.

Note that this kind of coupling is less important for any commercialization of the instrument but relevant for the in-depth characterization of the system. As discussed further below, these experiments yield valuable information on the QIT behavior with regard to ion cooling effects and ion accumulation/repeated excitation experiments.

### 3.2.9. Measurements

Measurements to characterize and to investigate the basic behavior of the ion trap are typically carried out with well-defined gas samples such as mixtures of nitrogen and oxygen as well as aromatic hydrocarbons (i.e., toluene, benzene) diluted in either hydrogen or nitrogen. The advantage of such mixtures is that the chemical behavior is well known. Therefore they are readily usable to examine a number of different effects occurring within the ion trap during the measurement. These effects include space charge induced mass shifts, phenomena as for example coalescent coupling, and ion signal suppression, to name a few. Likewise suited for such examinations are mixtures of xenon and krypton diluted in  $N_2$ , as both rare gases are chemically inert and exhibit a distinct isotopic pattern. In addition experiments are carried out with industrial process specific gases such as diborane ( $B_2H_6$ ) or arsine ( $AsH_3$ ). With regard to residual gas analysis the ion species of interest are typically  $H_2O^+$  and  $H_3O^+$ ,  $N_2^+$ ,  $O_2^+$ ,  $CO_2^+$  and those derived of  $C_xH_y$  compounds. Investigations on the analytical performance of the system are subsequently carried with toluene diluted in either nitrogen or hydrogen.

## 3.3. Analytes and sample preparation

Analyte containing gas mixtures are either purchased from Linde [Düsseldorf, Germany:  $AsH_3$  (100 ppbV in  $H_2$ ; purity: 4.0) and  $B_2H_6$  (50 ppmV in  $H_2$ ; purity: 5.7)] or are custom made, as listed below.

Table 8: Custom gas mixtures.

Analyte	Matrix gas	Mixing ratio
Xe + Kr	N <sub>2</sub>	each 6 ppmV
Xe + Kr	He	each 10 ppmV
Benzene, Toluene, Xylene (BTX)	N <sub>2</sub>	each 10 ppmV / each 10 ppbV
Benzene, Toluene, Xylene (BTX)	H <sub>2</sub>	each 10 ppmV / each 10 ppbV
Toluene	N <sub>2</sub>	10 ppmV / 10 ppbV
Toluene	H <sub>2</sub>	10 ppmV / 10 ppbV

Pure gases are purchased from Messer Industriegase GmbH (Siegen, Germany) and used without further purification (N<sub>2</sub> 5.0, H<sub>2</sub> 5.0, He 5.0, O<sub>2</sub> 5.0, synth. Air 5.0). Liquid analytes (benzene, toluene and xylene) used for the preparation of gas mixtures are purchased from Sigma Aldrich (Seelze, Germany) and gaseous analytes (Xe, Kr) are purchased from Messer Industriegase GmbH (Siegen, Germany).

A dynamical dilution stage equipped with mass flow controllers (MKS Instruments Deutschland GmbH, Munich, Germany) allows the dilution of gas mixtures up to 1:10,000 in different gas matrices (H<sub>2</sub>, N<sub>2</sub>, He).

### 3.4. Simulations and data analysis

All simulations presented in this work are performed by Walter Wissdorf using SIMION and a custom C++ code that is based on fast approximation methods (Barnes-Hut Trees and Fast Mutlipole Method) and allows the calculation of particle-particle interactions [151].

Data analysis of the obtained mass spectra is carried out with mMass [152], an open source mass spectrum analysis software, as well as custom python scripts, which allow data analysis with respect to the determination of signal intensities, peak areas and mass resolution, to name a few.

SWIFT waveforms are calculated in MATLAB scripts based on Goodman algorithm that are provided by Albrecht Brockhaus and Michel Aliman [153, 154].



## 4. Results and Discussion

Analytical performance parameters of the two benchmark instruments have been outlined in chapter 3.1. Since the characterization of the FT-QIT is the central object of this work the current chapter is focused on results obtained with the trap along with their discussion. With the FT-QIT as novel mass spectrometer that combines ionization, mass analysis as well as detection subsequently *within* the analyzer, an understanding of optimum operating conditions becomes distinctively complex. Therefore results from experiments with well-defined boundary conditions are presented. They give an insight into the basic QIT behavior towards different parameters and highlight certain challenges in the QIT operation. This chapter is closing with a presentation of the current attainable analytical performance with the laboratory setup under optimum measurement conditions.

### 4.1. Basic FT QIT settings

#### *Storable and detectable mass range*

The FT-QIT is driven with an RF frequency of 1 MHz. Amplitudes are adjusted at the RF generator and then amplified by the RFA module leading to trapping field amplitudes of 0 – 500 V<sub>RF</sub>. According to equation (4.31) (valid for an *a*-parameter of zero) the lower mass cutoff (LMCO) is solely depending on the applied RF voltage. The upper mass limit, however, is only depending on the mechanical dimensions of the ion trap, since the stability diagram is based on an infinite, ideal quadrupolar field [9, 52, 148].

$$\left(\frac{m}{z}\right)_{min} = \frac{4 \cdot 0.908 \cdot e}{\omega_{rf}^2 \cdot r_0^2 \cdot m_H} \cdot V_{RF} \quad (4.31)$$

with  $m_H=1.66 \cdot 10^{-27}$  kg which is the mass of an H-atom

The effectively detectable mass range, however, is limited by the linear range of the response of the charge amplifier (cf. schematically shown in Figure 25) which is determined by a lower and an upper frequency limit,  $f_{min}$  and  $f_{max}$ , respectively. The ratio of the highest  $(m/z)_{max}$  to the lowest  $(m/z)_{min}$  is about 8 to 10 with respect to the frequency bandwidth of the first stage charge amplifier.

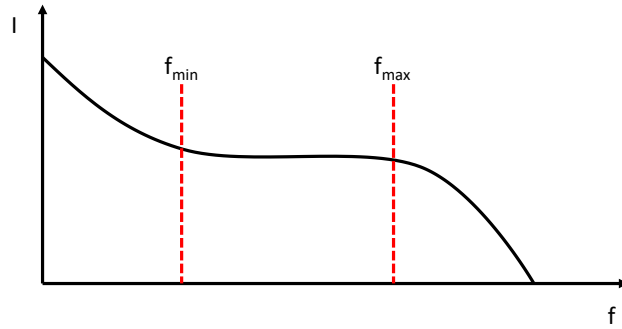


Figure 25: Sketch of the response curve of the charge state amplifier.

### Frequency and mass spectra

The ion resonance frequencies contained in the time-dependent transient signal are analyzed by fast Fourier transformation algorithms resulting in intensity-to-frequency dependencies. With the  $m/z$  ratio inversely proportional to the ion frequency (cf. equation (4.32)), the frequency spectrum is converted into a mass spectrum.

$$\frac{m}{z} \approx \frac{\sqrt{2} \cdot e \cdot V_{RF}}{4 \cdot \pi^2 \cdot f_{rf} r_0^2 m_H} \cdot \frac{1}{f_{ion}} \quad (4.32)$$

### Mass calibration

Ideally mass calibration is performed using several  $m/z$  ratios over a wide mass range to obtain a reliable result. Correlation of  $m/z$  ratio and ion frequency has already been shown in eq. (4.32). Rearrangement to  $V_{RF}$  gives:

$$V_{RF} = \frac{m}{z} \cdot \frac{4 \cdot \pi^2 \cdot f_{rf} r_0^2 m_H}{\sqrt{2} \cdot e} \cdot f_{ion} \quad (4.33)$$

Since the physical dimensions of the QIT and the RF frequency are held constant, equation (4.33) simplifies to:

$$V = \frac{m}{z} \cdot c \cdot f_{ion} \quad (4.34)$$

With  $c$  as the QIT specific constant, the dominating factor is the amplitude of the trapping field.

Parallel to the RF calculation the value for the applied trapping field returned by the analog digital converter (ADC) is recorded. Plotting the ADC value in dependence of the calculated trapping field (based on  $m/z$ - $f_{ion}$ -signal pairs in the mass spectrum) a straight line is observed, which is characterized by a negative slope and a positive  $y$ -intercept. The value of the negative slope is assigned to the ADC ratio giving the counts per volt and the  $y$ -intercept is assigned to the ADC offset giving the entire number of counts. Both parameters are input parameters in the ProtoBox Setup and are considered as the frequency to mass conversion factor. In the following an exemplary mass calibration is demonstrated:

Considered are ion signals corresponding to water and nitrogen in residual gas measurements and ion signals corresponding to toluene while the QIT is operated in the gas sampling mode. Ion signals observed are  $\text{H}_2\text{O}^+$  ( $m/z$  18) and  $\text{H}_3\text{O}^+$  ( $m/z$  19),  $\text{N}_2^+$  ( $m/z$  28), as well as  $\text{C}_7\text{H}_7^+$  ( $m/z$  91) and  $\text{C}_7\text{H}_8^+$  ( $m/z$  92). Table 9 shows the  $m/z$  ratios, the measured value of the ADC and finally the calculated RF voltage. As further input parameter the ion frequencies corresponding to the  $m/z$  ratios are required. Plotting the ADC value in dependence of the RF voltage leads to a linear relation with a correlation factor of  $R^2=0.99$  (cf. Figure 26). By linear regression, ADC ratio and ADC offset are determined to -1.21 counts/Volt and 983.8 counts, respectively.

Table 9: Input data for mass calibration.

$m/z$ [Da]	ADC value	$V_{\text{RF}}$ [V]	$m/z$ [Da]	ADC value	$V_{\text{RF}}$ [V]
91	561	349.3	28	798	151.2
92	561	349.2	19	819	134.9
91	572	340.3	19	819	134.2
92	572	340.2	18	819	134.2
91	550	358.2	19	836	122.1
92	550	358.2	19	846	113.0
29	801	163.0	18	846	114.2
28	801	163.9	19	858	103.9
28	798	151.5	18	858	103.6

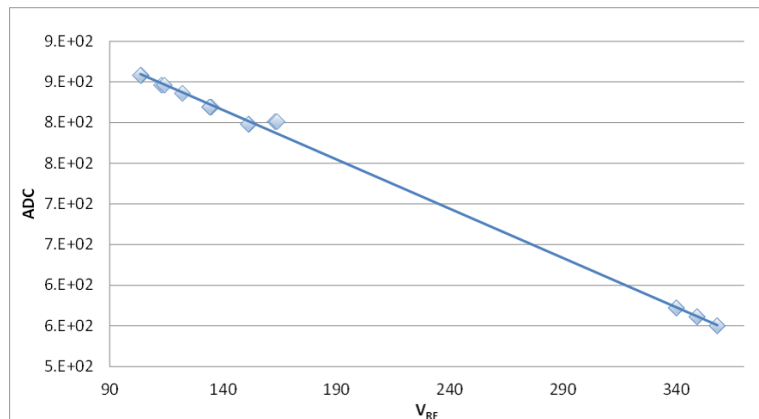


Figure 26: Linear regression line for calibration of ADC ratio and ADC offset yielding the mass calibration input data.

This mass calibration was deliberately performed for a combination of residual gas and sample gas mode measurements. Previous mass calibrations were carried out in only one of the two operational modes and showed distinct deviations. On the one hand these deviations are caused by the much smaller input mass range for each individual calibration. On the other hand the gas load itself does definitely change the calibration factor. The difficulties arising from the use of the gas inlet will be discussed later in detail. At this point just the enhanced neutral particle density, the elevated number of charged particles combined with an increased collision frequency are noted; factors surely affecting the ion oscillation within the ion trap.

*Note:* Currently, an exact mass calibration is not of primary concern. Thus, mass calibration input parameters as well as the  $m/z$  data given in the following are always referring to nominal masses. For now, those calculations are based on nominal masses as well, since the influence of a slightly varied  $m/z$  ratio on the determination of e.g. mass accuracy and mass resolution has not much impact.

## 4.2. Variation of basic measurement parameters

### 4.2.1. EI ion source

#### *Setup Mini-E-Gun*

The electron ionization source is based on a classical 70 eV filament device. In analogy to electron guns [149], this EI source consists of a Wehnelt electrode, a focus electrode and an anode electrode, and is mounted facing a small hole in the ring electrode. With the acceleration

voltage at potential of -70 V, the Wehnelt is adjusted to -75 V to maintain small bias. The focus voltage needs to be adjusted to obtain a maximum electron yield for ionization within the trap. The anode is used as electron gate “closed” at -105 V and “opened” at 0 V (Ground-potential).

### *Influence of focus voltage*

Since no emission current measurement is available in the current setup the focus voltage is adjusted with regard to the intensity of the obtained analyte signal. Figure 27 demonstrates the measurement of 500 ppbV toluene in nitrogen in pulsed sampling mode with an RF field of 340 V<sub>RF</sub> while varying the focus voltage from -70 V to +30 V. All further measurement parameters were kept constant. To ensure electron delivery into the ion trap the focus voltage must be more positive compared to the filament voltage. Otherwise no corresponding analyte ion signal is observable. In the range of approx. -68 V to -35 V no dependency of the ion signal intensity on the applied focus voltage is observed. In the following the resulting analyte signal decreases significantly remaining on a four-fold smaller value up-to focus voltages around +30 V.

For a better understanding of the focus voltage dependency a simulation is performed. This simulation is done for an RF amplitude of 150 V<sub>RF</sub> taking into account the impact of the oscillating RF field. In a color map the ion signal intensity in dependence of the focus voltage as well as the ring voltage is shown (cf. Figure 28). It is readily understandable that within the negative half-wave of the trapping field no electrons enter the ion trap. At ring electrode voltages above -70 V the simulation shows resulting ion signal intensities that are almost independent on the applied focus voltage (roughly a factor of two when electrons are electrically allowed to enter the trap).

For the experimental investigations on the focus voltage dependency an ionization length of 7 ms is applied. With the RF operated at a frequency of 1 MHz the RF amplitude oscillates 7,000 times during ionization, i.e., the experimental results correspond to a mean trapping field voltage. A direct comparison of simulation data and experimental data is thus not possible. Electrons enter the trap only when the ring voltage is at -70 V or above. In addition modulated electron energies are assumed leading to different ionization cross sections. Furthermore, the applied trapping field is distinctively higher. To a first approximation however a trapping field voltage of +50 V is assumed as mean value for RF voltages allowing

the passage of electrons. A comparison of the experimental data with simulation data at 50 V<sub>RF</sub> shows a similar behavior of the focus voltage dependency on the signal intensities.

Neither in the experiments nor in the simulations a significant influence of the focus voltage is observed. In contrast the focus voltage is adjustable over a wide range hardly leading to any signal loss or enhancement in the current setup.

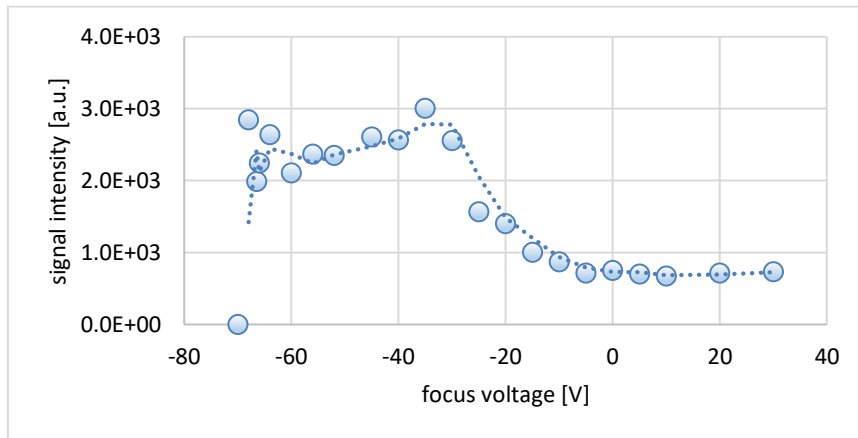


Figure 27: Dependence of the analyte signal intensities for toluene on the focus voltage.

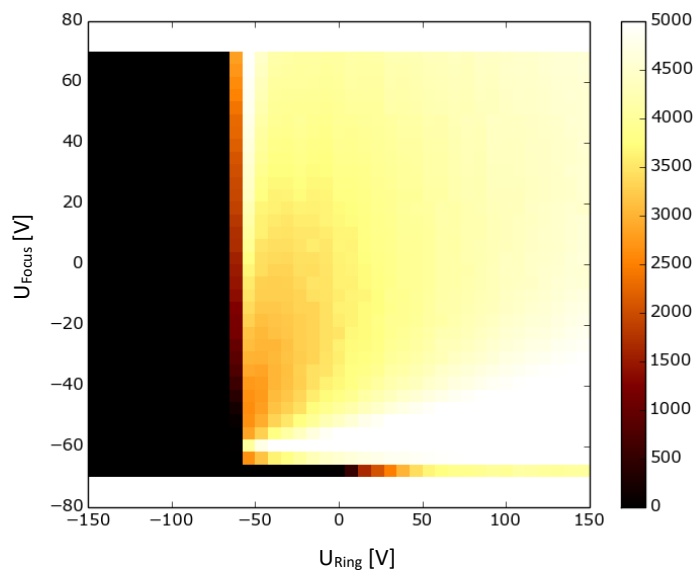


Figure 28: Color map of the simulated ion signal response depending on the focus voltage (y-axis) and the RF voltage (x-axis) for a single oscillation of the trapping field [151].

### 70 eV EI: Comparability to spectra databases

The application of 70 eV EI has one major advantage: The recorded mass spectra are comparable to those present in databases such as the *NIST Chemistry WebBook*. Nevertheless one should note that depending on the selected  $m/z$  range, trapping field voltages up-to 500 V<sub>RF</sub> are applied. Electrons which are entering the trapping field with an kinetic energy of 70 eV will be modulated in their energy by the trapping field. In the experiments the filament voltage is varied from -20 V to -100 V, with the Wehnelt voltage set to -5 V and the focus voltage to +3 V with respect to the filament voltage, while monitoring the nitrogen signal intensity. Operating within a trapping field of 116 V<sub>RF</sub> a constant ionization time (0.5 ms) is chosen for the generation of N<sub>2</sub><sup>+</sup>-ions. As shown in Figure 29 a direct correlation between the applied filament bias voltage and the ion signal intensity is observed. This correlation may also be explained by a worse electron guidance into the trap at reduced bias voltages and must not strictly be a consequence of a reduced electron energy. Corresponding simulations were carried out; the results are depicted in the picture sequence in Figure 30. Displayed is a single oscillation of the RF field with an amplitude ranging from -150 V to +150 V. The filament is biased at -70 eV and focus voltage is adjusted to 0 V. Only when the trap ring voltage is at -70 V ions begin to enter the ion trap. Subsequently the introduced electron beam splits up and a modulation of electron energies due to the oscillating field is observed. Orange trajectory sections indicate electrons exceeding 70 eV, light blue trajectory sections indicate electrons with 30 to 70 eV and dark blue trajectory sections electrons with less than 30 eV kinetic energy.

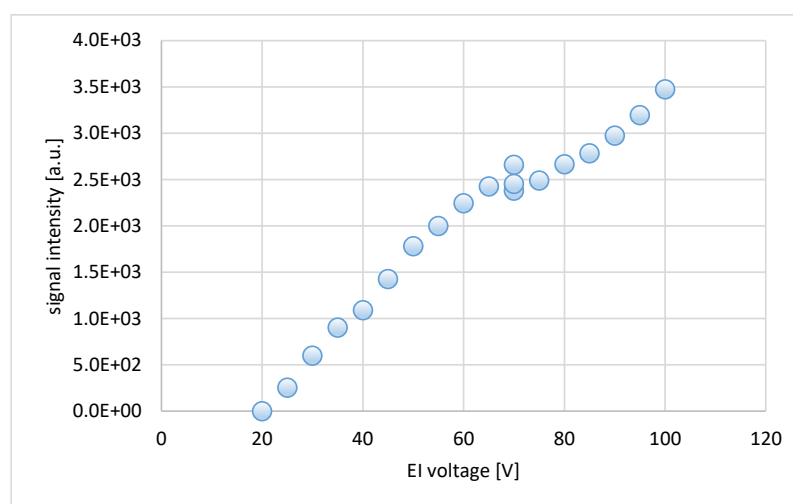


Figure 29: Dependence of the analyte signal intensities for toluene on the electron energy.

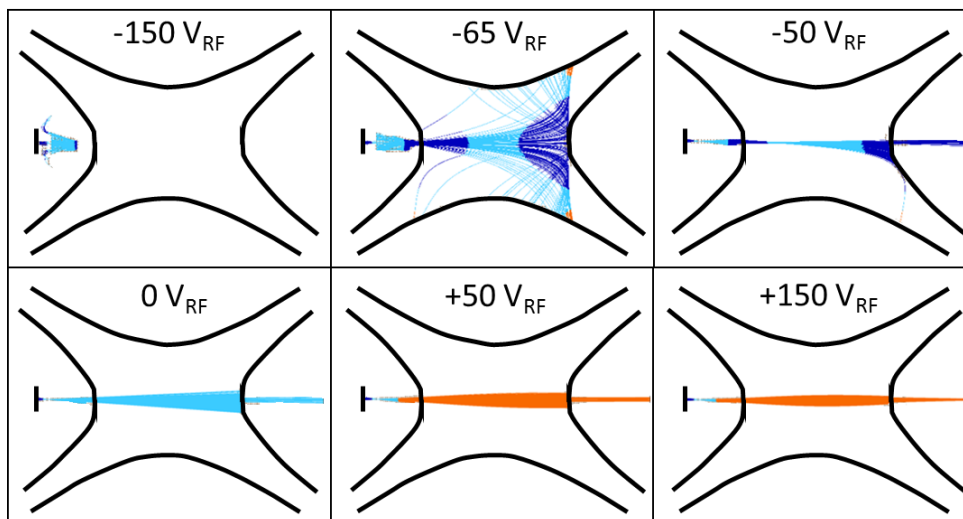


Figure 30: Selected electron trajectory simulations showing the modulation of the electron beam within a single RF oscillation. Orange color:  $E_{kin} > 70$  eV. Light blue color:  $E_{kin} 30 - 70$  eV. Dark blue color:  $E_{kin} < 30$  eV.

#### 4.2.2. Trapping field

Depending on the selected mass range the trapping field amplitude needs to be adjusted while the RF frequency is held constant at 1 MHz, as a minimum potential is required for ion storage. Showing the influence of the trapping field, measurements are carried out in residual gas mode tracing  $\text{H}_2\text{O}^+$  at  $m/z$  18 while varying the amplitude of the trapping field in the range of 80 to 150  $V_{\text{RF}}$ . Ionization length and time of ion excitation are held constant. With an RF voltage of 80  $V_{\text{RF}}$  no corresponding ion signal is observed in the mass spectrum. An increase of the trapping field amplitude leads to detectable  $\text{H}_2\text{O}^+$  signals with an intensity plateau over a wide range of the RF voltage (100 – 120  $V_{\text{RF}}$ ). A further increase of the trapping field amplitude, however, leads to the entire loss of the signal. This phenomenon is speculated to result from dips in the stability diagram caused by the non-ideal quadrupole field due to, e.g., holes in the electrodes [155–158]. Since the dip in the trapping efficiency is quite small, a small variation of the trapping field amplitude (approx. 1 %) allows the measurement of  $\text{H}_2\text{O}^+$  with reasonable signal intensities.



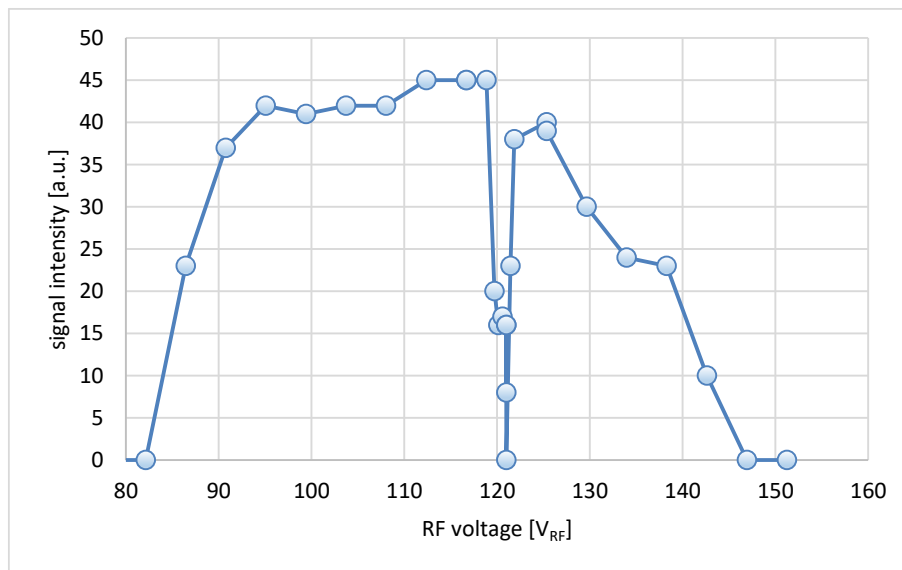


Figure 31: Influence of the trapping field voltage on the signal abundance of  $m/z$  18 in a residual gas measurement. The loss in the ion signal is addressed to dips in the stability diagram.

A further measurement that demonstrates the importance of the careful consideration of the trapping efficiency is carried out with a nitrogen/oxygen mixture (50:50) sampled out of 2.5 mbar upstream pressure with a 20 ms gas inlet time. The ionization time was adjusted to 1 ms with a 2.5  $\mu$ s excitation pulse after a short delay time of 10 ms. In this measurement the trapping field amplitude is varied from 125 to 210  $V_{RF}$ . Dips in the trapping efficiency are not observed, neither for nitrogen nor for oxygen in this measurement. Both ion species show a non-linear trend when plotting the ion signal intensity in dependence of the trapping field amplitude (cf. Figure 32 left). The intensity maximum of  $m/z$  32 is shifted to higher RF voltages compared to the signal intensity maximum of  $m/z$  28. In addition the calculated ratio of  $O_2^+/(N_2^++O_2^+)$  is plotted on the secondary axis. Instead of the expected 50 %, a ratio varying from 8 % to 68 % is determined. For a direct signal intensity comparison the mass dependent trapping efficiency, the ion frequency dependent excitation rate, and the characteristic curve of the charge state amplifier need to be considered. Correspondingly treated data show a constant signal response over a wider range of the trapping field amplitude for both ion species (cf. Figure 32 right). Between 145 and 175 Vpp constant signal response is given for both ion species, allowing the analysis of the constant  $O_2^+/(N_2^++O_2^+)$  ratio of 30 % with a significant but systematic suppression of the oxygen signal. Reasons for this suppression are currently not known.

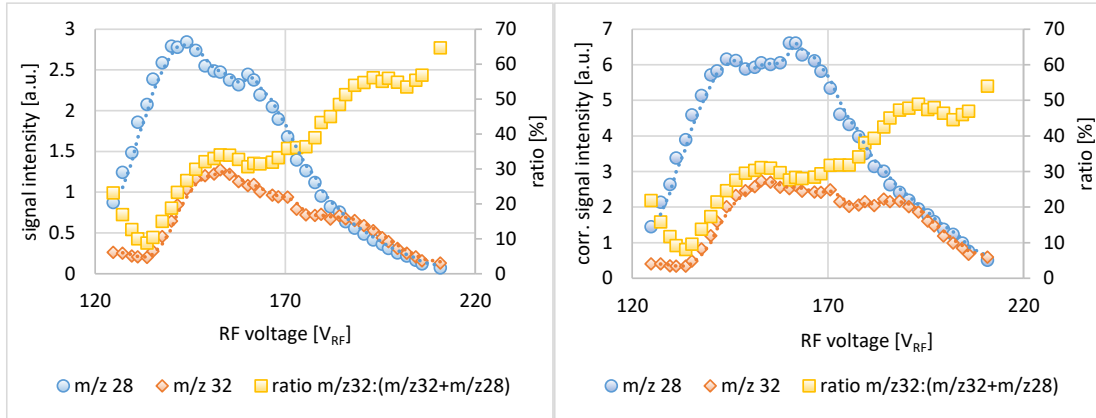


Figure 32: Signal intensity of  $N_2^+$  ( $m/z$  28) and  $O_2^+$  ( $m/z$  32) in dependence of the RF amplitude. Left: Uncorrected data. Right: Corrected data with respect to excitation rate and linearity of the charge state amplifier. Ratio of  $O_2^+/(N_2^++O_2^+)$  is plotted on the secondary axis.

As discussed, the Dehmelt potential describes the pseudopotential inside the ion trap that affects the stored ions. For the trapping of heavier ions higher RF voltages are required. Correlation of Dehmelt potential, trapping field voltage and ion mass is given by equation (4.35). The data presented in Figure 33 are obtained when plotting the signal intensities in dependence of the Dehmelt potential. For both ion species the initial slope is at same Dehmelt values representing the minimum trapping potential that is required for sufficient ion storage inside the ion trap. Once the potential barrier is high enough to keep ions inside the trap (here:  $D \approx 4.2$  V) a constant ion signal response is expected when enhancing the trapping field voltage and thus the Dehmelt voltage. Thus, a comparison of the Dehmelt potentials for signal intensities for each  $m/z$  ratio must provide optimum ion storage conditions.

$$D = -\frac{ezV^2}{4\omega^2r_0^2m_HM} \quad (4.35)$$

Herein  $D$  is the Dehmelt potential,  $e$  is the elementary charge,  $z$  is the number of charges,  $V$  is the trapping field amplitude (zero – peak),  $\omega$  is the trapping field frequency,  $r$  represents the ion trap radius,  $m_H$  is given as the mass of a H-atom and  $M$  is the molecular mass.

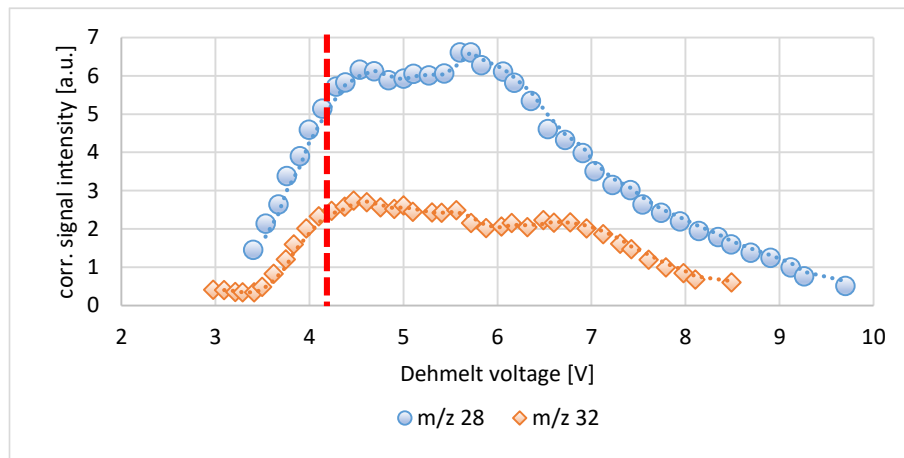


Figure 33: Corrected signal intensities of  $m/z$  28 and  $m/z$  32 in dependence of the Dehmelt voltage.

#### 4.2.3. Rectangular ion excitation

For the excitation of stored ions a rectangular DC pulse is applied to the endcap electrodes. The height of the DC pulse is held constant at 12 V whereas the pulse width is adjusted depending on the applied trapping field amplitude. Ideally it is assumed that ions are confined in the center of the ion trap so that the total energy of the excitation causes a maximum displacement of the ions without losing them due to collisions with the electrodes. The influence of the pulse width of the excitation pulse on the ion signal intensities is investigated for a 60:40 (V:V) mixture of nitrogen and oxygen. The corresponding ions are trapped within a field of  $153 V_{\text{RF}}$ . The length of the ionization pulse is 1 ms. Figure 34 shows the corresponding trends for  $m/z$  28 ( $\text{N}_2^+$ ) and  $m/z$  32 ( $\text{O}_2^+$ ) while varying the excitation pulse width from 0.5 to 4.6  $\mu\text{s}$ . The maximum signal intensity for both ion species is obtained with an excitation pulse width around 2  $\mu\text{s}$  reaching a plateau up-to pulse widths of approx. 3.8  $\mu\text{s}$ . The calculated ratio of  $\text{O}_2^+/(\text{N}_2^++\text{O}_2^+)$ , which is plotted on the secondary axis in Figure 34 (left) exhibits the correct neutral ratio over a wide range only deviating at shorter and elevated pulse widths. Figure 34 (right) shows the normalized calculated excitation rates for both species in dependence of the pulse width demonstrating a qualitatively similar trend.

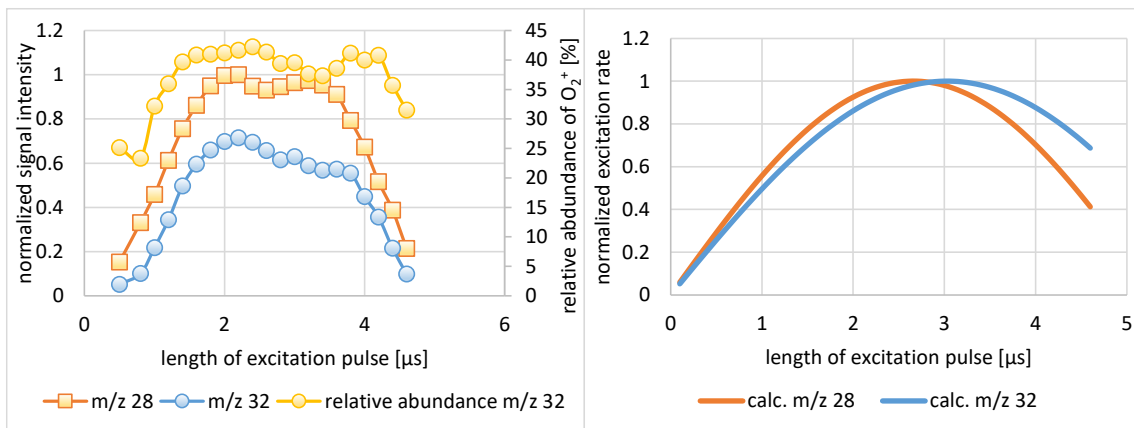


Figure 34: Left: Recorded ion signal abundances for  $m/z$  28 and  $m/z$  32 in dependence on the length of the excitation pulse, showing a constant relative abundance of  $m/z$  32 over a wide range. Right: Calculated excitation rate for  $m/z$  28 and  $m/z$  32 in dependence of the length of the excitation pulse.

The significant ion signal intensity decrease starting at excitation pulse width of  $3.8 \mu\text{s}$  is explained by overexcitation according to equation (3.30). Since the measurement was carried out in a trapping field of  $153 V_{\text{RF}}$ , one obtains:

$$12V \cdot T_p \leq \frac{1.905 \cdot 153V}{2\pi \cdot 1\text{MHz}} \quad (4.36)$$

$$12V \cdot T_p \leq 46.4 V \cdot \mu\text{s} \quad (4.37)$$

Equation (4.37) is only fulfilled up-to pulse widths of  $3.8 \mu\text{s}$ ; further increase leads to signal loss as a consequence of ion overexcitation.

### 4.3. Physical-chemical effects on FT-QIT performance

#### 4.3.1. Space charge and ion suppression

##### *Increase of total ion number*

The total number of ions depends on several parameters. The collision cross section of electrons with most gaseous compounds is peaking around 70 eV. In addition the number of generated ions is increasing with increasing length of the ionization pulse, which means an increased anode opening time, or by an increased filament current.

Figure 35 shows the measurement using a mixture of 500 ppbV toluene in nitrogen upon varying the length of the ionization pulse from 1 to 32 ms. In addition to the  $[M-H]^+$ -ion of toluene at  $m/z$  91, matrix ions such as  $N_2^+$  ( $m/z$  28) and  $N^+$  ( $m/z$  14) are expected. With the applied RF field of  $350 V_{RF}$  the LMCO is calculated to 31 Da according to equation (4.31). Thus,  $m/z$  14 and  $m/z$  28 are not trapped within the applied field. In addition resonance frequencies of matrix ions are beyond the linear range of the charge state amplifier and thus these ions cannot be detected at all. As expected the signal intensity of  $m/z$  91 initially rises with increasing length of the ionization pulse, reaching maximum signal intensity at 15 ms. Subsequently signal intensity decreases despite the further increasing ionization pulse length. This phenomenon is attributed to an overload of the trap. It is noted that even though matrix ions are not detectable and their mass is below the LMCO these ions will be initially present in the trap at least for a few oscillations of the RF field, greatly increasing the total number of ions.

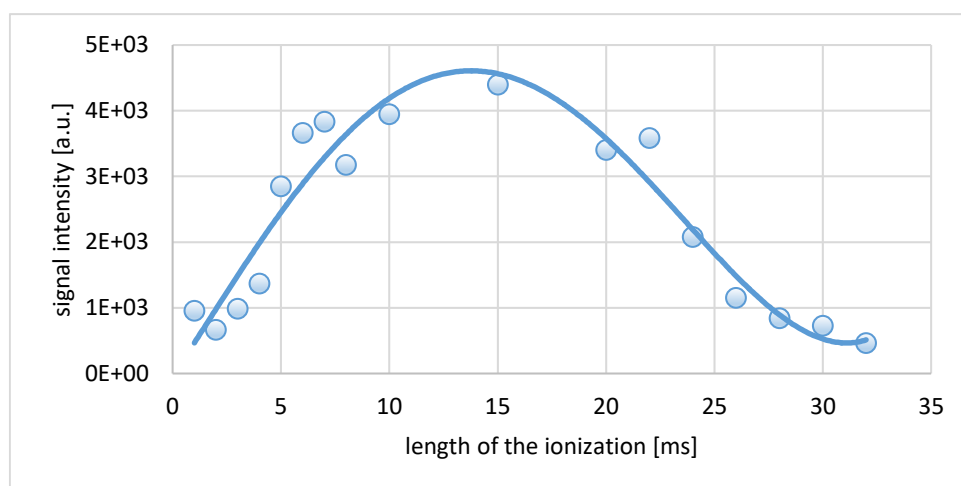


Figure 35: Measured ion signal intensity for toluene in dependence on the length of the EI ionization pulse.

An increased filament current results in a non-linear response of the electron emission current. Figure 36 shows the ion signal intensity for a mixture of 500 ppbV toluene in nitrogen in dependence of the filament current. Again, in addition to toluene ion species a number of further ions will be present within the ion trap. The signal intensity of the toluene  $[M-H]^+$  increases exponentially as expected, until the QIT is severely overloaded.

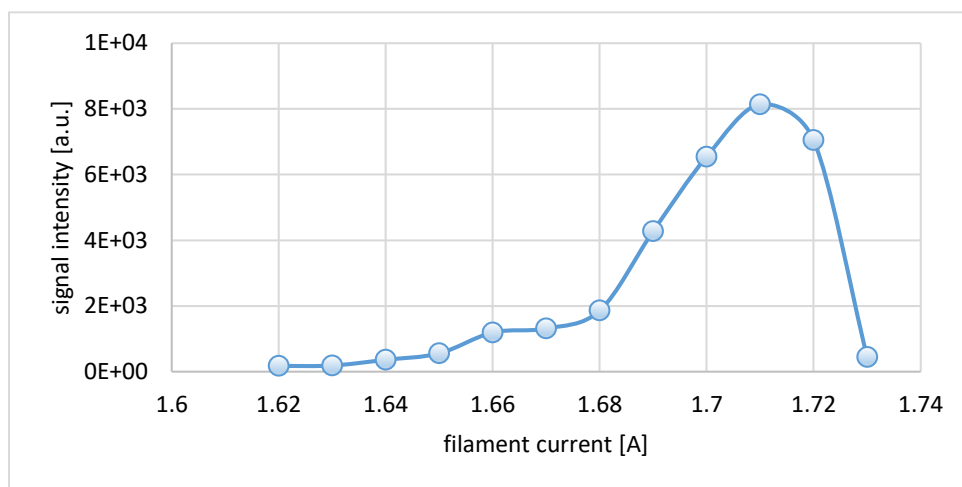


Figure 36: Ion signal intensity for toluene in dependence on the filament current.

A further experiment that demonstrates the effect of ion signal loss/suppression is carried out with a gas mixture containing nitrogen and oxygen with an oxygen mole fraction of  $X(O_2)=0.8$ . The gas mixture is sampled from a reservoir held at 5 mbar with a gas inlet pulse length of 20 ms. The amplitude of the trapping field is adjusted to 170 V<sub>RF</sub>, for ion excitation a pulse length of 2  $\mu$ s is applied and the length of the ionization pulse was adjusted to 5 ms. Under these conditions the signal distribution in the mass spectrum is correctly representing the neutral analyte distribution (cf. Figure 37 a). The total number of generated ions inside the trap is strongly increasing by an extension of the ionization time to 35 ms. The recorded mass spectrum does not correspond to the correct neutral nitrogen/oxygen mixing ratio anymore, but is showing an almost entirely suppressed nitrogen ion signal and a very large oxygen signal (cf. Figure 37 b). This experiment has also been carried out with a mixture of nitrogen and oxygen with  $X(O_2)=0.2$ . Again the signal intensities at  $m/z$  28 and 32 correctly represent the neutral analyte distribution in the gas sample when using an appropriate length of the ionization pulse of 5 ms (cf. Figure 37 c). An extension of the ionization time to 40 ms leads to a very strong nitrogen signal while the oxygen signal is almost entirely suppressed (cf. Figure 37 d).

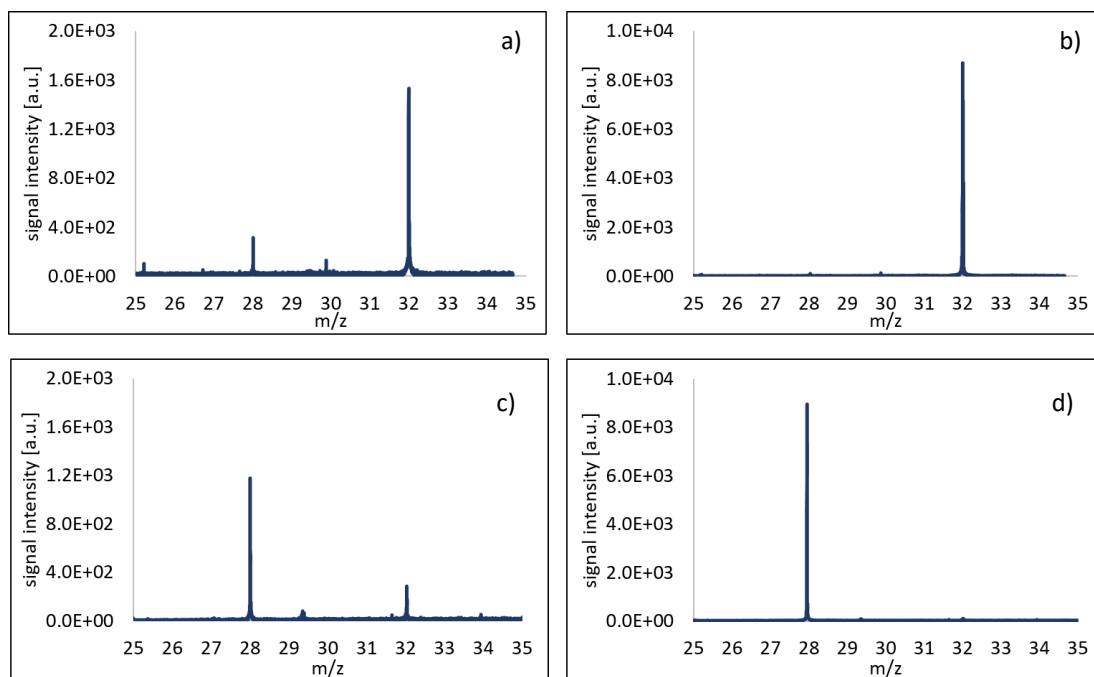


Figure 37: Signal intensity of nitrogen and oxygen with  $X(\text{O}_2)=0.8$  and an ionization of a) 5 ms and b) 35 ms. Signal intensity of nitrogen and oxygen with  $X(\text{O}_2)=0.2$  and an ionization of c) 5 ms and d) 40 ms.

The nitrogen/oxygen gas mixture with  $X(\text{O}_2)=0.2$  is also used while scanning the ionization time in the range of 5 ms to 35 ms. Both extreme cases have already been discussed in reference to Figure 37 c) showing the correct analyte distribution and d) depicting the oxygen signal suppression. Figure 38 shows the ion signal intensities for  $m/z$  28 and 32 in dependence of the ionization pulse length. For better comparison the oxygen signal is scaled with a factor of 5. Initially, both ion signal intensities increase with increasing ionization time, although the slope of nitrogen signal is significantly larger. Whereas the ion signal for nitrogen further increases, the oxygen signal collapses at an ionization time of 20 ms and is almost entirely suppressed at 35 ms ionization time. The determination of the measured signal ratio (Figure 38, secondary axis) shows that the oxygen signal decreases with the first increase of the ionization time. At an ionization time of 5 ms the oxygen signal reflects the correct 20 % in the gas mixture, the oxygen signal at 35 ms ionization time is only 1 %.

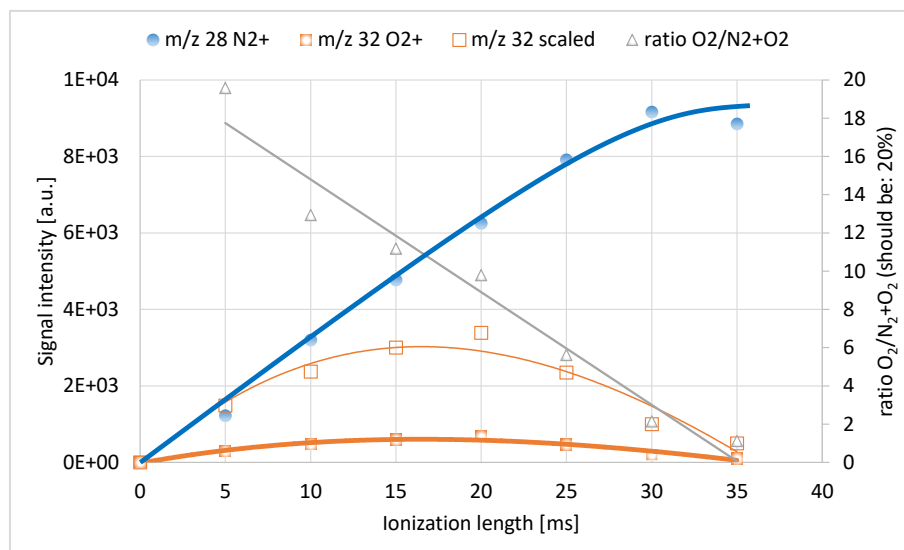


Figure 38: Signal intensities for  $m/z$  28 and  $m/z$  32 in dependence of the length of the ionization pulse.

It becomes apparent that in each of the experiments the ion signal that is present in smaller amounts suffers ion suppression at elevated total ion densities. In the first case toluene was studied as single ionic species within the mass spectrum. Nevertheless matrix ions ( $N_2^+$ ,  $N^+$ , ...) are generated in greater amounts leading to an increased total ion density and thereby causing ion suppression of toluene ions. In both other cases nitrogen and oxygen were chosen to allow an observation of both ion species within the mass spectrum. It plays a predominant role, which of the ion species is present at higher amounts. Thus, ion signal suppression is most probably an effect caused by space charge effects inside the ion trap rather than e.g. charge transfer processes.

#### *Mass signal shifts due to a prolonged ionization time*

With increasing number of the total ion density within the ion trap, also mass signal shifts gain in importance. The measurement of a mixture of 500 ppbV toluene in nitrogen in dependence of the ionization time as already discussed further above allows an examination of space charge induced mass signal shifts. At an ionization time of 0.8 ms the toluene signal is at  $m/z$  91.05 (Note: the system is not calibrated). The maximum mass signal shift is observed at an ionization time of 30 ms with a  $m/z$  ratio of 91.32 (cf. Figure 39). Hence, the total mass signal shift in this measurement scenario is determined to 0.27 Da, which corresponds to a



mass accuracy of 3 ‰ (= 3,000 ppm<sup>3</sup>) according to equation (4.38). Mass accuracy when determined in this work is always referring to an  $m/z$  error ( $Err$ ) in relation to the  $m/z$  value.

$$Err = \frac{\Delta m/z}{m/z} \quad (4.38)$$

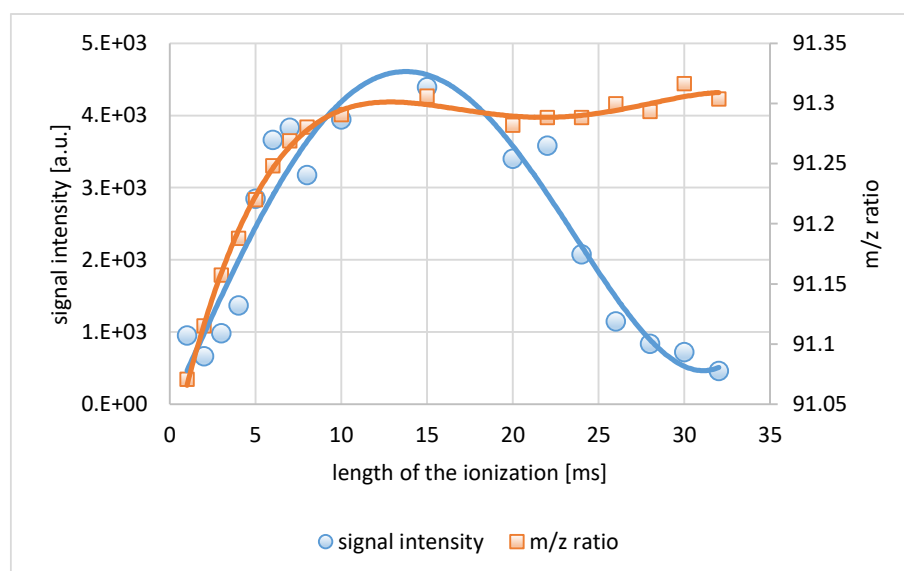


Figure 39: Signal intensity of toluene (primary axis) and  $m/z$  ratio of the ion peak (secondary axis) in dependence of the length of the ionization pulse.

### Mass signal shifts due to increased filament currents

A similar result is obtained when increasing the total number of ions by increasing the filament current. The dependence of the ion signal intensities on the applied filament current has already been presented further above. With toluene present at 500 ppbV in nitrogen the mass signal shift of the  $[M-H]^+$  is recorded while varying the filament current in the range of 1.62 A - 1.72 A. Whereas the  $m/z$  ratio is determined to 91.16 Da at 1.62 A filament current, a strongly shifted  $m/z$  ratio of 92.84 Da is determined at 1.7 A. Due to the significantly increased number of ions within the ion trap an absolute mass shift of 1.68 Da is observed, corresponding to a deviation of approximately 1.8 ‰. Although the measurement of the toluene signal intensities showed reasonable abundances at comparably small filament

<sup>3</sup> Since mass accuracy values are ideally far below the ‰-range, they are typically given in ppm.

currents, the analysis of mass signal shifts shows already 0.4 % deviation when varying the filament current between 1.63 and 1.65 A. This strongly suggest a trap overload caused by apparently subtle changes of the filament current.

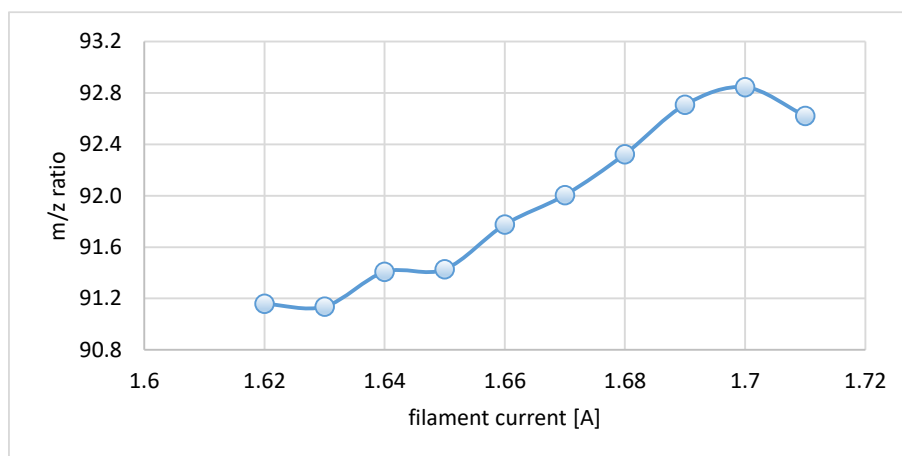


Figure 40: Mass signal shift for the toluene  $[M-H]^+$  at  $m/z$  91 while varying the filament current.

#### 4.3.2. Ion molecule reactions affecting signal ratios

Space charge induced ion signal suppression is manageable by carefully adjusting the total charge present inside the ion trap (filament current, ionization time). Nonetheless, ion-molecule reactions can significantly affect the ion signal distribution in the recorded mass spectrum, which is then incorrectly representing the neutral analyte distribution of the gaseous sample. On the other hand, this is one of the most powerful advantages of ion trapping devices for e.g. kinetic studies of ion-molecule reactions or performing  $MS^n$  experiments [9, 67, 159]. For the application as monitor for neutral gas compositions, however, the extent of such reactions needs to be reduced to a minimum.

For examinations on the extent of ion-molecule reactions within a typical measurement cycle again a mixture of nitrogen and oxygen with  $X(O_2)=0.2$  is used. The time and length of the gas inlet as well as the time and length of the ionization pulse are kept constant. The delay time of the excitation pulse, however, is varied from 100 – 1,500 ms relative to the ionization pulse. Figure 41 shows the signal intensity of  $N_2^+$  and  $O_2^+$  in dependence of the delay time between the end of ionization and ion excitation on the primary axis. The calculated ratio of

$O_2^+/(O_2^++N_2^+)$  is represented on the secondary axis, while assuming that  $N_2$  and  $O_2$  are ionized with the same efficiency (ionization cross sections for 70 eV EI are given as  $2.508 \text{ \AA}^2$  ( $N_2$ ) and  $2.441 \text{ \AA}^2$  ( $O_2$ ) [160]). Several effects are observable within this figure. At first an increase of the  $O_2^+$  signal with the delay time is clearly visible. An increasing delay time between ionization and ion excitation pulse naturally leads to a longer reaction time for the chemical system. Thus, a decline of the  $N_2^+$  signal and an increasing  $O_2^+$  signal are expected due to charge transfer from  $N_2^+$  to  $O_2$  according to reaction R.4.37.



In addition to the increase of the  $O_2^+$  signal and the corresponding declining  $N_2^+$  signal an overall decreasing total signal intensity with increasing delay time is observed, resulting in an  $O_2^+/(O_2^++N_2^+)$  ratio that levels off to constant values around 42 %. This behavior is rationalized with respect to the applied pulsed gas inlet: With an increasing delay time the pressure within the ion trap is continuously decreasing (cf. chapter 4.5). Subsequently the collision rate and therefore the reaction probability for charge transfer reactions to occur decreases. It is obvious that the transient pressure profile in combination with time for chemistry to occur is strongly affecting the extent of ion-molecule reactions.

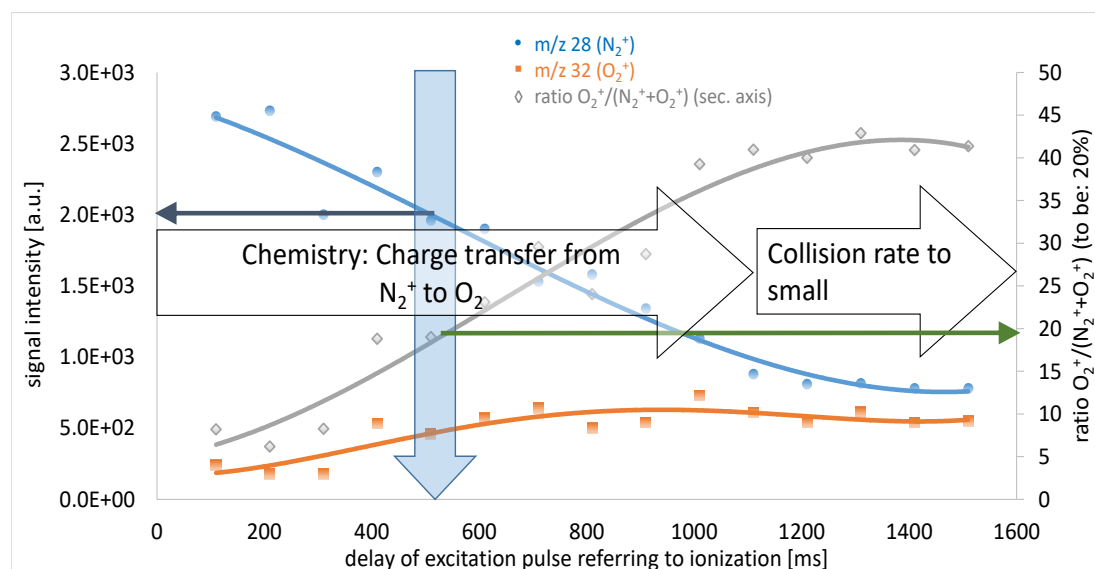


Figure 41: Signal intensity for  $m/z$  28 and  $m/z$  32 in dependence of the delay time until ion excitation.

Besides the chemical influence on the signal distribution Figure 41 shows again the importance of a non-overloaded analyzer as discussed in the previous section. At short delay times the total number of ions inside the trap is exceedingly high. Thus, the oxygen signal is suppressed by the stronger nitrogen signal. With carefully adjusted operating conditions, which control the number of generated ions inside the trap, accurate signal distributions in the mass spectra can be obtained. The total ion load of the trap should not exceed a critical value, which is  $2 \cdot 10^3$  on the arbitrary units scale of the system. Simultaneously the delay time between ionization and ion excitation and therefore the reaction time should be reduced to a minimum in order to minimize ion-molecule reactions. This operating point is highlighted in blue in Figure 41 leading to the correct representation of  $O_2^+/(O_2^++N_2^+)$  ratio (green arrow).

#### 4.3.3. Operation in pulsed gas mode, filament behavior

The experiments presented further above focus on the extent of charge overload as a function of ionization time and filament current (space charge effects) and the extent of ion-molecule reactions as a function of transient pressure and detection pulse delay. Results obtained from these measurements are used to establish a parameter set for neutral gas composition monitoring. Measurements are again carried out with a mixture of nitrogen and oxygen while dynamically varying the mole fraction of  $X(O_2)$  ranging from 0 to 1. Avoiding any overload of the analyzer, the length of the ionization pulse is adjusted to 1 ms. This leads to a  $m/z$  28 signal for pure nitrogen with an intensity of 1,600 in arbitrary units as shown in Figure 42. The first addition of small amounts of oxygen (5 %) causes a significant drop in the total signal intensity by a factor of approximately 4. This effect is well known in the literature [162, 163] and is addressed to the formation of oxides on the surface of the wolfram filament leading to a loss in electron emission efficiency. Once the oxide layer has formed any further increase of the oxygen mixing ratio has no further effect on the electron emission current at constant filament current. Thus, the signal intensities for widely ranging nitrogen to oxygen ratios correctly reflect the neutral analyte distribution in the gas sample (cf. Figure 42).

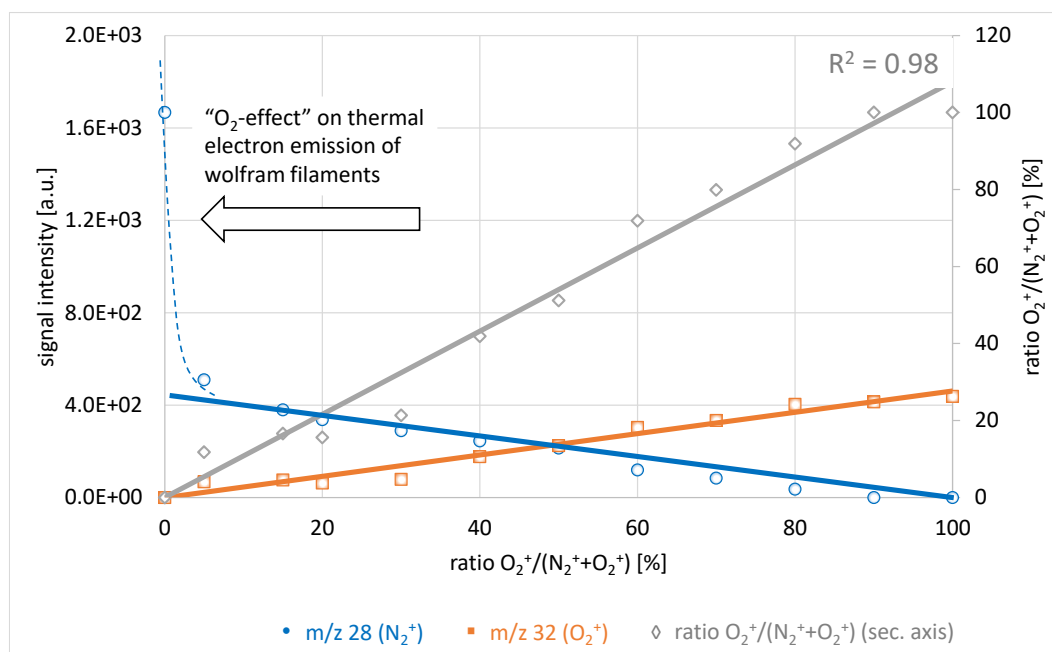


Figure 42: Signal intensity for  $m/z$  28 and  $m/z$  32 in dependence of the nitrogen/oxygen mixing ratio.

#### 4.4. Advanced excitation schemes

Undisputable, the QIT is almost always operated under non-ideal conditions. It has been shown that upon the careful adjustment of the operational parameters mass shifts and ion suppression are largely avoided. Nevertheless, further improvements become inevitable, especially when strongly increased dynamic ranges for trace analysis in the presence of gas matrix compounds in large excess are considered. An enhancement of the performance of the entire setup is possible upon application of advanced ion excitation schemes, as for example SWIFT.

##### *Avoiding ion suppression caused by longer ionization times*

In analogy to the measurement presented in section 4.3.1 a mixture of 500 ppbV toluene diluted in nitrogen is investigated while varying the length of the ionization pulse. The RF voltage is adjusted to 350 V<sub>RF</sub>. Thus, the toluene [M-H]<sup>+</sup> ion is the single detectable ion species whereas nitrogen derived ion species are certainly present in the trap. In contrast to the

measurement shown above, in this case a SWIFT pulse is applied, that excites a wide range of  $m/z$  values below and above the resonance frequency of the  $[M-H]^+$  at  $m/z$  91. With sufficiently high energies the excited ions are removed from the trap by discharging on the QIT electrodes surfaces. Keeping measurement conditions as close as possible the SWIFT pulse with a duration in the milliseconds range is started 5 ms prior to the end of the ionization.

Due to the application of the SWIFT waveform matrix ions are removed during and after ionization. Even at short ionization pulse lengths enhanced toluene signal intensities are measured. With respect to Figure 35 the signal intensity measured without the application of SWIFT decreases at ionization pulse lengths exceeding 15 ms. The maximum achievable signal intensity is about 4,500 in arbitrary units. With the applied SWIFT pulse comparable signal intensities are achieved with a much shorter ionization length of only 6 ms. Up-to a signal intensity of  $2 \cdot 10^4$  in arbitrary units the signal rises proportional to the length of the ionization pulse, which is then not longer than 18 ms. A further increase of the ionization pulse neither leads to a further linear increase of the signal intensity, nor to any signal loss. Even at an ionization pulse length of 170 ms, which is more than a factor of ten longer than compared to the experiment without the use of SWIFT, a sustained high signal intensity ( $3 \cdot 10^4$  a.u.) is measured. From the results presented above, it is concluded that the total signal intensity should not exceed a value of  $2 \cdot 10^3$  a.u., to avoid trap overload. This readily explains why the signal intensity does not rise linearly beyond values of  $10^4$  a.u.. The removal of any matrix ions present at high amounts prevents the toluene signal from being suppressed. It is noted that a strongly increased number of ions will hamper an effective application of SWIFT.

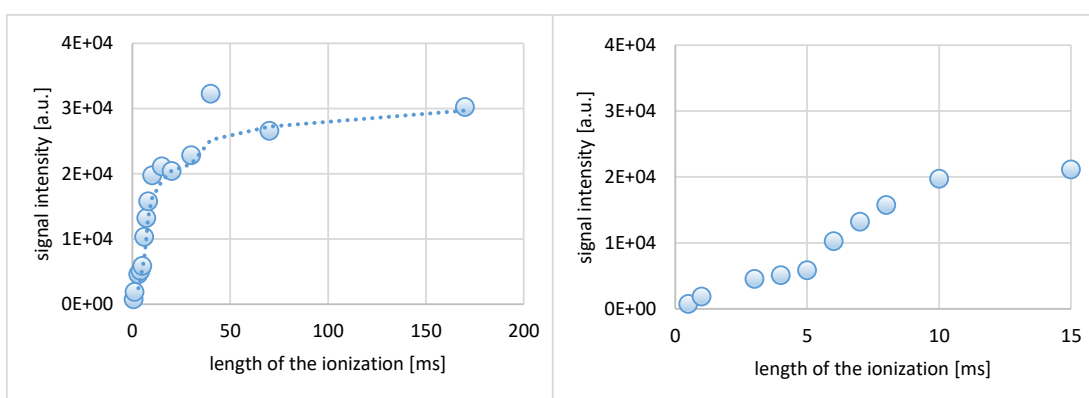


Figure 43: Left: Ion signal intensity for toluene in dependence on the length of the EI ionization pulse with application of SWIFT. Right: Zoom into the dependency at short ionization times.

### *Avoiding ion suppression caused by increased filament currents*

The strongly increased number of ions and the related mass shifts caused by elevated filament currents have also been presented above (cf. section 4.3.1). Again, the application of suitable SWIFT waveforms leads to the reduction of space charge within the trap. As the measurements are carried out within an identical trapping field, the same SWIFT pulse as previously described is used. Nevertheless, as the signal intensity rises exponentially with filament current, the toluene ion signal still collapses at filament currents around 1.7 A. However, the positive effect of SWIFT application becomes clearly visible when comparing the results without and with SWIFT in a single plot (cf. Figure 44). The ion signal breakdown is observed at comparable filament currents (approx. 1.7 A), but the toluene dependent ion signals are almost 3 times greater with the application of SWIFT under otherwise identical measurement conditions.

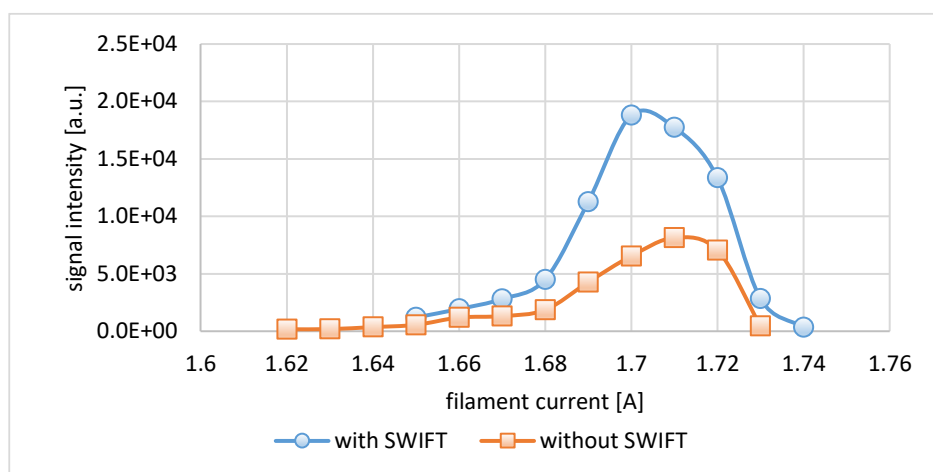


Figure 44: Signal intensity of the toluene  $[M-H]^+$  in dependence of the filament current with (orange trace) and without (blue trace) the application of SWIFT signals.

### *Analysis of trace components*

Analysis of trace components that are present at ppbV levels or lower require significantly longer ionization times for a sufficient analyte ion generation. Since 70 eV electron ionization is a non-selective ionization technique, the carrier gas and other matrix components that are present at much higher mixing ratios are ionized with nearly identical efficiency and therefore are present very large excess. As an example the measurement of

krypton diluted in nitrogen is shown. Since four stable isotopes are known for krypton, corresponding ion signals are expected at  $m/z$  82 (12 %),  $m/z$  83 (12 %),  $m/z$  84 (57 %) and  $m/z$  86 (17 %) [164].

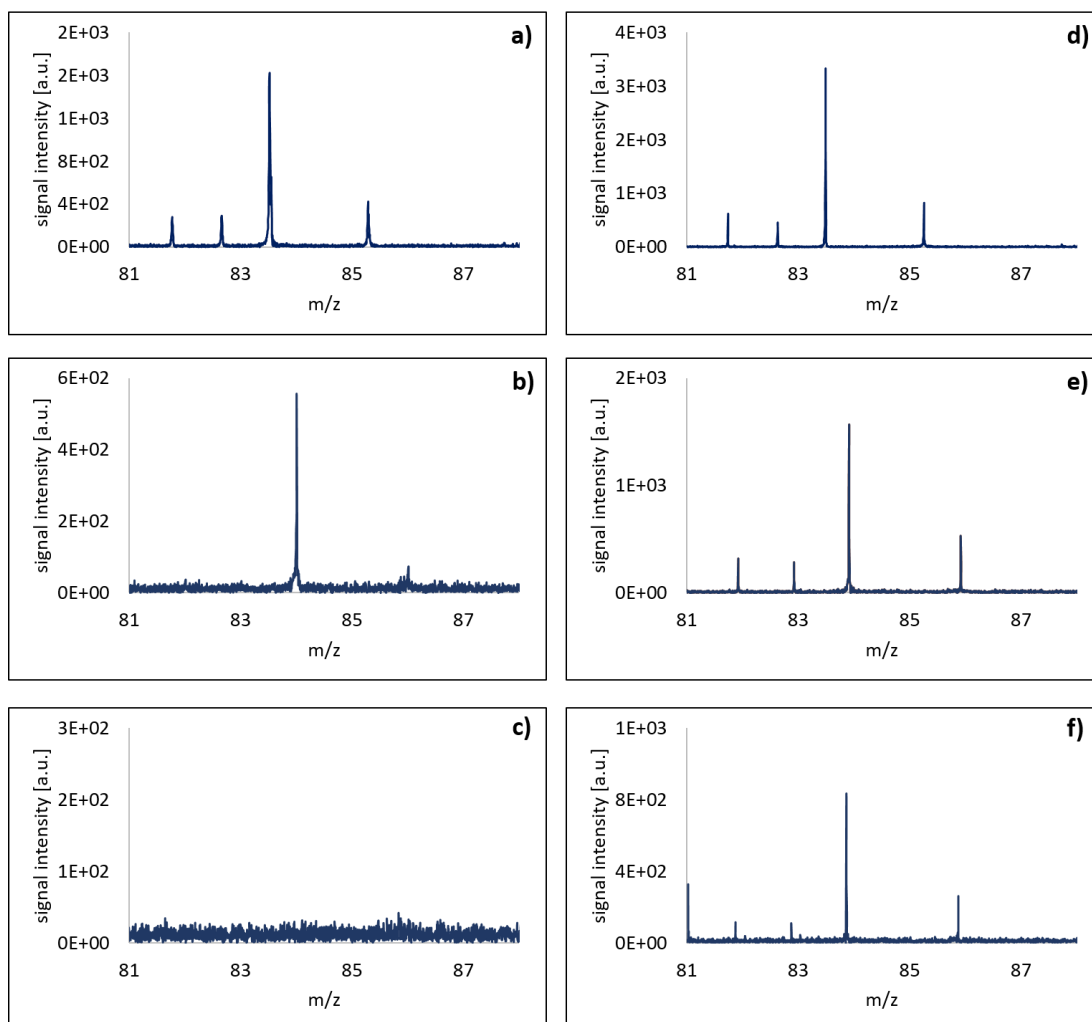


Figure 45: Signal intensities of krypton diluted in nitrogen at a) 10 ppmV, b) 1 ppmV and c) 100 ppbV without the application of SWIFT and d), e) and f) with the application of SWIFT.

With krypton present at relatively high mixing ratios of 10 ppmV the measurement of all four ion species is successful showing roughly the correct isotopic pattern [cf. Figure 45 a), ionization time 0.5 ms]. A reduction of the krypton mixing ratio to 1 ppmV necessitates an increase of the ionization time to 2 ms and is thus leading to the generation of a relative large amount of nitrogen radical cations. As described further above the presence of any ion species at elevated charge densities potentially causes suppression of ions present at lower mixing



ratios. An extension of the ionization time allows the measurement of krypton as only one collapsed single signal at  $m/z$  84 (cf. Figure 45 b). At krypton mixing ratios below 1 ppmV no corresponding ion signal is observed in the mass spectrum neither by a further extension of the ionization time to 10 ms (cf. Figure 45 c). However, the application of synthesized SWIFT waveforms for the “kick-out” of any matrix ion species (e.g.,  $\text{H}_2\text{O}^+$ ,  $\text{O}_2^+$ ,  $\text{N}_2^+$ ) allows the measurement of krypton ions even at low mixing ratios with the correct isotopic pattern. In all three cases the application of SWIFT signals improves the quality of the measurement. For 10 ppmV krypton in nitrogen an enhancement of the signal intensity by a factor of almost 2 and an enhancement of mass resolution from 2,000 to 6,000 at  $m/z$  84 is observed, as shown in Figure 45 d). The collapsed single ion signal measured for 1 ppmV krypton is split up into all expected isotopes (cf. Figure 45 e). Figure 45 f) shows the measurement of 100 ppbV krypton reflecting the correct isotopic pattern due to the application of SWIFT whereas the measurement without SWIFT did not show any signal at all.

#### *Avoiding space charge induced mass shifts*

All measurements carried out with increased total ion numbers within the ion trap show a distinct mass shift at elevated ion densities for the regarded ion species. The application of SWIFT pulses allows a reduction of the total ion number within the ion trap. Thus, space charge is strongly reduced leading to a reduction of space charge induced effects as the discussed mass shifts. The above presented experiments with extended ionization time and filament current are also examined with respect to the mass accuracy of the toluene ion signal when applying SWIFT waveforms. In addition to the greater toluene ion signal intensities as compared to measurements without the application of SWIFT signals, also the observed mass shifts are significantly smaller. Considering only ion signal intensities at appropriate levels (maximum  $5 \cdot 10^3$  a.u., cf. Figure 43, p.80) the mass shift is reduced to  $< 0.03$  Da when increasing the ionization time and  $< 0.07$  Da when increasing the filament current. Ion signal mass shifts with and without the application of SWIFT are compared in Figure 46 and Figure 47.

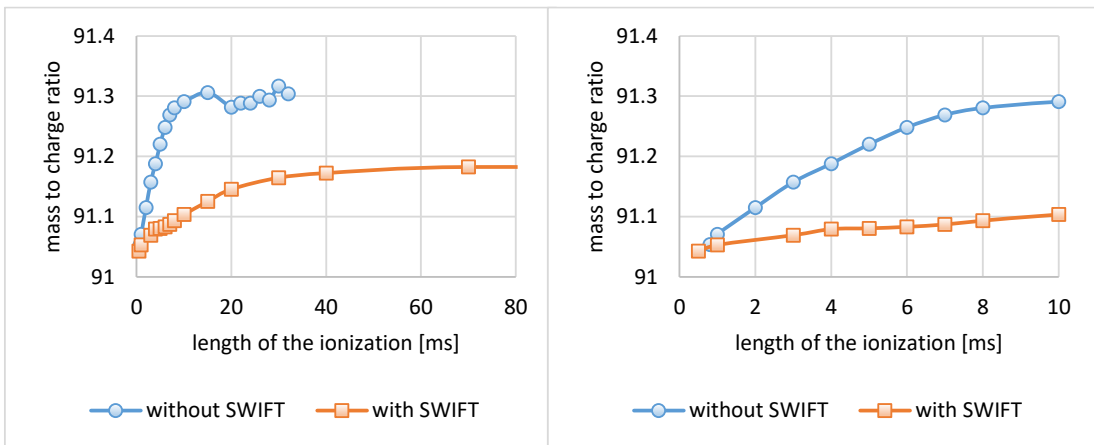


Figure 46: Observed mass shift in dependence of the length of the ionization pulse with and without the application of SWIFT.

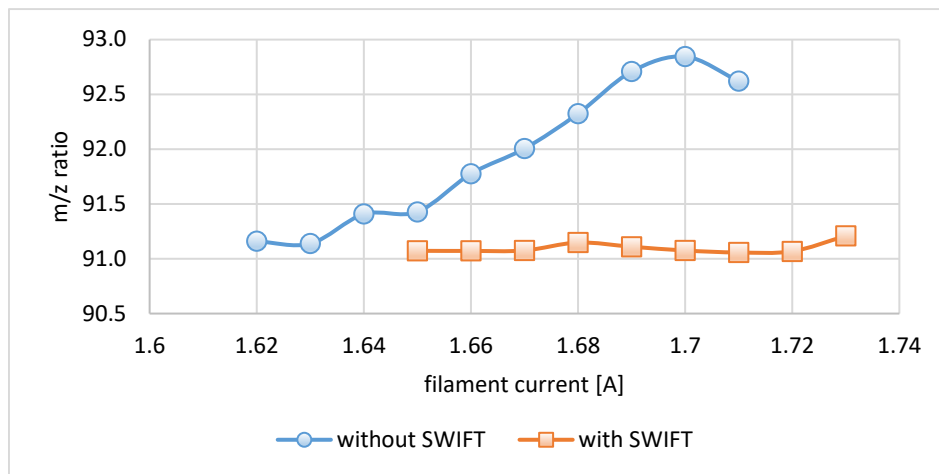


Figure 47: Observed mass shift in dependence of the filament current with and without the application of SWIFT.

## 4.5. Gas inlet: A crucial parameter

The design of the gas inlet is undoubtable one of the most crucial parameters in the operation of the FT-QIT system. It is stressed, that the entire system is designed to be as compact as possible including the valve-driven pulsed gas inlet. Gathering information on the transient pressure profile during and after gas inlet allow an estimation of the maximum pressure reached within the ion trap. Two different approaches are used:

- *Recording of the pressure gauge analog output:* With an oscilloscope the pressure gauge reading (Type: Pfeiffer PKR 261, Pfeiffer Vacuum, Asslar, Germany) of the vacuum recipient is recorded. As trigger signal the electrical activation pulse of the ALD valve is used. The recorded signal is a voltage signal that is proportional to the logarithm of the pressure. The according transformation equations are given in the pressure gauge manual.

*Note:* The response time of the pressure gauge is pressure dependent and given by the manufacturer with  $< 10$  ms at  $10^{-6}$  mbar and up-to 1 s at  $10^{-8}$  mbar [146]. Thus the recorded pressure profile will be influenced by this response time. It will be shown later that the response time only causes a small temporal shift.

- *Mass spectrometric examination:* With an analyte present at elevated mixing ratios (e.g. 1 ppmV toluene in nitrogen) the QIT itself can be used to examine the pressure profile within the ion trap. For the analysis of analytes at such high mixing ratios short ionization times of 1 ms are sufficient. Hence, the gas inlet time as well as the time for the excitation pulse are kept constant whereas the 1 ms ionization time is moved with increasing delay times within the pressure pulse. For each point of ionization time a mass spectrum is recorded allowing an evaluation of the ion signal intensity. Plotting the signal intensities in dependence of the ionization time allows a representation of the pressure profile, since under the selected QIT conditions the obtained ion signal intensity is directly proportional to the particle density.

#### 4.5.1. Design I: Bended metal tube

Most of the experiments to examine the pressure profile within the ion trap are carried out with the gas inlet design I as shown in the Experimental section (p. 48). Typical measurement parameters used as starting points are a sample pressure of 2.5 mbar and a gas inlet time of 20 ms whereas the QIT background pressure is kept  $< 10^{-8}$  mbar.

##### *“Standard” measurement settings*

The transient pressure gauge signal when introducing toluene diluted in nitrogen shows a sharply rising and then slowly depleting section (cf. Figure 48). The onset of the rising slope is determined as 24 ms after opening of the valve. The maximum pressure of  $5.5 \cdot 10^{-4}$  mbar is reached at 53 ms. As the pressure is only slowly dropping, pressures  $< 10^{-6}$  mbar that are necessary for the ion detection phase are only reached after 600 ms.

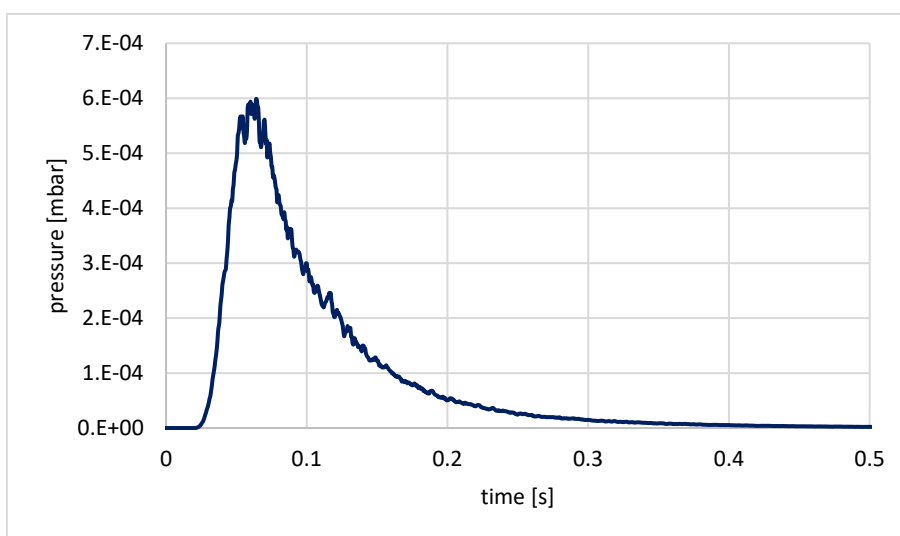


Figure 48: Pressure profile measured with the pressure gauge for a 20 ms gas inlet with 2.5 mbar upstream pressure.

With toluene diluted in nitrogen  $m/z$  91 ( $[M-H]^+$ ) and  $m/z$  92 ( $M^+$ ) signals are observed. Plotting the abundance of both ion species in dependence of the time when the ionization pulse is applied, similar curves to the pressure profile are acquired (cf. Figure 49) with a significantly greater abundance of  $m/z$  91. Allowing a better comparison the ion signal intensities and the pressure are normalized to the respective maxima, as depicted in Figure 50 (left). The

transients of both toluene dependent ion signals are in very good agreement. By a temporal shift of only 10 ms the pressure transient becomes congruent with the signal intensity transients (cf. Figure 50 right).

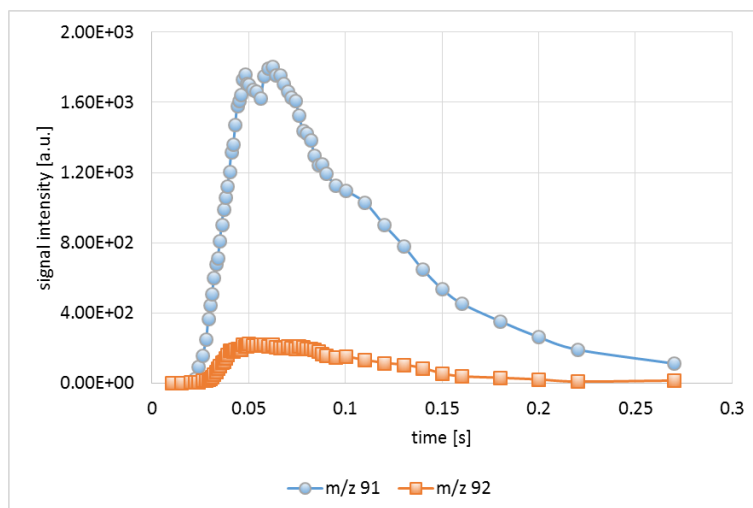


Figure 49: Ion signal intensity profile at  $m/z$  91 and  $m/z$  92 upon application of a 20 ms gas pulse from 2.5 mbar.

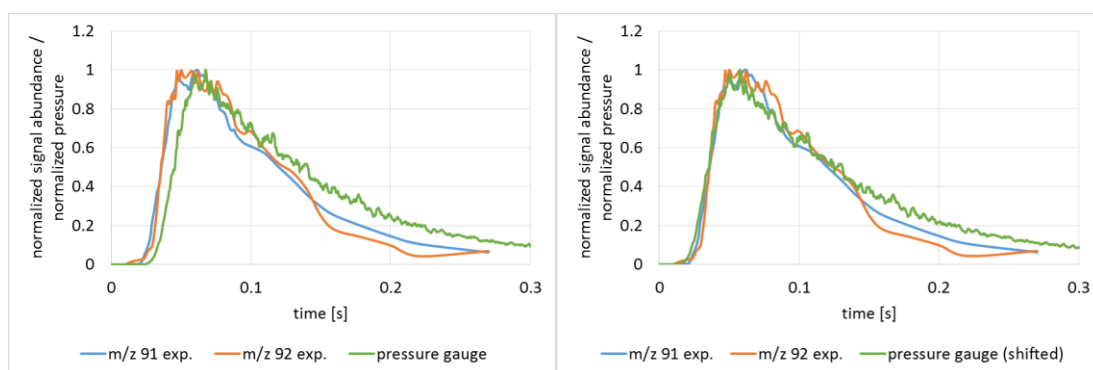


Figure 50: Left: Normalized signal abundance and pressure profile plotted on the same time scale. Right: Normalized signal abundance and a 10 ms shifted normalized pressure profile.

The reproducibility is examined with a number of different analytes. Ionization time dependent signal intensities are recorded for toluene species ( $m/z$  91,92) and benzene species ( $m/z$  77, 78) all resulting in qualitatively identical signal intensity curves.

### Variation of gas pulse length

The length of the applied gas pulse is varied to introduce corresponding amounts of analyte molecules. In addition to 20 ms typical gas inlet times are 15 and 25 ms. Recording of the pressure gauge data as well as analysis of the ionization time dependent signal intensities of toluene in nitrogen show an increase in the overall signal intensities with an increasing opening time of the valve (cf. Figure 51). However, the beginning of the initial slope as well as the position of the signal maximum are almost independent of the gas inlet time. This becomes more obvious when regarding the normalized pressure and signal intensity curves (cf. Figure 52). The only notable difference is a small deviation in the value of the initial slopes. As these different slopes are not observed in the non-normalized plots, it is concluded that the first pressure increase is not depending on the length of the gas inlet but only representing the first gas molecules entering after opening the valve. The pump-down time until optimum pressure conditions for QIT analysis are reached is for all three gas inlet times approx. 600 ms. Comparison of the pressure data and the signal intensity curves shows very good agreement when shifting the pressure curves -10 ms (cf. Figure 53, experimental data on primary axis and pressure gauge data on secondary axis).

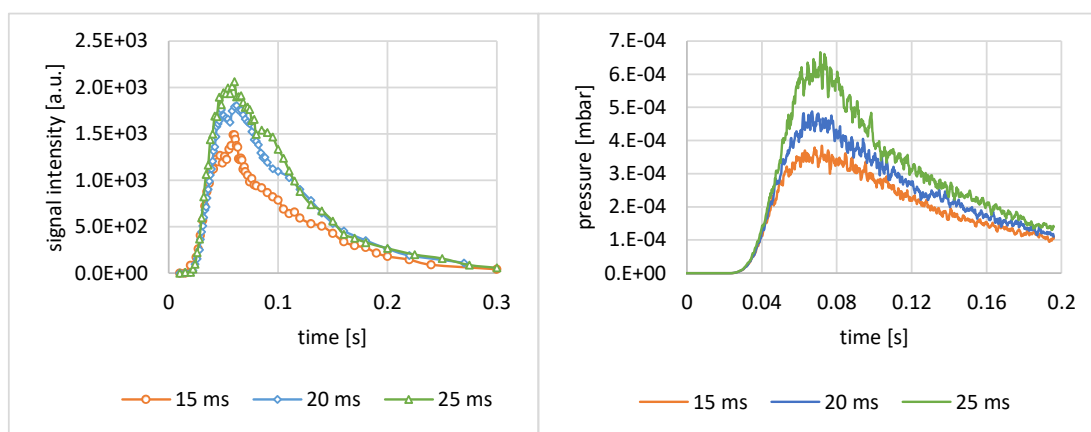


Figure 51: Analyte ion signal response (left) and pressure data response (right) in dependence of the length of the gas inlet pulse.

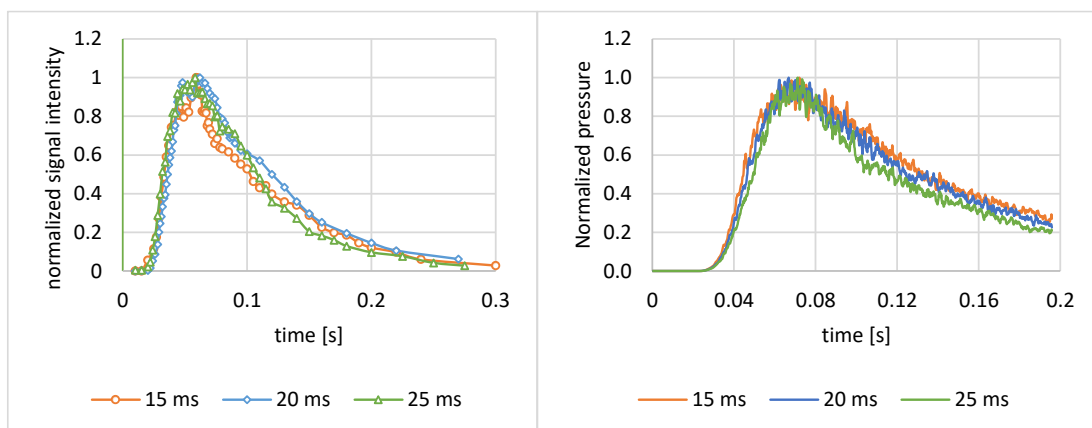


Figure 52: Normalized analyte ion signal response (left) and normalized pressure data response (right) in dependence of the length of the gas inlet pulse.

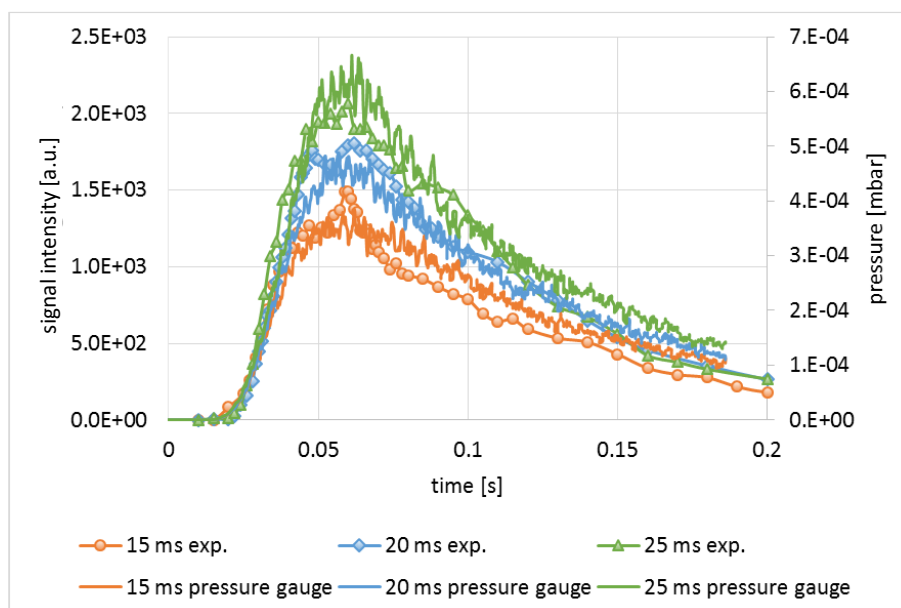


Figure 53: Comparison of the ion signal intensity and shifted pressure data for the three gas inlet pulse lengths.

### Variation of sample pressure

Upon increasing the sample pressure the gas load is increasing as well. The influence of the sample pressure on the pressure profile within the ion trap is examined using the pressure gauge data in comparison to analyte ion signals<sup>4</sup>. An increasing sample pressure does not only lead to a greater number of particles but also shows a shift of the beginning of the initial slope as well as a shift of the pressure maximum to shorter times (cf. Figure 54). Although the gas load at higher upstream pressures is higher, optimum pressure conditions are reached on the same time scale as in the other experiments. This indicates that the pump-down rate of the used turbo pump is not the limiting factor but rather the gas dynamics which is driven by effusion due to the prevailing molecular flow conditions. Normalization of the pressure curves and analyte intensity signals demonstrate the very good agreement of the two independent analysis methods when applying a 10 ms shift between both data sets (cf. Figure 55).

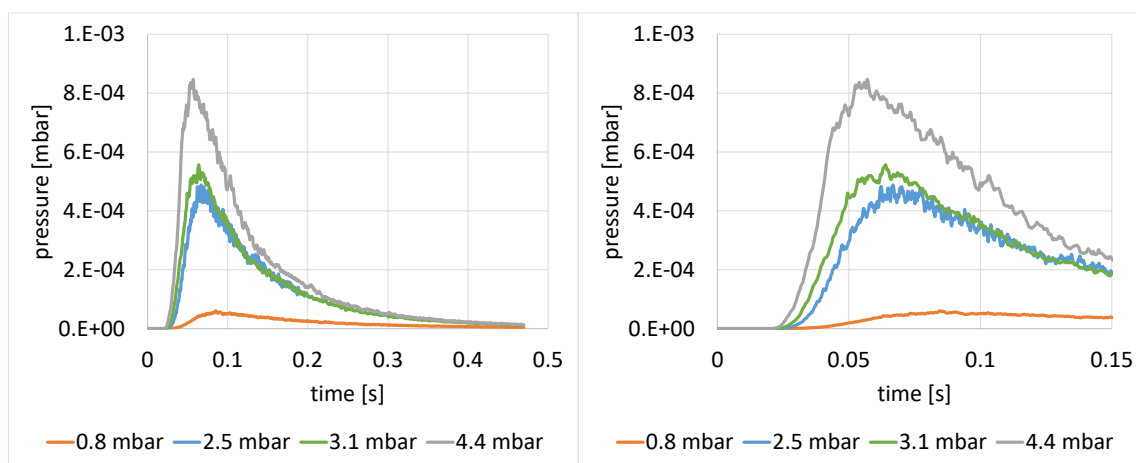


Figure 54: Transient pressure gauge data for different sample pressures. Right: Expanded region covering 0 to 0.15 s.

<sup>4</sup> Avoiding a QIT overload the ionization time at elevated sample pressures is reduced to 0.5 ms. Thus, absolute intensity values are not comparable within this set of results and therefore only the normalized data are shown.



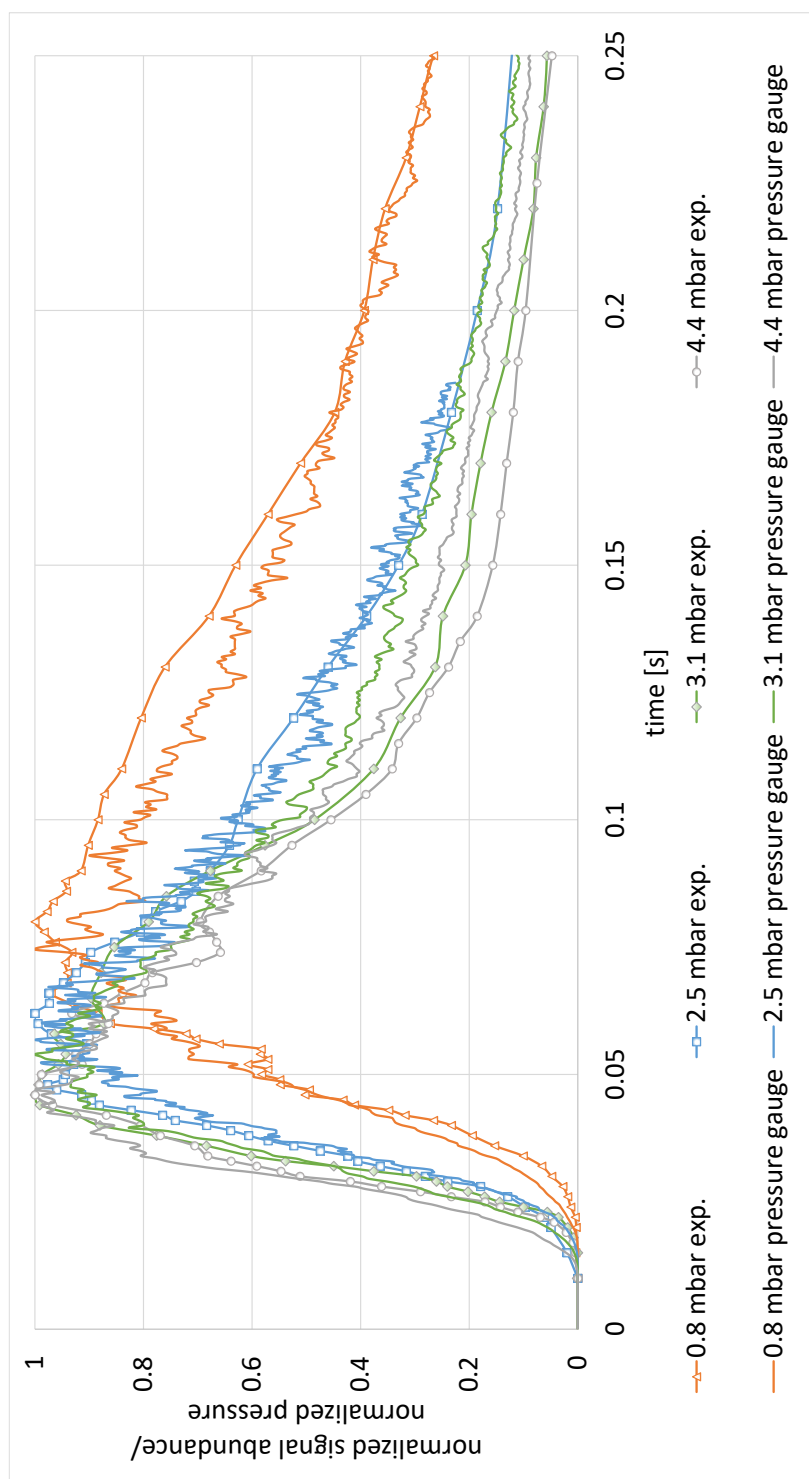


Figure 55: Transient normalized signal abundance and normalized shifted pressure data for different sample pressures.

### *Variation of gas composition*

Measurements carried out in H<sub>2</sub> as matrix gas demonstrate a pronounced influence of the gas composition on the flow behavior and thus the pressure profile inside the trap. Figure 56 compares pressure gauge data for gas samples with nitrogen and hydrogen as matrix gas, respectively. For all three applied gas inlet times the hydrogen matrix leads to an earlier initial slope of the pressure transient. The initial slopes for each matrix gas, however, are independent on the valve opening time, as presented further above. The earlier increasing pressure in H<sub>2</sub>-matrix is explained by the lower mass of hydrogen and the resulting higher velocity at identical thermal energies. Since the adjusted sample pressures are not completely identical, absolute pressures given in Figure 56 are not comparable. As the analyte molecules are carried in by the matrix gas even the measurement of toluene signal intensities shows the temporal shift between experiments in different matrix gases.

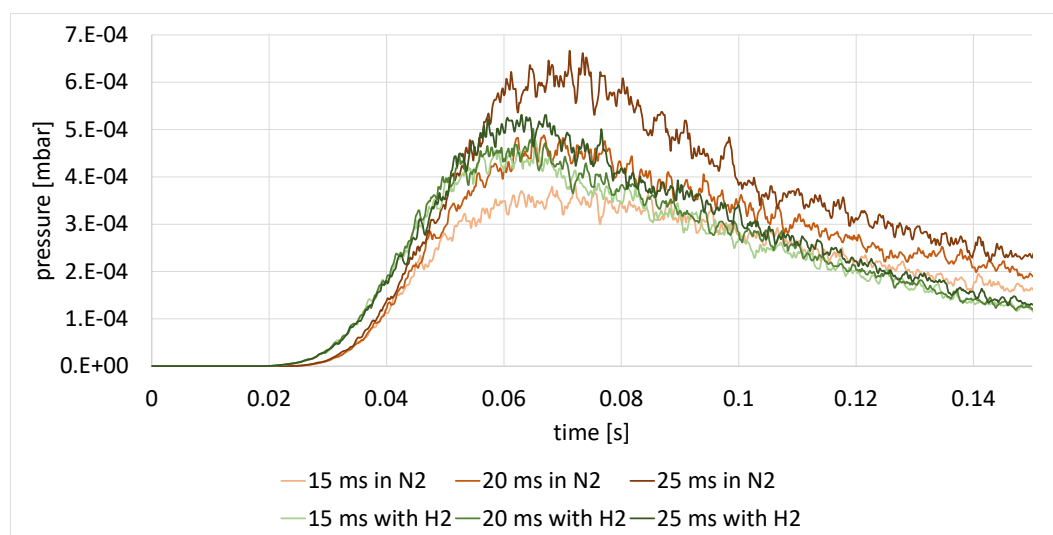


Figure 56: Transient pressure gauge data recorded for different gas inlet lengths in nitrogen and hydrogen matrix, respectively.

### Removal of the bended metal tube

The initial slope of the gas inlet used in design I is rather steep. Nevertheless the pump-down time until optimum pressure conditions for ion detection are reached (approx. 600 ms), needs to be reduced to improve the maximum repetition rate. Removal of the metal tube (gas inlet through QIT basis flange, cf. Figure 19, p. 48) leads to a significantly steeper pressure profile (cf. Figure 57). In this configuration the neutral molecules enter the QIT solely by effusion, thus only a small number of neutral molecules is present inside the trap and only reduced amounts of analyte ions are generated. Hence this gas inlet is more suitable with respect to faster pump-down rates but will not facilitate sensitive measurements. It is concluded though that the slow pump-down rate using design I is a consequence of the bended shape of the tubing in combination with the molecular gas flow dynamics.

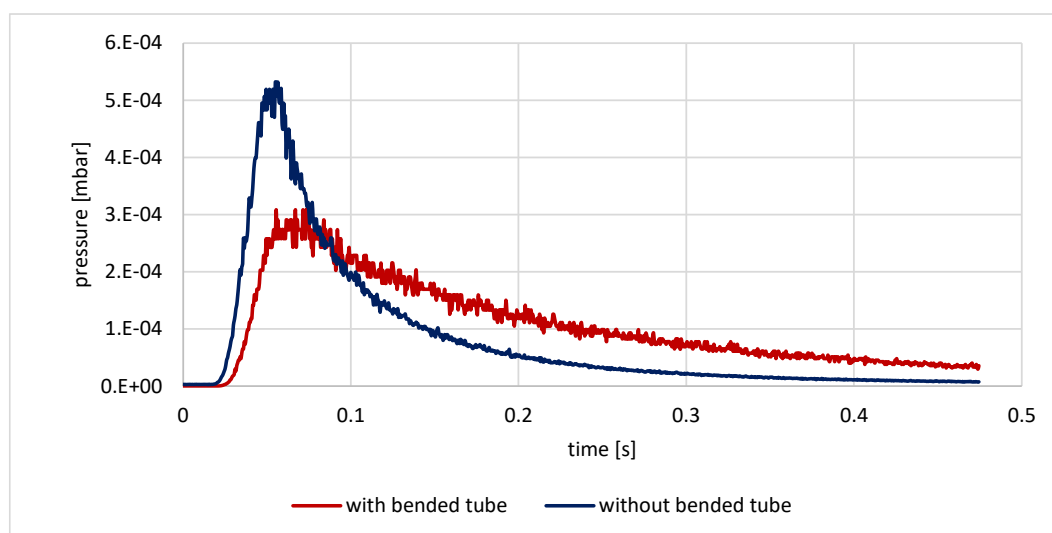


Figure 57: Transient pressure profile with (red trace) and without (blue trace) the bended tube.

### 4.5.2. Design II: straight ceramic tube

To achieve a high particle density within the ion trap on the one hand and a faster pump-down rate on the other hand the gas inlet is redesigned. A straight ceramic tube (length: 90 mm, ID: 4 mm) connects a second gas inlet at the basis flange with a hole in the ring electrode. Since the ceramic tube is firmly attached to the ring, the sample gas is directly introduced into the ion trap.

### Analysis of the pressure profile

For the newly designed gas inlet the pressure profile is examined using the two established analysis methods. Measurements are carried out with a mixture of 1 ppmV toluene diluted in nitrogen. The pressure gauge data show a comparable steeply rising pressure profile as obtained after removal of the bended metal tube. Figure 58 (left) depicts the pressure measured at the pressure gauge in dependence of three different gas inlet lengths (15, 20 and 25 ms). With increasing gas inlet length the amount of introduced gas is greater resulting in higher pressure maxima. Pressure maxima as well as the tailing of the pressure profile are shifted to longer times with increasing gas inlet length. Nevertheless in all three cases pressures  $< 10^{-6}$  mbar are reached within 300 ms (cf. Figure 58 right).

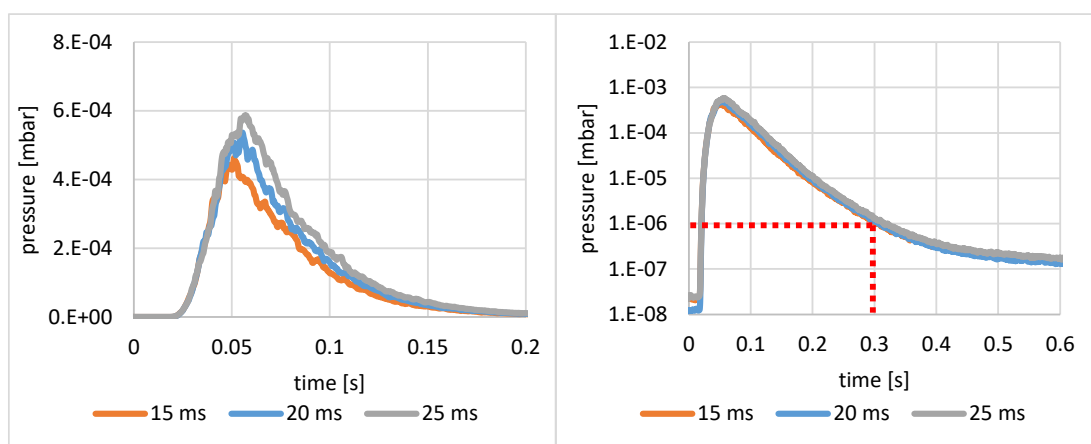


Figure 58: Left: Transient pressure gauge data recorded for different gas inlet lengths with the improved gas inlet design. Right: Logarithmic plot of the pressure gauge data shown in the left panel. Pressures  $< 10^{-6}$  mbar are reached within 300 ms.

Analysis of the pressure profile inside the trap results in significantly earlier detected ion signals compared to the pressure profiles measured at the pressure gauge. An increasing signal intensity maximum and a broadened signal response profile are observed with an increasing gas inlet length. The position of the signal intensity maximum is determined to 28 ms, whereas the pressure maximum at the pressure gauge is determined to 52 ms for the 20 ms gas inlet length (sample pressure: 2.5 mbar). The delay times between the maxima of both profiles as well as between the beginning of the initial slopes (analyte: 10 ms; pressure: 20 ms) are distinctively greater than in the results presented for gas inlet I. Figure 59 compares the analyte profile and the pressure profile, showing that the two datasets are transferable by

a simple temporal shift, as was the case for gas inlet I. Differences in the shape of both data sets as well the broadening of the pressure profile are expected due to the direct gas inlet into the ion trap and the subsequent gas removal by effusion.

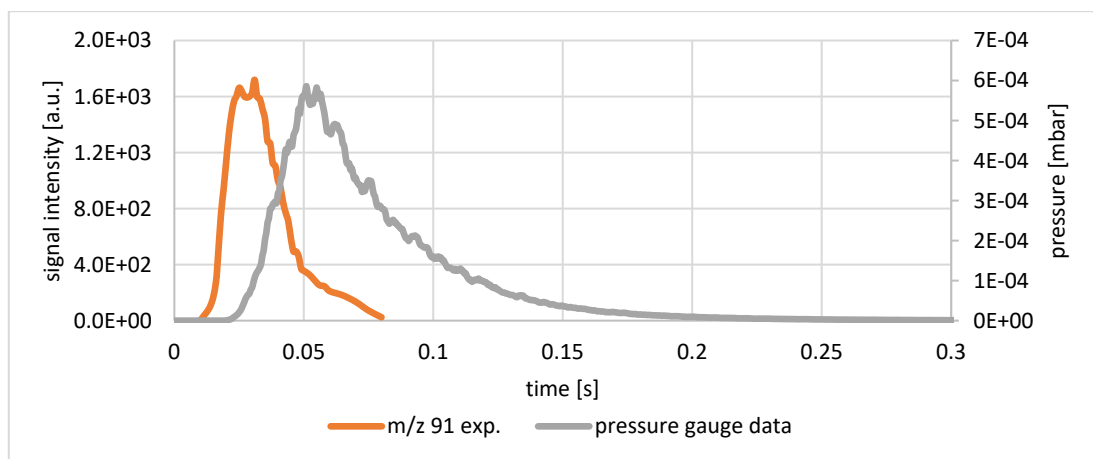


Figure 59: Transient toluene ion signal intensities and pressure data for the improved gas inlet with 20 ms gas inlet length and 2.5 mbar upstream pressure.

#### 4.5.3. General results of pressure profile analysis

The above presented results obtained by recording of the pressure gauge data and analysis of ionization time dependent ion signal intensities in the QIT show a good agreement when using gas inlet design I. Since all examined analytes showed similar temporal responses, an influence of potential ion-molecule-reactions affecting the signal intensities can be excluded. As the bended metal tube only allows an incident gas flow onto a hole in the endcap electrode the QIT as well as the entire recipient are filled with gas almost simultaneously to the same background pressure. The temporal shift between the analyte signal profile and the pressure profile is explained by the pressure gauge response time.

For gas inlet design II the pressure gauge and the signal intensity transient are not directly comparable anymore. Since the ceramic tube is connecting the gas inlet valve and the QIT, the ion trap volume is initially filled with the sample gas and then particles effuse from the trap into the volume of the recipient. Thus, a temporal shift between analyte signal and pressure signal as well as a broadening of the pressure profile is expected.

In all experiments using the ceramic tube as gas delivery stage, an overall steeper pressure transient is observed (cf. Figure 60 and Figure 61). Taking the pressure gauge data as a basis, a pressure  $< 10^{-6}$  mbar is reached after 300 ms compared to 600 ms with the bended tube.

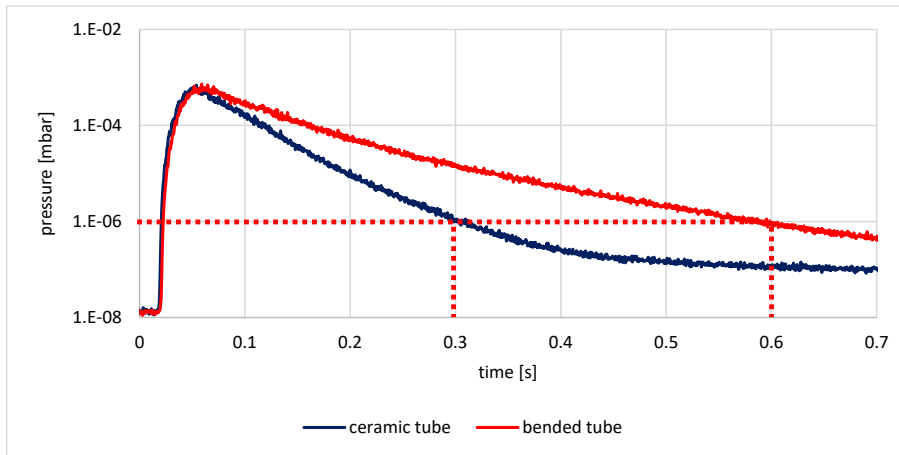


Figure 60: Transient pressure gauge data for both gas inlet designs. With the bended tube the time until  $p=10^{-6}$  mbar is reached is two times longer.

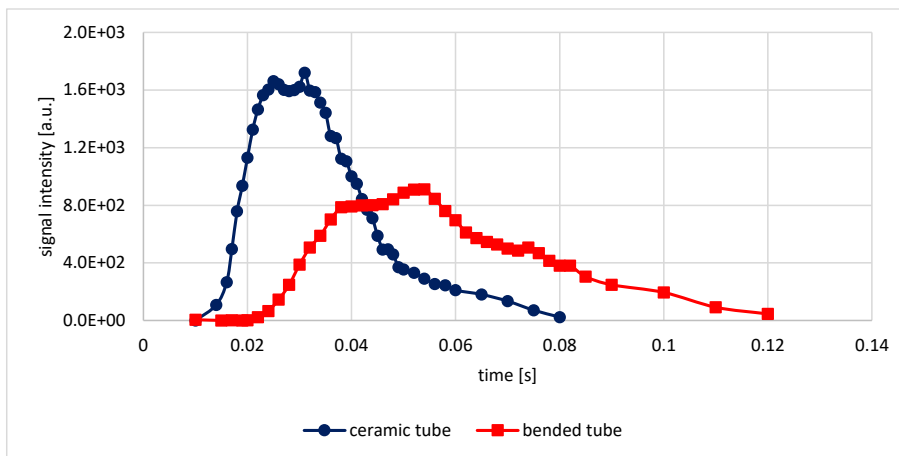


Figure 61: Transient analyte ion signal response compared for both gas inlet designs: Red trace bended tube, blue trace ceramic tube.

#### 4.5.4. Determination of the pressure inside the ion trap

As suggested by the good agreement of both pressure measurement methods for gas inlet design I, an equal distribution of particles in the trap and in the entire recipient is assumed. Hence, the measured pressure at the gauge is closely reflecting the pressure inside the ion trap. In addition, the fact that both data sets can be transferred into each other by a small temporal shift of 10 ms offers a huge advantage for the routine QIT operation: To estimate the pressure profile within the trap, the reading of the pressure gauge is a sufficient tool. The analysis of the analyte signals is not necessary. Recording of the pressure gauge data is done within a couple of seconds whereas the QIT method takes up to two hours including time for data post processing.

For the analysis of the transient pressure profile within the ion trap using gas inlet design II, one cannot avoid the QIT data acquisition since a simple conversion of pressure gauge reading and the gas density within the trap is not possible.

With the analyte mixing ratio being proportional to the total number of particles, the analyte mixing ratio is also proportional to the pressure. Thus, the analytical response of the ion trap is depicting the partial pressure of the analyte, here toluene. Assuming that the measured pressure for gas inlet I is truly reflecting the pressure inside the ion trap, a calculation of the trap pressure using gas inlet II is possible. Therefore ion signal measurements for both gas inlet designs under identical measurement conditions are required. The measurements shown in Figure 61 are carried out using a 20 ms gas inlet pulse sampled out of 2.5 mbar. Identical settings for the filament current, ionization time, timing of the excitation pulse, and length of the FFT window are chosen. The analyte signal intensity is in both cases depicting the toluene partial pressure. Comparison of the analyte signal profile and the measured pressure profile for gas inlet design I leads to a toluene partial pressure that is corresponding to a maximum pressure of  $7 \cdot 10^{-4}$  mbar. Since identical measurement parameters are chosen, the same signal response for toluene in both cases is expected. Thus the ratio of the maxima of the analyte signal profiles is reflecting the ratio of the maximum trap pressure in both setups and is given by a value of almost 0.5. Hence, a maximum trap pressure for gas inlet II of  $1.4 \cdot 10^{-3}$  mbar is determined.

#### 4.5.5. Signal loss with increasing sample pressure

As already discussed an increasing sample pressure translates to an increased number of gas molecules entering the ion trap and eventually an elevated number of generated ions. Sample pressure and gas inlet length must be chosen carefully to avoid a burn out of the filament. Figure 62 shows the measurement of 500 ppbV toluene in nitrogen while varying the sample pressure in the range of 0.8 to 9.2 mbar. All further parameters are kept constant. The first event within a measurement cycle is the 20 ms gas inlet pulse (section 0 – 20 ms), followed by a 5 ms ionization time (section 25 – 30 ms). The 3.5  $\mu$ s excitation pulse is applied at 900 ms delay time. The trapping field is adjusted to 350 V<sub>RF</sub>. With a filament current of 1.7 A even at low sample pressures of 0.8 mbar a significant ion signal for toluene at  $m/z$  91 is observed in the mass spectrum. An increase of the sample pressure up-to 2.5 mbar shows a rise in signal intensities by a factor of roughly 2. Further increasing the sample pressure, however, causes a loss in the signal abundance of  $m/z$  91. Eventually, at 9.2 mbar no toluene dependent ion signal is detected at all.

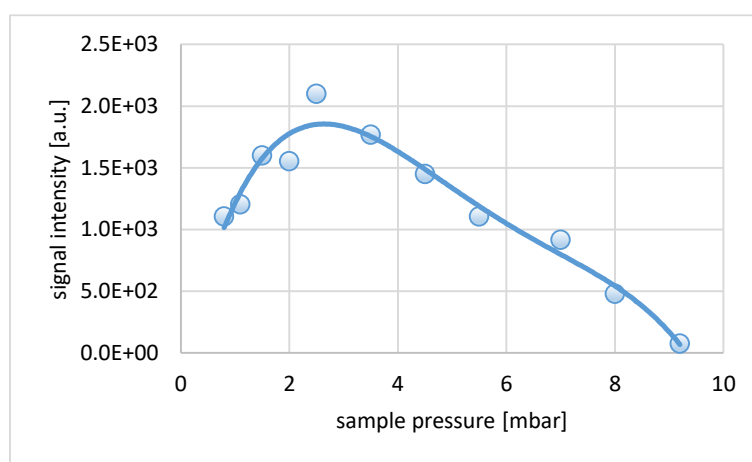


Figure 62: Toluene signal intensity for  $m/z$  91 in dependence on the upstream sample pressure.

This measurement is well in accord with the data presented in chapter 4.3.1. An increase of the sample pressure at constant ionization time and filament current causes an elevated number of generated ions. Since nitrogen is the main matrix gas, a large number of matrix ions is present leading to a space charge induced loss of the toluene signals. It is assumed that in the present case as well the application of appropriate SWIFT signals reduce the amount of interfering ions and thus will help to detect toluene signals even at elevated sample pressures.



## 4.6. Optimization of operational conditions

The experiments discussed so far were carried out to point out the extent the analytical performance is affected by the selected operational conditions. As the influence of a number of parameters is rationalized, an optimization of the operational conditions becomes feasible.

The very uncommon pulsed gas inlet into the analyzer and thus the transient pressure profile in the trap strongly determine the entire measurement sequence. The pressure profile within the trap is mainly defined by the chosen gas inlet type, the valve opening time and the sample pressure. Figure 63 shows the pressure profile recorded for gas inlet design I while sampling from 2.5 mbar with a valve opening time of 20 ms. According to the results reported in chapter 4.5.4 the profile is shifted by 10 ms to represent the effective pressure within the ion trap. Based on this effective pressure profile the further measurement sequence parameters are adjusted. Maximum ion yield is reached while ionizing in the gas pulse maximum, i.e., when the total number of neutral molecules is at maximum. Depending on the expected analyte mixing ratio the length of the ionization pulse needs to be adapted. It is noted that an ionization particularly at elevated ionization lengths results in a large amount of matrix ions. In addition, quantification is hardly possible at strongly elevated ionization lengths as the gas pulse maximum is quite steep and ionization times  $> 15$  ms cover partly the falling slope of the pressure curve. As discussed, the total ion load and related space charge induced effects are minimized by the application of SWIFT. In the performed measurements the application of SWIFT waveforms (for around 10 ms) during ionization is most efficient. At longer ionization times SWIFT waveforms are applied 5 ms prior to the end of the ionization time. This leads to a rapid elimination of unwanted matrix ions. Additionally ion-molecule reactions that may potentially adversely affect the analyte signal response are suppressed. The time until suitable FT analysis pressure conditions are reached is governed by the ion storage phase. In the present case a pressure  $< 10^{-6}$  mbar is reached within 600 ms, thus representing the minimum dwell time until ion excitation is applicable. The length of the recorded transient ion signal is depending on the pressure and on the number of stored ions. For the acquisition of longer transient ion signals and thus better mass resolutions, an extension of the ion storage phase to reach lower background pressures will be helpful. The adaption of the measurement sequence parameters to the experimentally determined pressure profile for gas inlet I are

schematically depicted in Figure 63. The measurement sequence parameters for gas inlet II are adapted in the same fashion.

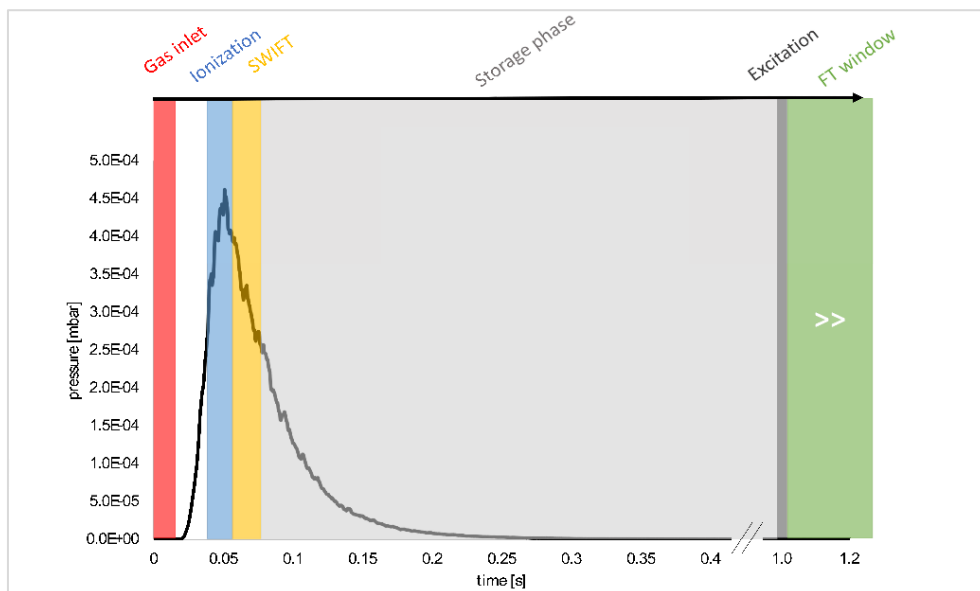


Figure 63: Sketch of the measurement sequence adapted to the transient pressure profile inside the ion trap.

For residual gas analysis the influence of the operational conditions is much smaller. As residual gas analysis is typically carried out at background pressures  $< 10^{-8}$  mbar optimum pressure for the ion detection phase is already given. Solely the length of the ionization pulse needs to be adjusted. As at  $10^{-8}$  mbar the total number of present analyte molecules is orders of magnitude smaller than in the pulsed gas sample mode, ionization lengths of up-to several hundreds of ms are required and well feasible.

#### ***Transient ion signal: Gaining first information***

Although the mass spectrum is the most relevant information acquired in both, residual gas analysis as well as for gas sampling, useful information on the measurement quality can already be obtained by inspection of the transient ion signal. The shape and the amplitude of the transient signal as well as the duration meaningful ion signals are contained in the transient are the most important factors.

Since the displacement of ions in z-direction is reduced by collisions with other neutrals and ions, an exponentially decreasing signal amplitude is expected. At elevated pressure

conditions inside the ion trap the ion signal in the transient is decreasing significantly faster as the collision rate is strongly enhanced. A comparison of measurements carried out at background pressures of  $10^{-8}$  mbar and  $10^{-6}$  mbar is given in Figure 64, demonstrating the dramatic ion loss at elevated pressures.

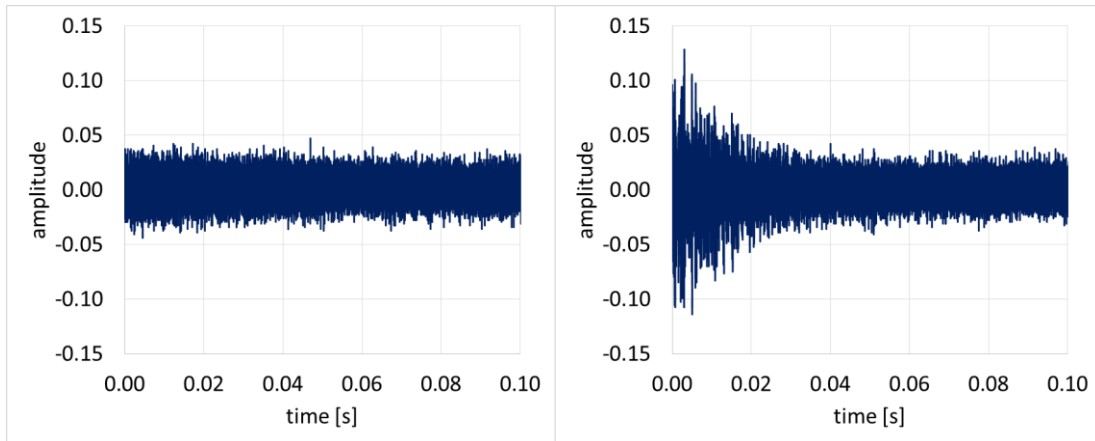


Figure 64: Transient ion signals recorded at  $10^{-8}$  mbar (left) and  $10^{-6}$  mbar (right).

Larger loss rates are also observed upon over-excitation of ions. In this case ions moving on trajectories in regions farther way from the trap center will soon collide with the electrodes and discharge. Typically, the transient signal is then initially showing a linear decrease rather than an exponential decay (cf. Figure 65).

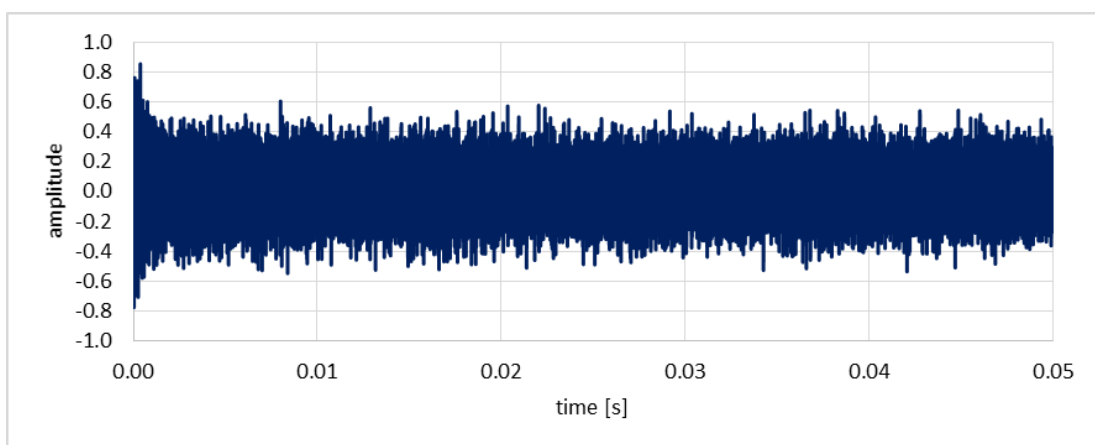


Figure 65: Transient ion signal showing a larger loss rate upon ion over-excitation.

An ion overload of the trap causes similar effects as an overall increased background pressure since the collision rate is enhanced. In addition the induced image currents on the endcap electrodes are strongly elevated causing an overload of the charge state amplifier. This results in strongly enhanced transient amplitudes as depicted in Figure 66.

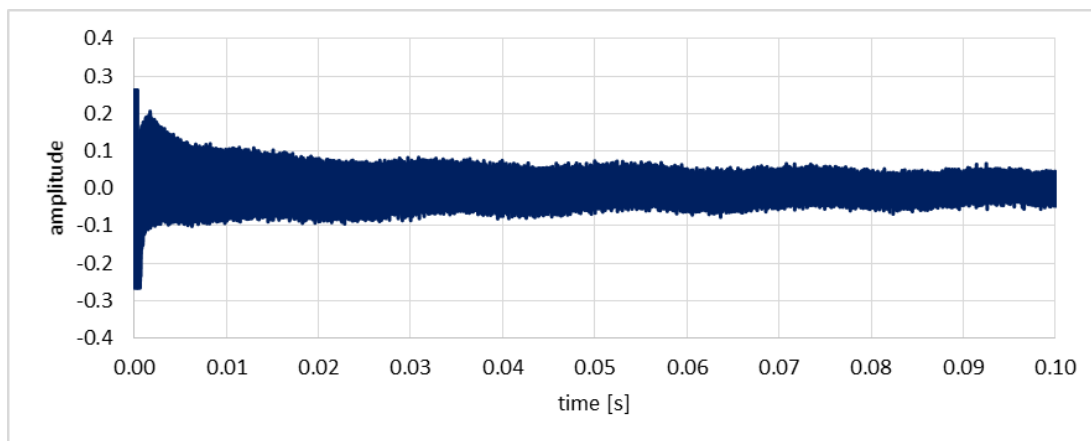


Figure 66: Typical shape of the transient ion signal upon trap overload.

With a transient signal that is significantly deviating from the ideal shape, i.e., a true exponential decay, the information gathered from the recorded mass spectrum must be handled with great care.

#### 4.7. Analytical performance

With respect to optimized operational conditions, the analytical performance as reachable with the current setup is examined in both operational modes – residual and pulsed gas sampling mode. Figures of merit are mass resolution, mass accuracy, and reproducibility. In pulsed sample mode also linear range, limit of detection, and temporal measurement resolution are investigated.

#### 4.7.1. Analytical performance in residual gas mode

##### Mass Resolution

Typical analytes in residual gas measurements at pressures  $< 10^{-8}$  mbar are hydrocarbons, carbon dioxide, nitrogen, oxygen, and water. With a trapping field of  $140 V_{RF}$ , an ionization length of 220 ms and an ion excitation after 800 ms, water ( $H_2O^+$ ,  $m/z$  18) and nitrogen ( $N_2^+$ ,  $m/z$  28) are measured as main background components (cf. Figure 67). Ion oscillations are observed within an FT-window of 100 ms. According to equation (4.39) a mass resolution of about  $R=5,500$  is determined for both ion species, since FWHM (full width at half maximum,  $\Delta m$ ) for  $m/z$  18 is given with 0.0034 Da and FWHM for  $m/z$  28 is 0.0048 Da.

$$R = \frac{m}{\Delta m} \quad (4.39)$$

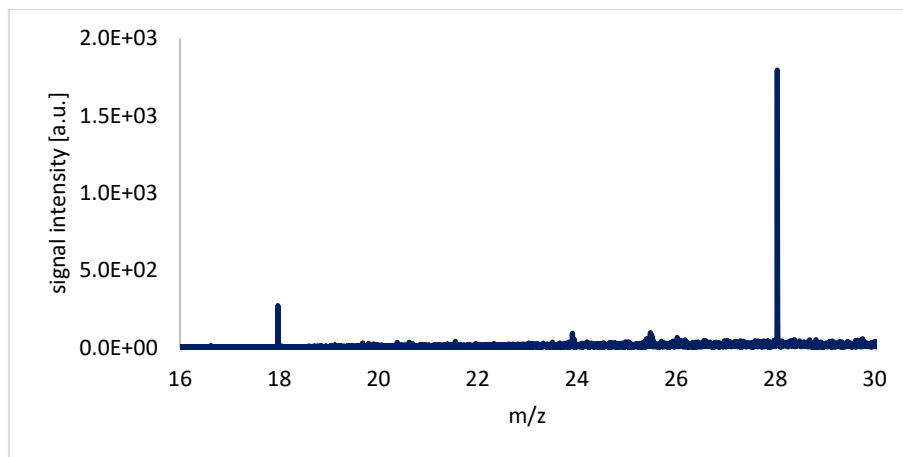


Figure 67: Mass spectrum in residual gas mode showing ion signals of water ( $m/z$  18) and nitrogen ( $m/z$  28).

##### Mass accuracy

Even highest mass resolutions are not beneficial at all, when a corresponding mass accuracy is missing. An ion trap overload, which has been shown in this work to be the main cause of mass shifts, thus needs to be avoided to the largest possible extent. Examinations on the stability of the resonance frequencies or  $m/z$  ratios, respectively, are carried out recording nitrogen mass signals at a background pressure around  $10^{-8}$  mbar within a trapping field of  $150 V_{RF}$ . This measurement has been repeated almost 10,000 times while keeping all

operational parameters constant. The trend of the detected normalized resonance frequencies in dependence of the measurement time is shown in Figure 68.

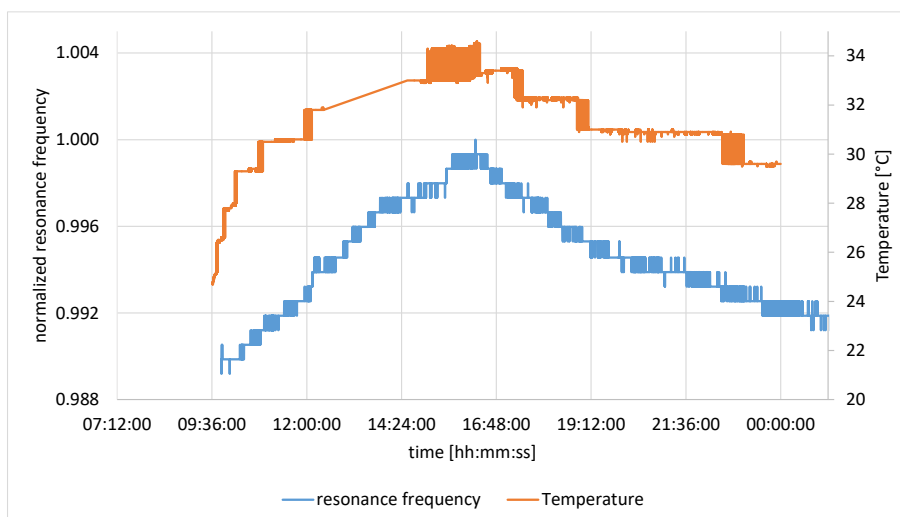


Figure 68: Long-term trend of the resonance frequency of  $m/z$  28 in a residual gas measurement (blue trace) and of the corresponding room temperature (orange trace).

Essentially, two different effects regarding the resonance frequency drift have to be considered: i) drift with time and ii) jitter between two individual measurements. The former is investigated in a more than 16 hour long term measurement as shown in Figure 68. The data exhibit a drift to a maximum of the resonance frequency until approx. 4 pm in the afternoon and then decline again to lower frequencies. Simultaneously the room temperature was recorded showing a similar trend with a maximum at approx. 4 pm (cf. Figure 68, sec. axis). This suggests a direct relation between the ambient temperature and a resonance frequency drift. This phenomenon is currently further investigated. An evaluation of the mass accuracy (or resonance frequency accuracy) at this point is thus not meaningful.

A second long-term measurement at almost constant temperature was conducted allowing the examination of water within a trapping field of  $118 V_{RF}$ . Figure 69 shows the dependence of the calculated  $m/z$  ratio on the measurement time for two measurement sections.

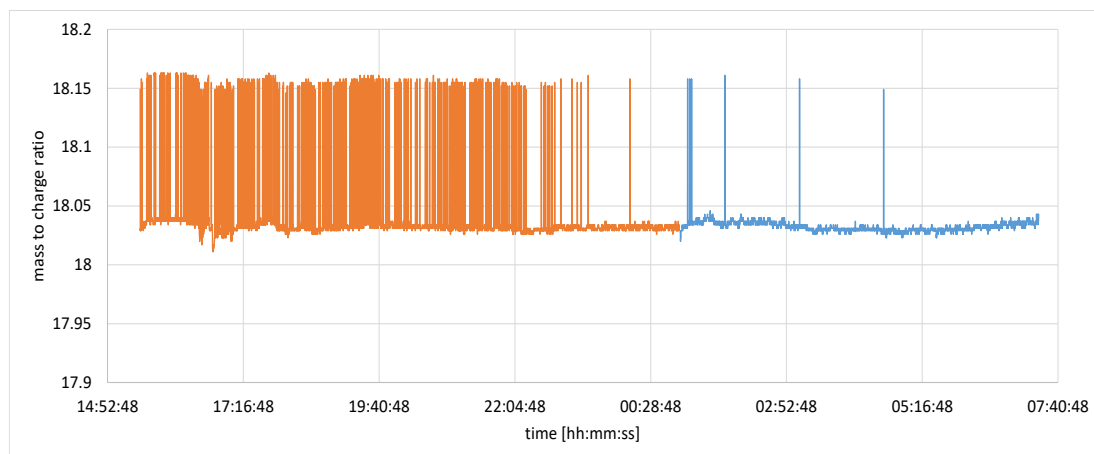


Figure 69:  $m/z$  ratios for water recorded in a residual gas measurement at constant room temperature.

Noticeable are the step-wise deviations of  $\approx 0.1$  Da, especially in the first section but also occurring in the second section. Comparison of the recorded RF trapping field amplitude with the calculated  $m/z$  ratios demonstrates that these steps are directly corresponding (exemplarily shown in Figure 70) and are thus defined as outliers. It is assumed that these outliers in the calculated  $m/z$ -ratios are a consequence of a wrongly determined trapping field voltage. Thus, for examinations on mass accuracy these outliers are removed.

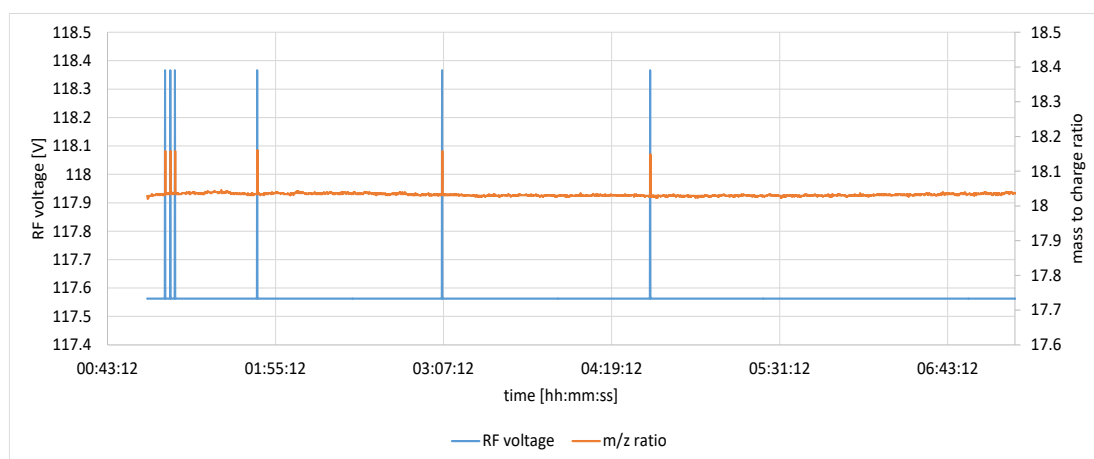


Figure 70: Observed outliers in the  $m/z$  calculation compared to the measured RF voltage.

The number of outliers in the first measurement section is with 450 out of 3,900 measurements extremely high. Removal of those faulty values leads to a mean  $m/z$  value of 18.032 Da with a standard deviation of 0.0037 Da. The mass accuracy is defined as the ratio of the  $m/z$  error and the  $m/z$  value, and is calculated to 200 ppm. In the second measurement section the mean  $m/z$

value of 18.034 Da and a standard deviation of 0.0048 Da result in a mass accuracy of 270 ppm. The distribution of the calculated  $m/z$  ratios is represented in a histogram for both measurements showing an almost Gaussian shape.

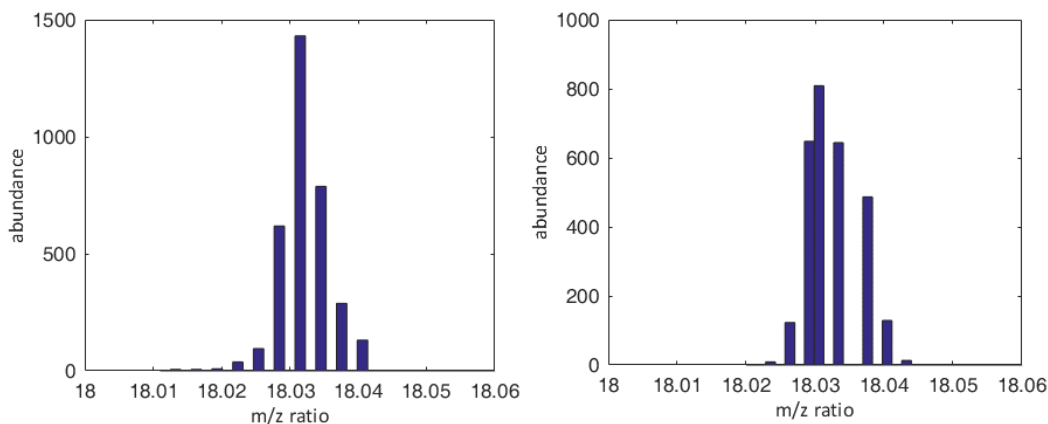


Figure 71: Histograms of the distribution of the determined  $m/z$  ratios after elimination of the outliers for the first (left) and the second (right) measurement section.

### Reproducibility

The accuracy measurements are also evaluated with regard to the analyte signal intensities to inspect reproducibility. In case of residual gas measurements one must be aware of changing mixing ratios with time as the pump-down process is proceeding. Plotting the signal intensities in dependence of measurement time, an exponentially decreasing trend is observed, as expected (cf. Figure 72). Thus the determination of mean values for the whole measurement is less meaningful. Nevertheless signal intensities compared for consecutive measurements show only small intensity variations of 12 %.

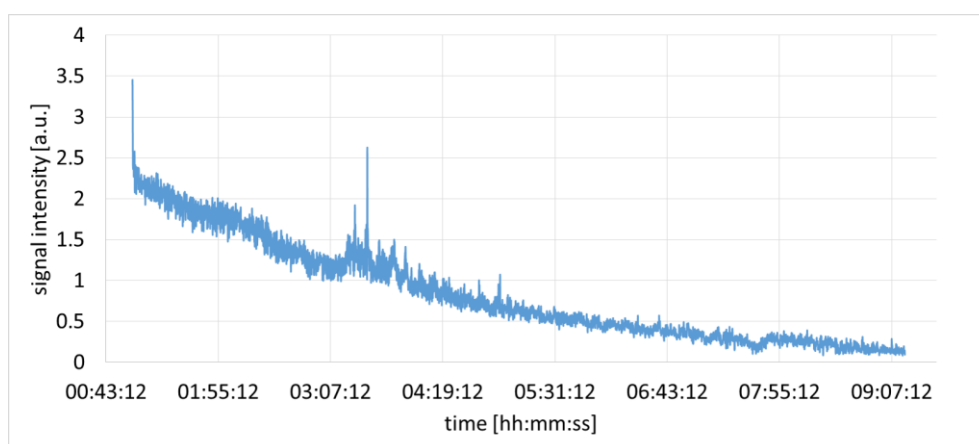


Figure 72: Trend of the signal intensities for  $m/z$  18 in residual gas mode.



#### 4.7.2. Analytical performance in gas sampling mode

##### Mass Resolution

Examinations on mass resolution in pulsed gas sampling mode are carried out using three different gas mixtures covering a mass range from  $\sim m/z$  25 to  $\sim m/z$  130: i) 1 ppmV diborane diluted in hydrogen, ii) 100 ppbV krypton diluted in nitrogen, and iii) 50 ppbV xenon diluted in nitrogen. Since the analyte mixing ratios are comparably small, SWIFT is applied to remove matrix and background ions.

Figure 73 shows a mass spectrum recorded with 1 ppmV diborane present in hydrogen. This spectrum was obtained with a 20 ms gas inlet from a 3 mbar sample pressure, an ionization time of 10 ms, the application of SWIFT 5 ms prior to the end of ionization, and ion detection after 1 s. The length of the observed FT-window is 50 ms. Five diborane fragment and isotopic ion signals at  $m/z$  23, 24, 25, 26 and 27 are detected. Only the fragment ions at  $m/z$  21 and 22 with literature abundances of 1.9 % and 11.2 % [165], respectively, are missing. An evaluation of the mass resolution for the five major peaks is summarized in Table 10.

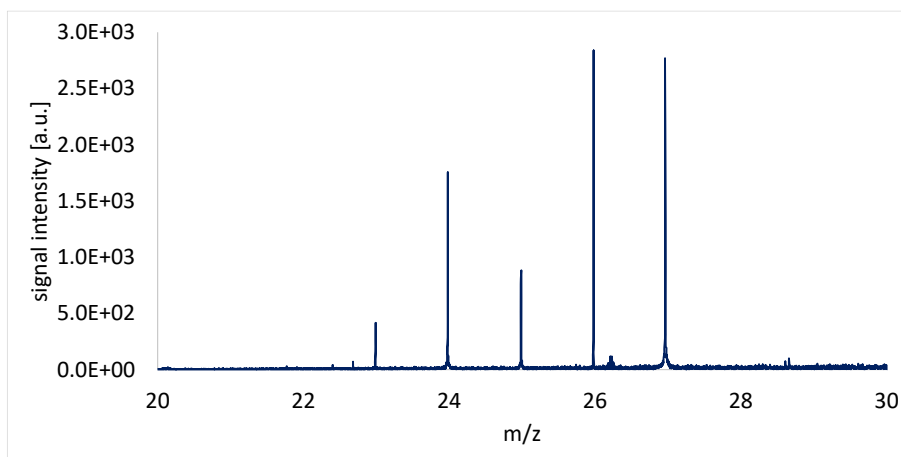


Figure 73: Mass spectrum recorded with 1 ppmV diborane diluted in hydrogen present.

Table 10: Mass resolution of diborane dependent ion signals for two FFT windows.

$m/z$ ratio	50 ms FFT window		100 ms FFT window	
	$\Delta m$	mass resolution	$\Delta m$	mass resolution
23	0.0022	10,500	0.0015	15,300
24	0.0019	12,600	0.0012	20,000
25	0.0024	10,400	0.0016	15,600
26	0.0025	10,400	0.0015	17,300
27	0.0055	4,900	0.0032	8,400

A mass spectrum recorded with 100 ppbV krypton in nitrogen present is depicted Figure 74, showing all expected isotopes ( $m/z$  82, 83, 84 and 86). This mass spectrum is obtained with a gas inlet time of 20 ms from 2.5 mbar sample pressure, 10 ms ionization, SWIFT application 5 ms prior to the end of ionization and an ion detection after 1 s. The trapping field amplitude is adjusted to 270  $V_{RF}$  and the length of the FFT-window is chosen to 200 ms. The peak width for the base peak at  $m/z$  84 is  $\Delta m = 0.0083$  FWHM, leading to a calculated mass resolution of 10,000.

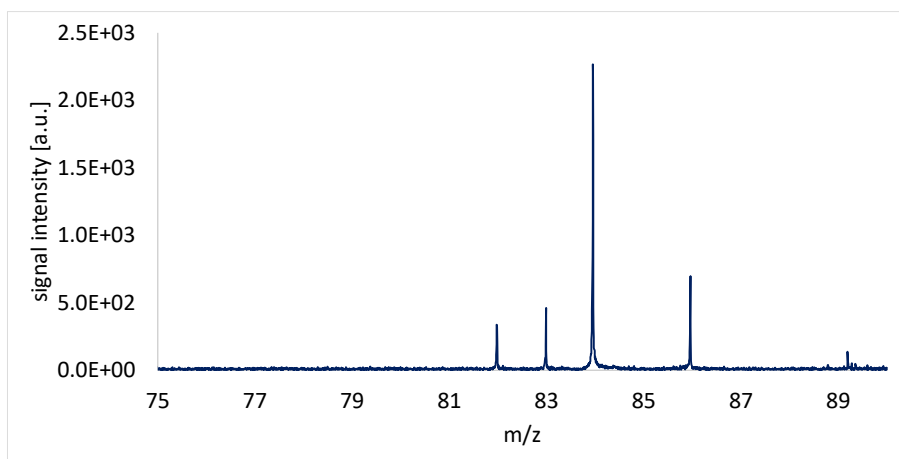


Figure 74: Mass spectrum recorded with 100 ppbV krypton diluted in nitrogen present.

The measurement of 50 ppbV xenon is recorded with a similar set of measurement parameters, only increasing the trapping field voltage to 340  $V_{RF}$ . Five of the known seven stable isotopes are detected with almost correct relative abundances (Lit:  $^{128}\text{Xe}$  (1.9 %),  $^{129}\text{Xe}$  (26.4 %),  $^{130}\text{Xe}$  (4.1 %),  $^{131}\text{Xe}$  (21.3 %),  $^{132}\text{Xe}$  (26.9 %),  $^{134}\text{Xe}$  (10.4 %),  $^{136}\text{Xe}$  (8.9 %) [164]) (cf. Figure 75). The two

isotopes with lower abundance, however, are hardly distinguishable from noise. The peak width and calculated mass resolution are summarized in Table 11 for the five major peaks.

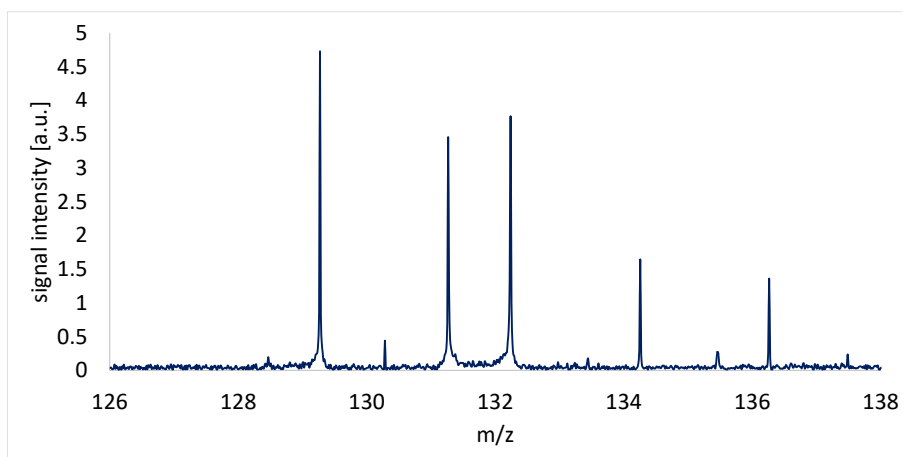


Figure 75: Mass spectrum recorded with 50 ppbV xenon diluted in nitrogen present.

Table 11: Mass resolution of xenon isotope signals for two FFT windows.

<i>m/z</i> ratio	50 ms FFT window		100 ms FFT window	
	$\Delta m$	mass resolution	$\Delta m$	mass resolution
<b>129</b>	0.069	1,900	0.017	7,800
<b>131</b>	0.034	3,900	0.020	6,600
<b>132</b>	0.044	3,000	0.021	6,300
<b>134</b>	0.034	4,000	0.018	7,600
<b>136</b>	0.070	1,900	0.018	7,500

In all three cases the mass resolution is greater than 5,000. From FT-QIT theory it is known that mass resolution decreases with increasing *m/z* ratio since ions with higher *m/z* ratio oscillate slower. Thus on average these ions are passing the detector electrodes fewer times leading to less information in the transient ion signal [9, 52]. A decrease in mass resolution is observed within the regarded mass range, but still showing good resolution at higher *m/z*. The measurement of xenon demonstrates the gain in information due to the evaluation of a larger FFT window.

### Mass accuracy

For investigations on mass accuracy in the pulsed sample mode toluene (500 ppbV in N<sub>2</sub>) is used as analyte. While sampling from 2.5 mbar with a gas inlet time of 20 ms, an ionization time of 5 ms generates a sufficient number of analyte ions detected on  $m/z$  91. As the ionization time is carefully adjusted, space charge induced effects are minimized without application of SWIFT. Avoiding a slow permanent increase in the background pressure, a waiting time of 30 s is applied between each measurement. Figure 76 shows the  $m/z$  ratio in dependence of the measurement time.

In analogy to the experiments carried out in the residual gas mode a constant shift of the  $m/z$  ratio is noticed. The RF voltage is verified to be constant (340 V<sub>RF</sub>) in the entire measurements series, excluding mass shifts caused by errors in the recorded RF voltage as observed in residual gas mode. The room temperature shows a continuous increase from 26°C to 32°C within the timeframe of this experiment. In residual gas mode a dependency of resonance frequency shift with temperature shift has already been noticed: an increase of the ambient temperature causes an increase of the resonance frequency. In this experiment  $m/z$  ratios are plotted. Since the calculated mass is inversely proportional to the frequency, a corresponding  $m/z$  ratio shift is expected. This correspondence is observed in the current measurement. While the temperature is rising, the  $m/z$  ratio is continually decreasing. A calculation of the mass accuracy over the entire experimental time frame is thus not helpful. More interesting though, are the deviations between single measurements as shown in Figure 77.

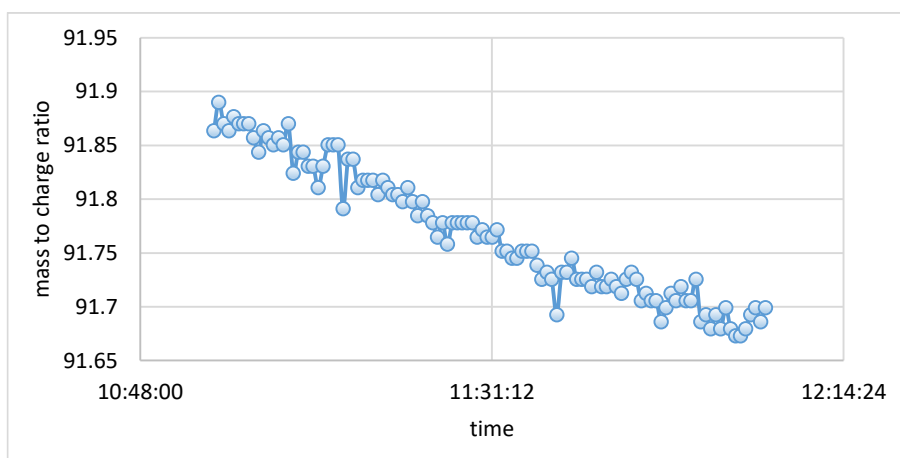


Figure 76: Trend of the calculated  $m/z$  ratio for toluene (91 Da) over time in pulsed sampling mode.

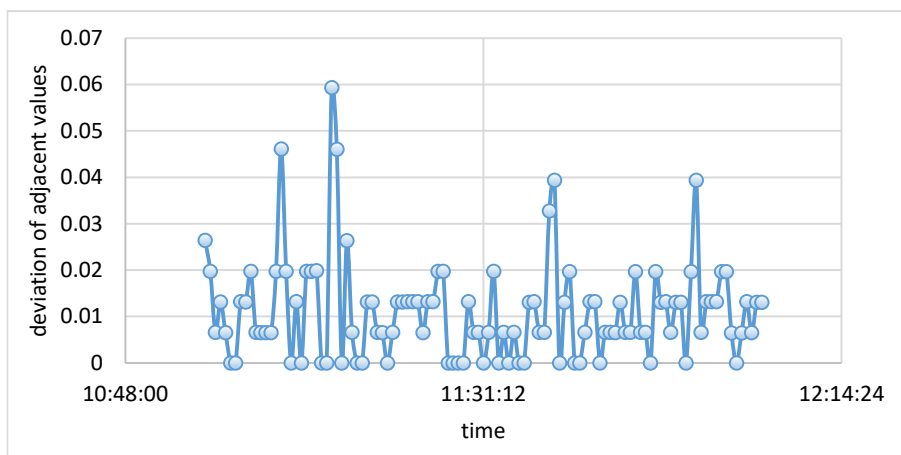


Figure 77: Jitter in the  $m/z$  ratio for consecutive measurements.

The maximum mass shift between two measurements is 0.06 Da, whereas most deviations are within a range of 0.02 Da. It is noted that the minimum noticeable shift is about 0.007 as step function, which strongly suggests that the best case accuracy is about 80 ppm at 91 Da. The analysis of the mean value allows the determination of the mass accuracy when temperature shifts are avoided. With  $\Delta m=0.043$  Da at a  $m/z$  ratio of 91 Da, the mass accuracy is calculated to 470 ppm.

The mass accuracy in residual as well as in pulsed gas mode are comparable. Only the observation of continuously shifting masses and the relation with room temperature require further inspection. It is mentioned that the new generation FT-QIT system allows the setting of an actively controlled QIT temperature. Initial measurements have shown a strongly improved performance with respect to mass accuracy, when space charge is minimized.

### *Linear range and limit of detection*

Experiments examining the linear range and the limit of detection are carried out with toluene diluted in either nitrogen or hydrogen. Following the discussion above it is apparent that with the same set of parameters only a rather limited linear range covering 2 orders of magnitude is achievable, without suffering from e.g. space charge induced effects. Space charge will inevitably be generated by extended ionization times required at low analyte mixing ratios. At elevated mixing ratios much lower ionization times already lead to large ion

loads. Thus the total number of ions inside the trap is the only parameter that needs to be adjusted by the length of the applied ionization pulse in order to avoid space charge effects. It is demonstrated, that linearity over more than two orders of magnitude is reachable via normalization of the analyte ion signal intensities. This normalization is a simple division of the analyte signal intensities with the length of the applied ionization pulse as exemplarily shown for the measurement of toluene in Table 12. All further parameters, as gas inlet (20 ms from 2.5 mbar), application of SWIFT (5 ms prior to the end of ionization), RF trapping field ( $340 V_{\text{RF}}$ ) and time for the excitation pulse (2.3  $\mu\text{s}$  after 900 ms) are kept constant.

Table 12: Normalization of signal intensities.

<b>mixing ratio [ppmV]</b>	<b>ionization time [ms]</b>	<b>signal intensity [a.u.]</b>	<b>norm. signal intensity [a.u.]</b>
0	10	736	73.6
0.01	10	1,094	109.4
0.02	10	1,519	151.9
0.03	10	1,552	155.2
0.04	10	2,035	203.5
0.05	10	2,023	202.3
0.1	10	3,466	346.6
0.25	7	4,674	667.7
0.5	4	4,566	1,141.5
0.9	1	1,824	1,824.0
1.7	1	3,307	3,307.0
3.3	0.5	2,984	5,968.0

At elevated mixing ratios of 3.3 ppmV an ionization length of 0.5 ms generates a toluene signal with rather large abundance. For the detection of 10 ppbV, however, an extension of the ionization length to 10 ms is necessary for a reasonable signal response. The linear response is given when plotting the normalized signal intensities in dependence of the analyte mixing ratios (cf. Figure 78). It is thus clearly demonstrated that an extension of the linear range due to a signal normalization is feasible. This range may be extended even further by application of shorter ionization times, which is currently not possible.

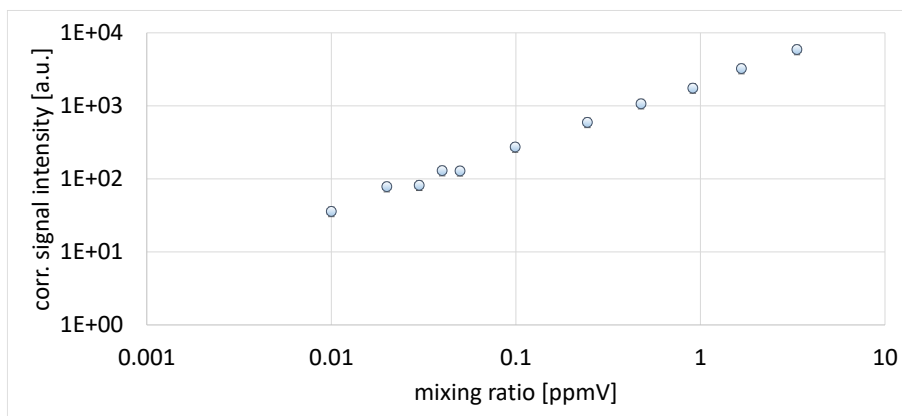


Figure 78: Dilution series of toluene in nitrogen using normalized signal intensities.

Figure 79 shows a mass spectrum recorded in the presence of a mixture of 10 ppbV toluene in nitrogen in the range  $87 < m/z < 95$ . For sufficient analyte ion generation the ionization pulse is adjusted to 10 ms. As main toluene ion species the  $[M-H]^+$  at  $m/z$  91 is detected with a signal to noise ratio of 28. This is considerably larger than the definition for the LOD by Kaiser and Specker [166], which is  $S/N = 3$ . The linear response for toluene mixing ratios in the lower ppbV range is shown in Figure 80. The slope is obtained by linear regression allowing an extrapolation to a signal to noise of 3. The limit of detection is determined to 1 ppbV.

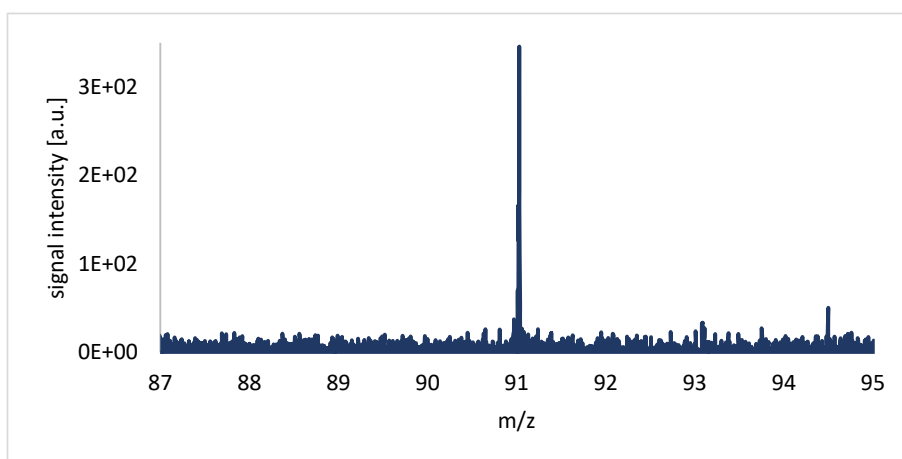


Figure 79: Mass spectrum recorded with 10 ppbV toluene diluted in nitrogen present leading to  $[M-H]^+$  at  $m/z$  91.

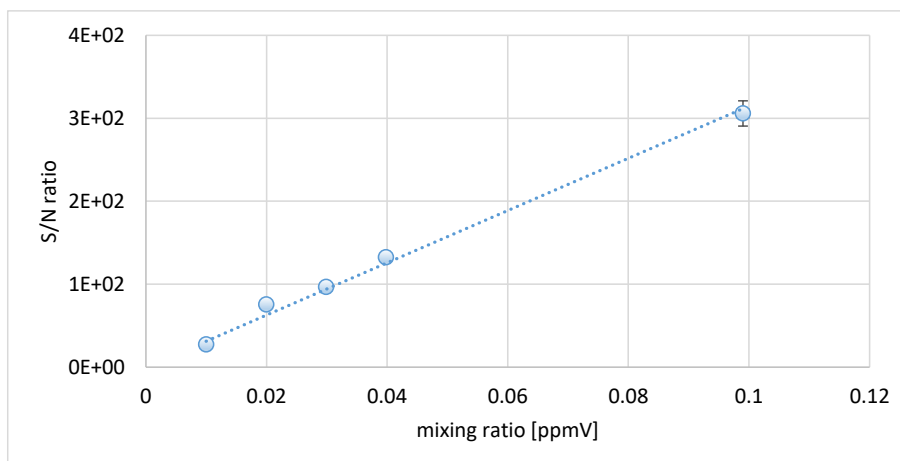


Figure 80: Signal to noise ratio of  $m/z$  91 in dependence of the toluene mixing ratio.

Similar measurements with toluene present at lower mixing ratios in hydrogen also lead to a LOD of 1 ppbV upon extrapolation of the signal response. The observed analyte ion signal is the  $[M+H]^+$  at  $m/z$  93 since analyte protonation predominates in the presence of hydrogen as matrix gas. The extension of the linear dynamic range to 4 orders of magnitude with the analyte signal intensity to ionization pulse length normalization is also successfully demonstrated.

#### *Extent of ion-ion and ion-molecule chemistry*

The above presented measurements were performed using gas inlet design II. Due to the direct gas introduction into the ion trap a significant reduction of the ionization time by a factor of almost 4 compared to measurements with gas inlet design I is possible at lower analyte mixing ratios. The importance of shorter ionization times becomes apparent when examining the dilution series of toluene in nitrogen performed with gas inlet design I. Covering the analyte mixing ratios in the range of 1 ppbV and 10 ppmV ionization times from 35 ms down to 0.5 ms are applied. In a double logarithmic plot (cf. Figure 81) the normalized signal intensities for  $m/z$  91 are plotted in dependence of the toluene mixing ratios. Surprisingly, non-linear behavior is observed for lower mixing ratios and thus extended ionization times.



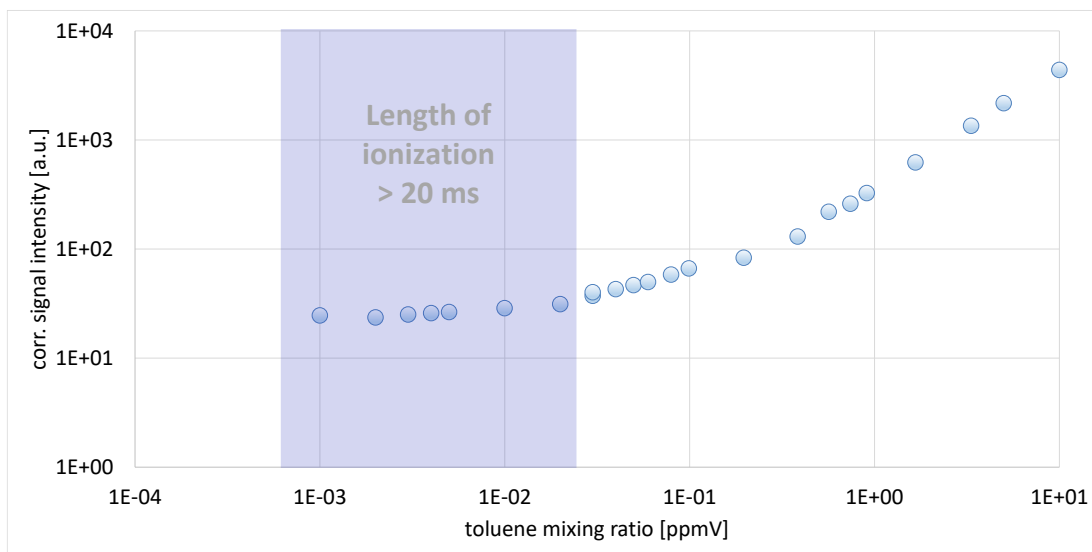


Figure 81: Double logarithmic plot of the toluene dilution series using gas inlet design I with elevated ionization times using normalized signal intensities in dependence of the toluene mixing ratio.

In Figure 82 a mass spectrum recorded in the presence of 10 ppmV toluene (0.5 ms ionization time, red trace) and a spectrum of 100 ppbV toluene (35 ms ionization time, blue trace) are compared, showing a significantly larger abundance of  $m/z$  93 at lower toluene mixing ratios. With electron ionization mainly  $m/z$  91 ( $[M-H]^+$ ) and  $m/z$  92 ( $M^+$ ) are expected, as well as a small amount of  $m/z$  93 reflecting the C-13 isotopic peak.

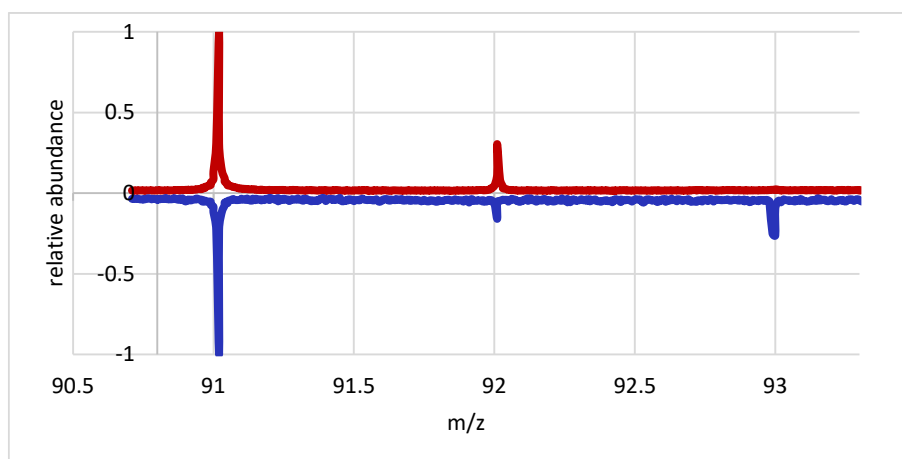
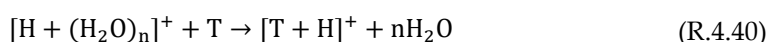
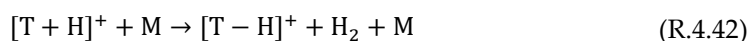
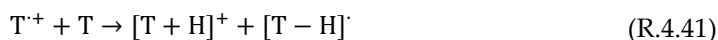


Figure 82: Mass spectrum recorded with 10 ppmV (red trace) and 100 ppbV (blue trace) of toluene diluted in nitrogen present (see text for details).

Lower mixing ratios call for longer ionization times and thus longer times for ion-molecule interactions inside the ion trap. Matrix ions, such as nitrogen species ( $N_2^+$ ,  $N_4^+$ , ...) as well as proton bound water clusters, are generated in large excess and lead to the formation of  $T^+$  ( $m/z$  92) and  $[T+H]^+$  ( $m/z$  93) according to the following reactions (with  $T$  = Toluene;  $M$  = collision molecule) [161, 167].



Furthermore chemical conversion of toluene ion species is occurring by subsequent reactions with neutral molecules [168–170].



The impact of ion-molecule chemistry on the signal distribution at elevated ionization times is depicted in Figure 83. The abundance of  $m/z$  92 and  $m/z$  93 on the sum signal of  $m/z$  91 – 93 is plotted in dependence of the ionization length. Whereas the relative abundance of  $m/z$  93 is continuously rising the abundance of  $m/z$  92 decreases with ionization time.

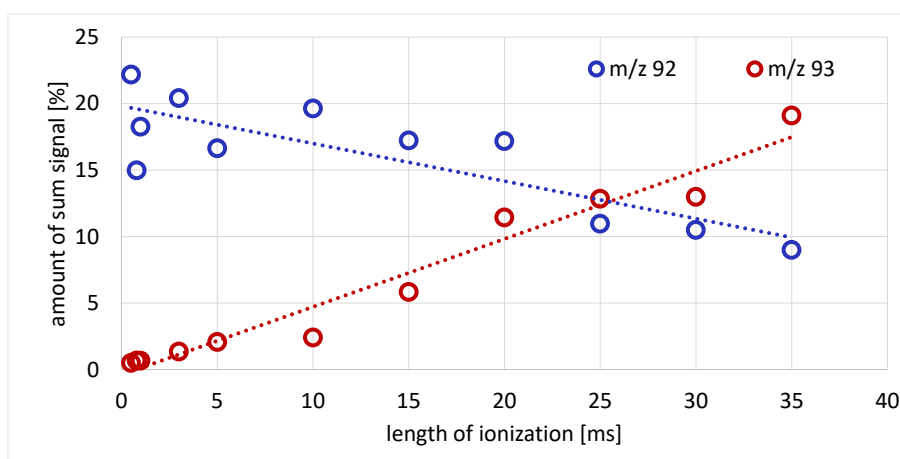


Figure 83: Relative abundances of  $m/z$  92 (blue trace) and  $m/z$  93 (red trace) in dependence of the ionization length (see text for details).

The SWIFT pulses applied within the recording sequence for matrix ion removal have a length of approx. 10 ms and are thus too short to cover the entire ionization time at small analyte mixing ratios. Further adjustment of SWIFT signals, that remove matrix ions with similar efficiency over the whole length of the ionization time is necessary to efficiently suppress ion-molecule reactions between the neutral analyte and matrix ions. Ion-molecule chemistry between analyte ion species, however, remains unaffected.

Furthermore, at elevated ionization times the ionization pulse is much longer than the width of the peak maximum of the transient pressure profile in the ion trap. Thus, ionization will not only occur in the peak maximum but also in the pressure tailing. This fact would rather lead to lower signal abundances, but must be considered, too. It is concluded that prolonged ionization lengths largely exceeding the transient pressure maximum region should be avoided.

#### *Relation between signal intensities and peak areas*

All measurements shown so far were evaluated with respect to the recorded ion signal intensities instead of peak areas. The relation between signal intensities and peak areas is thus investigated. Figure 84 exemplarily shows a dilution series of 10 ppbV to 3 ppmV toluene in nitrogen. Evaluated peak areas for each measurement point are plotted in dependence on the signal intensities resulting a linear response with an  $R^2$  value of 0.994 (cf. Figure 84). Thus, data analysis with respect to signal intensities as well as with respect to peak areas is justified.

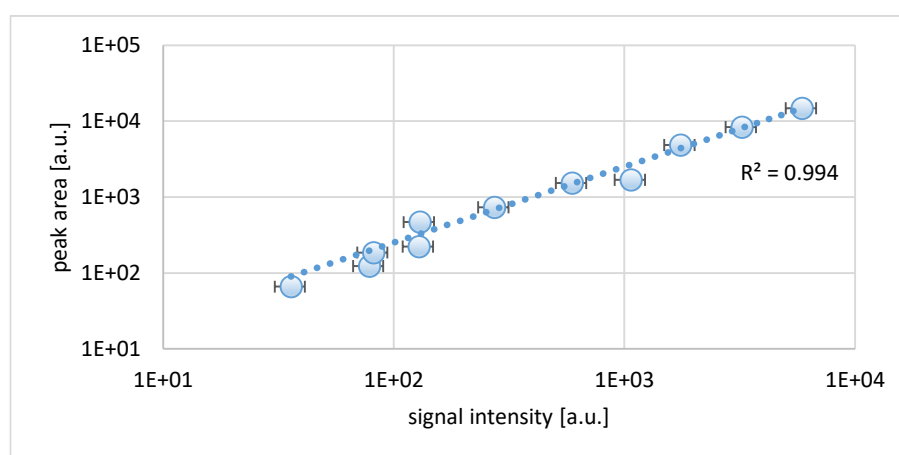


Figure 84: Correlation plot between signal peak areas and signal intensities. Both data sets are treated with previously described ionization length normalization.

### *Temporal resolution*

The temporal resolution of measurements in the pulsed gas sampling mode is essentially dominated by the pressure drop after closing the inlet valve. It has been discussed that with gas inlet design II a delay time of 300 ms is sufficient to reach suitable trap pressures  $< 10^{-6}$  mbar for the ion detection phase. Thus, the total analysis time for a single measurement is determined to be about 0.5 s. In repeated measurement cycles, however, it is noted that after each measurement sequence several seconds of an extended pumping phase are required to avoid a continuous increase of the background pressure. In consequence, the temporal resolution with the QIT operated in repeated pulsed gas sampling mode is estimated to approx. 20 s.

### *Reproducibility*

A number of sources within the entire setup and the measurement sequence is affecting the analyte signal response: i) the gas pulse characteristics, ii) the electron emission current of the filament, iii) the height of the excitation pulse, iv) the detection of image currents, to name a few. Reproducibility is examined sampling 500 ppbV toluene in nitrogen (20 ms gas inlet from 2.5 mbar). The ionization time is set to 5 ms and ion excitation is applied with a 3.5  $\mu$ s pulse after 900 ms. Avoiding any rise in the background pressure the dwell time between two measurements is set to 30 s. Figure 85 demonstrates the analyte signal intensity for  $m/z$  91 in dependence of the time of measurements showing a variance of 13 %.

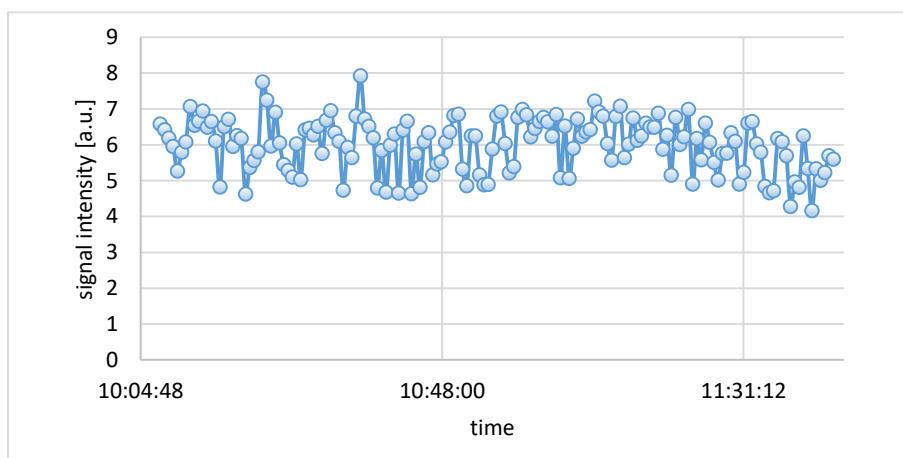


Figure 85: Trend in the signal intensities for toluene at  $m/z$  91 for consecutive measurements.

#### 4.8. *SWIFT – a powerful tool needing further investigation*

The pivotal importance and power of advanced excitation schemes, in particular of SWIFT for FT analysis based mass analyzers including the present ion trap have already been discussed in some detail in chapter 4.4. Due to the elimination of unwanted ion species by application of SWIFT waveforms, ion signal suppression is largely avoided and the measurement of components at low mixing ratios becomes possible. In addition, a reduction of the total ion load within the ion trap prevents, e.g., space charge induced mass shifts.

##### *Capability of analyzing complex mixtures*

A targeted and intelligent application of SWIFT can aid to analyze even more complex gas mixtures. With the current setup the simultaneously storable range of  $m/z$  values is about 100 Da. As long as the mixing ratios of the analytes are in the same order of magnitude, the mass spectrum represents the correct neutral analyte distribution, assumed that ion-molecule chemistry is suppressed and ionization efficiencies of the different compounds are comparable. With components present in large excess, however, the analysis of compounds at lower mixing ratios will be adversely affected by space charge and ion suppression. The application of SWIFT though in an iterative process will potentially allow the analysis of complex gas mixtures with analytes present within a broad range of mixing ratios: The first spectrum recorded will (only) show the main components (maybe the matrix gas) of the entire ion population. In a second run these main components are specifically removed from the trap, so that ion species at smaller mixing ratios can be recorded. A repetition of this process is possible as long as new ion signals appear. Summing up the iteratively measured spectra, a mass spectrum for the entire neutral gas composition is generated.

##### *SWIFT for the stimulus excitation pulse*

The application of SWIFT is not only possible during ionization or ion storage phase but can also be used as stimulus excitation pulse followed by transient signal acquisition. Thereby a targeted ion excitation of selected  $m/z$  ratios or  $m/z$  ranges is enabled while other  $m/z$  ratios are either not excited at all or removed from the trap. Stimulus SWIFT excitation is currently

under deep investigation. Such stimulus SWIFT pulses need to be much shorter to allow an immediate recording of the transient ion signal. It is pointed out that the rectangular ion excitation pulse has a length of several  $\mu\text{s}$  and the SWIFT waveforms discussed so far have lengths around 10 ms. Such a long excitation pulse applied on the endcap electrodes will inevitably lead to loss of ion information.

The application of stimulus SWIFT is integrated into the measurement software of the PreSeries Tool, which is the latest FT-QIT system generation. The user may chose the mass range, the length as well as the height of the amplitude of the SWIFT pulse. The corresponding waveform is then transparently calculated and applied to the endcap electrodes. Figure 86 shows data for  $m/z$  28 and  $m/z$  44 from a measurement carried out in residual gas mode at a background pressure of  $5 \cdot 10^{-9}$  mbar. For ion excitation stimulus SWIFT covering a mass range from 10 – 150 Da is applied while varying the length of the stimulus pulse in the range of 1 to 10 ms and the height of the signal amplitude from 0.1 to 1.

At low excitation energies characterized by short pulse lengths and small signal amplitudes only  $m/z$  28 is detected in the mass spectrum since they are insufficient for excitation of  $m/z$  44. Elevated ion energies, especially at a higher SWIFT signal amplitudes allow only the detection of  $m/z$  44 since  $m/z$  28 is over excited and thus removed from the ion trap. Figure 86 (right) shows clearly the under- and over-excitation regions framing the optimum excitation region for  $m/z$  44.

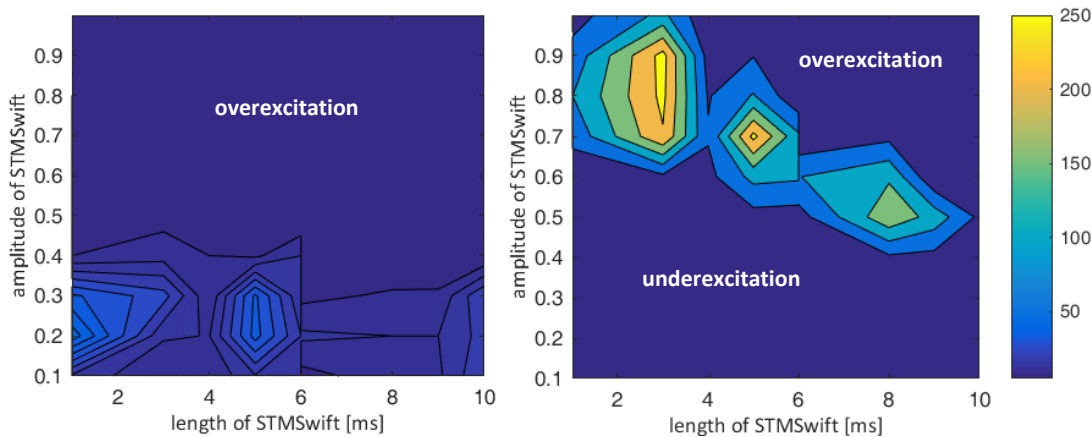


Figure 86: Variation of the amplitude and length of the stimulus SWIFT pulse showing areas of under- and over-excitation for  $m/z$  28 (left) and  $m/z$  44 (right).

This example demonstrates that stimulus SWIFT can be used for a more targeted ion excitation. With the application of the rectangular excitation pulse only  $m/z$  28 was detectable in appreciable abundance. When individual narrow mass ranges are selected for the synthesis of the stimulus SWIFT waveform rather than the entire 10 – 150 Da mass range as shown above, each targeted species can be excited at optimum conditions.

## 4.9. Plasma-coupling

### *Sensitive measurements without the need of SWIFT*

Coupling of the QIT with the plasma source as described in the Experimental section is performed in the framework of this work to gain some additional information on the QIT behavior. Toluene (T) diluted in nitrogen is the analyte of interest, sampled from a reservoir held at 100 mbar. Analyte ions are generated within the confined ionization region. With water present at elevated mixing ratios the formation of  $T^+$ ,  $[T-H]^+$  and  $[T+H]^+$  is expected. Figure 87 shows a mass spectrum recorded in the presence of 100 pptV toluene. Total measurement time for this single-shot mass spectrum is 30 s taking into account the gas delivery, ion trapping, pumping, analysis and FFT.

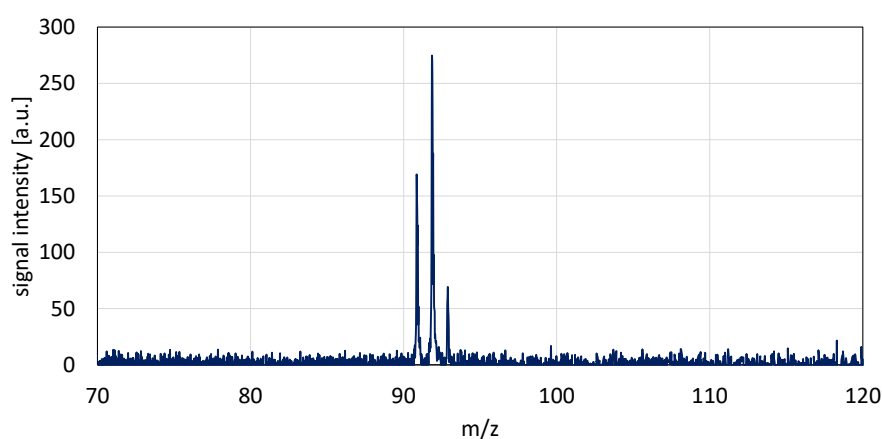


Figure 87: Mass spectrum recorded with 100 pptV toluene in nitrogen present as obtained with micro-plasma ion trap coupling.

A dilution series recorded in the range of 100 pptV to 1 ppbV shows linear response when considering the signal intensities and peak areas for  $m/z$  91 (cf. Figure 88 left). Plotting of the signal to noise ratio in dependence of the toluene mixing ratios (cf. Figure 88 right), allows the determination of the LOD ( $S/N = 3$ ), which is 130 pptV following linear regression.

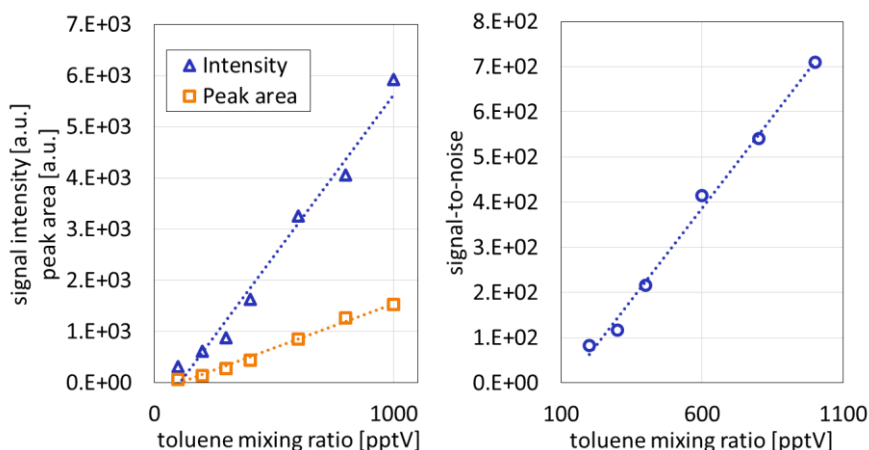


Figure 88: Signal intensities and peak areas (left) and signal to noise ratio (right) in dependence of the toluene mixing ratio.

From further experiments carried out with this plasma source e.g. with the CTOF it is known, that the total ion yield generated with the plasma source is extremely high, even generating matrix ions in large amount. Nevertheless, in the above measurements space charge and ion suppression appears to be no problem, although SWIFT is not applied. There are currently two possible explanations:

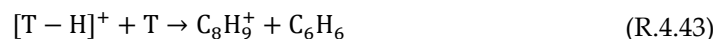
- i. Matrix ions such as  $N_2^+$ , that are not stable in the applied trapping field are rapidly lost when entering the ion trap. In case of EI in-trap ionization, however, ions with instable trajectories are generated and at least for some RF oscillations present inside the ion trap and potentially causing space charge related effects.
- ii. Since the plasma source is operated with helium a distinct helium leakage out of the small orifice into the ionization region occurs. It is assumed that despite the reversed pumping process a small neutral helium flow through the GC column is bleeding into the ion trap. In other commercially available QIT systems helium is commonly used as cooling gas. It is thus speculated that the small amount of helium introduced in this setup may have a favorable ion cooling effect.



### Repeated measurement experiments

A great advantage of the non-destructive ion detection is the fact that the measured ion population remains in the ion trap. This allows a repeated measurement of the same ion population and the targeted observation of ion-molecule reactions.

Exemplarily investigated is the chemical conversion of toluene species in hydrogen matrix upon the addition of another neutral analyte. The primary generated toluene species are the  $T^+$ , the  $[T-H]^+$  and in significantly larger extent the  $[T+H]^+$  ions due to protonation from initially generated  $H_3^+$ -ions. Toluene ion-molecule chemistry as already presented further above is further driven by a reaction also well known in the literature [168–170]:



Eventually chemical conversion leads to the formation of  $C_8H_9^+$  at  $m/z$  105 while the abundance of the primary toluene ion species decreases. This evolution is depicted in Figure 89. In a first measurement mainly the  $[M+H]^+$  as base signal in  $H_2$  matrix is observed. With the plasma source being shut off the stimulus pulse of the FT-QIT is applied in cycles of 9 s showing a relative abundance of  $m/z$  105 that is rising whereas the relative abundance of  $m/z$  93 is decreasing due to ongoing ion-molecule chemistry.

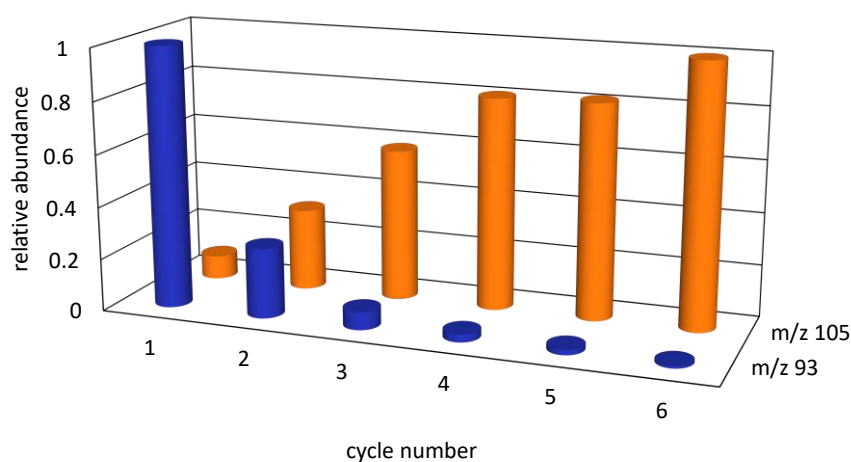


Figure 89: Temporal evolution of toluene ion species in repeated measurement experiments, showing an increase of  $m/z$  105 simultaneously to a decrease of  $m/z$  93. One cycle represents 9 seconds.

#### 4.10. Space charge induced ion coupling

From FT-ICR and Orbitrap mass spectrometers the coupling of ion populations with similar resonance frequencies is well known. This results in a single  $m/z$  ratio in the mass spectrum reflecting different  $m/z$  ratios and is addressed to coalescence coupling. This coalescence, however, is only observed at very high-resolution and affects the third or fourth decimal place of the calculated  $m/z$ .

In chapter 4.3.1 ion signal suppression caused by increased total ion loads present in the ion trap has already been discussed. Furthermore the absence of the xenon isotopes with lowest abundance has been mentioned in chapter 4.7.2. In both cases the  $m/z$  ratios are at least differing by 1 Da. Nevertheless, a similar effect as described with coalescent coupling is expected.

In the recent past initial simulations are carried out investigating the motion of ions with different  $m/z$  ratios taking into account space charge. For that purpose an ideal trap geometry with an ideal quadrupole field is assumed. As benchmark system for the simulation the chlorine radical cation isotopes at  $m/z$  35 and  $m/z$  37 are investigated. Currently the simulations are performed with 1,000 particles, 500 for each species, respectively. Without adding any additional space charge factor for consideration of ion/ion interaction a slowly decreasing transient signal is obtained leading to two separated peaks in the frequency spectrum, reflecting both ion species present (cf. Figure 90). For all three simulations the bath gas pressure is set to  $10^{-5}$  mbar with  $N_2$  as collision gas.

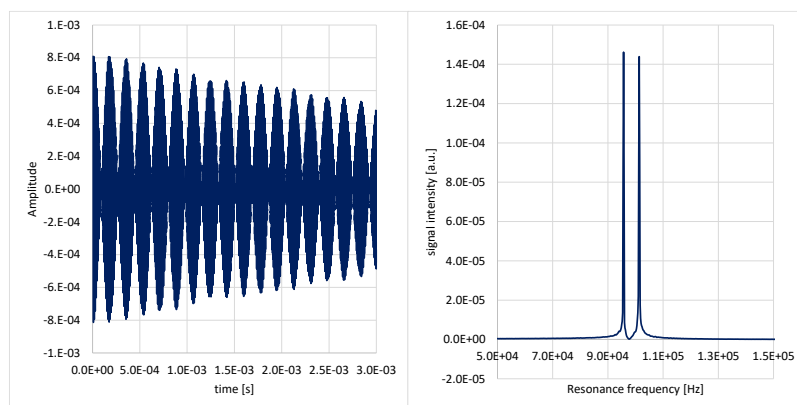


Figure 90: Simulation of  $m/z$  35 and  $m/z$  37 for a total of 1000 particles present without the consideration of space charge interactions. Left: Calculated transient signal. Right: Calculated frequency spectrum.

Space charge caused by a larger number of ions present inside the ion trap is invoked with the application of a space charge factor for each particle simulated. Ion transients and frequency spectra for two different space charge factors are shown in Figure 91 and Figure 92. With increasing number of charges inside the ion trap the transient ion signal is decreasing faster. This observation is in well accordance with the transients presented in chapter 4.6. Calculation of the simulated frequency spectra shows a significant collapsing of both signals with increasing charge state of the trap.

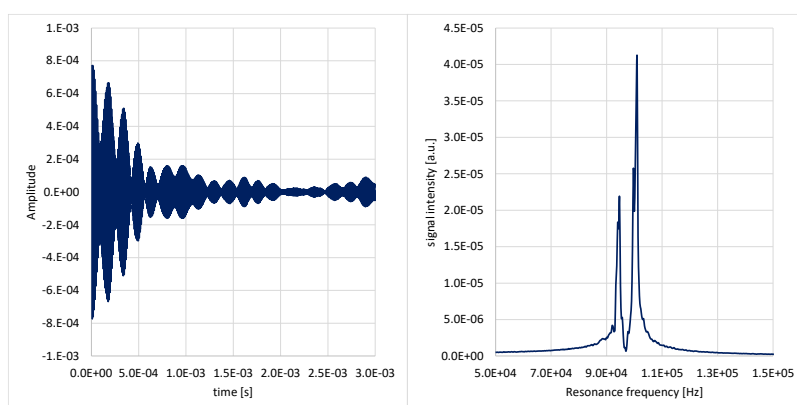


Figure 91: Simulation of  $m/z$  35 and  $m/z$  37 for a total of 1000 particles present with the consideration of space charge factor of 10. Left: Calculated transient signal. Right: Calculated frequency spectrum.

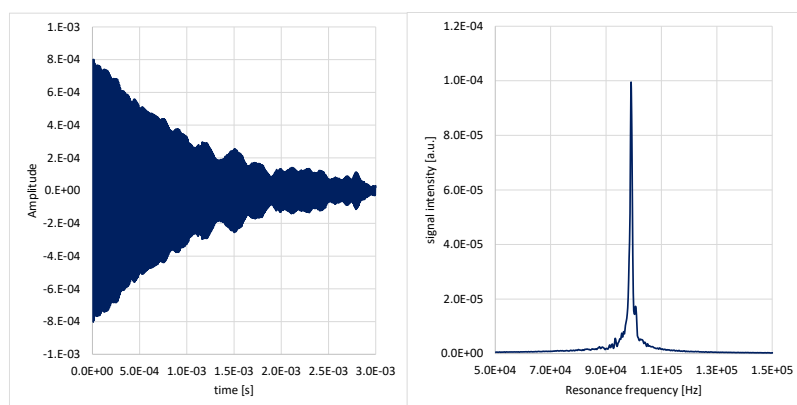


Figure 92: Simulation of  $m/z$  35 and  $m/z$  37 for a total of 1000 particles present with a space charge factor of 100. Left: Calculated transient signal. Right: Calculated frequency spectrum.

An animation of the time-dependent simulated motion of the two ion clouds within the trapping field shows that initially both clouds oscillate with their own specific frequency. Only at elevated charge states the ion clouds start to synchronize their frequencies, eventually oscillating with one frequency.

## 5. Summary and Conclusions

### *An open-heart surgery*

Boundary conditions for the design of the novel mass spectrometric setup used in this work are strictly defined, especially by robustness, cost-effectiveness, and compactness while showing an overall analytical performance exceeding that of RGAs. According to the required specifications the FT-QIT system is equipped with a direct gas inlet via a pneumatically driven valve and in-trap electron ionization.

Due to the instrument compactness requirement, analyte ionization,  $m/z$  analysis as well as ion detection are all carried out within the analyzer itself. Most commonly, however, mass spectrometers are constructed with separated regions for ionization, mass analysis and detection. This allows, e.g. an optimization of the ion source without influencing the performance of the mass analyzer. Operation of the FT-QIT though is comparable to an open-heart surgery. For instance, just a change in the amount of introduced gas will influence ionization efficiency, affect ion storage phase and at least determine the performance of the image current detection. For example, an increased amount of gas will allow a more efficient ionization whereas prerequisites for FT based ion detection are low pressures ( $< 10^{-6}$  mbar). The presence of the sample gas during the storage phase is assumed to have a favorable ion cooling effect, on the one hand, aiding to focus the ions to the center of the ion trap. On the other hand the elevated particle density translates to an increased collision frequency potentially leading to ion-molecule reactions.

Nevertheless, the present FT-QIT was successfully applied for initial analytical measurements. This required a detailed assessment of the impact of numerous operational parameters on the quality of the acquired transient signals and extracted mass spectra. The most critical parameters were identified and investigated in much more depth.

### *Influences on the signal response*

The influence of a number of parameters on the signal response in FT analyzers is known from theory or at least readily understandable. These include the trapping efficiency as function of the trapping field amplitude, the extent of the excitation due to the length and

height of the applied rectangular excitation pulse as well as the linear range of the charge state amplifier. Since the influence of the excitation pulse and the characteristics of the charge state amplifier on the signal response are well-determined their influences can be corrected in real-time, i.e., within the measurement cycles.

When analyzing complex gas mixtures one must be aware of ion-molecule-reactions when the measurement cycle provides enough time for chemistry to occur to some extent. Even within the given simple gas mixture of nitrogen and oxygen ion-molecule-reactions changed the ion distribution significantly. At first sight, the reaction probability of bimolecular reactions is reduced since the QIT is operated at reduced pressure. However, due to the oscillation of the RF trapping field ions are moving faster, resulting in elevated and more energetic collision frequencies and thus an enhanced reaction probabilities.

For successful quantitative measurements a constant electron emission current is a prerequisite. As known from literature and also demonstrated in this work the emission current can be significantly influenced by the composition of the sampled gas mixture due to the formation of, e.g. oxide layers when sampling O<sub>2</sub>.

#### *Avoiding space charge*

A major issue when examining influences on the entire QIT performance and thus ion signal responses is represented by space charge and ion trap overload. Multiple parameters can be varied to enhance or reduce the number of generated ions within the trap: length of the gas inlet, sample pressure, ionization time, and electron emission current, among others. There appears to be only a small margin between optimum yield in ion signal intensities and significant ion signal loss. Since the application of SWIFT reduces the total ion density within the trap, the maximum dynamic range reachable with the above listed parameters is strongly enhanced.

A limitation of the dynamic linear range to merely two orders of magnitude has been demonstrated for measurements carried out with a fixed set of parameters. This is in well accordance with recently evaluated ion trajectory simulations which suggest that the presence of approx. 100,000 ions (i.e., 1,000 simulated particles and a space charge factor of 100) decides whether reasonable ion signals are extractable from the transient signal or space charge induced effects (mass shift, ion signal collapse, ion signal loss) occur. Even the absence of the

xenon isotopes with lowest abundance (~2 %) is explainable due to the currently assumed maximum number of acceptable charges and the limited linearity range within a single measurement.

***Most critical parameter in FT-QIT operation: gas inlet***

The pulsed gas inlet is judged to be one of the most crucial parameters in FT-QIT operation and performance. Two major issues have been identified:

- i) The pulsed gas inlet with upstream pressures of  $> 1$  mbar leads to strongly elevated particle densities within the ion trap volume. In combination with in-trap electron ionization this causes an increased number of generated ions inevitably leading to space charge related problems.
- ii) The transient pressure profile inside the ion trap is predominantly determining the measurement sequence. Time for ionization, length of storage phase as well as time for ion excitation have to be adapted to the pressure profile allowing optimum measurement conditions.

Two different approaches for the analysis of the pressure profile were used: i) recording of the pressure gauge data and ii) examination of the analyte ion signal response. Eventually, the combination of both approaches provides a reasonable estimation of the pressure profile inside the ion trap and allows the determination of the absolute pressure in the gas pulse maximum. The characterization of the transient gas pulse allows an adaption of the measurement sequence, i.e., ionization within the pressure maximum and delayed data acquisition at suitable trap pressures for image current detection. With the current gas inlet design trap pressures  $< 10^{-6}$  mbar are reached within 300 ms. A further enhancement of the multiple measurement duty cycle in addition to a reduction of the ion collision frequency can be reached by reducing the gas load, as e.g. provided by fast switching gas jet valves. For efficient analyte ionization, especially at low analyte mixing ratios, however, elevated ionization times are necessary, which are in contradiction with shorter gas inlet pulses. An enhanced pump-down rate is only reachable by an increase of the QIT gas conductance, which translates to major re-designs of the system. Application of a faster switching valve can be of interest when sampling from elevated upstream pressures.

### *Analytical performance*

Under optimized measurement conditions the analytical performance is examined. According to the figures of merit a limit of detection for toluene of 1 ppbV in either nitrogen or hydrogen is evaluated. Mass resolution is investigated for three different analytes (diborane, krypton and xenon) showing  $R > 5,000$  in all three cases when evaluating a 100 ms FFT-window. Increased mass resolution upon applying a longer FFT-window is also observed. If significant drifts in room temperature are avoided, mass accuracy is kept  $< 500$  ppm. The linear dynamic range is limited to two orders of magnitude with a constant set of measurement parameters in response to the maximum tolerable total number charges inside the ion trap. An increase of the linear range, however, is successfully reached by a normalization of the obtained signal intensities or peak areas, respectively, with the length of the applied ionization pulse. Hence, an enhancement of the linear dynamic range to 4 orders of magnitude was successful. Further examinations on the capability of measuring complex gas mixtures due to the application of e.g. SWIFT excitation schemes are under current investigation.

### *Comparison to benchmark instruments*

A direct comparison of the analytical performance of the FT-QIT to the two benchmark systems requires careful consideration of a variety of diverse figures of merit. Outstanding analytical performance is reached with the TOFWERK CTOF coupled with micro-plasma based ionization, especially with regard to sensitivity (LOD  $< 10$  pptV toluene). The upstream pressure for these investigations, however, is with  $\sim 500$  mbar significantly higher than in the operation modes of the QIT. How far analytical performance can be maintained with the TOF system when lowering the upstream pressure needs further investigation. The quadrupole based RGA system of MKS performs as expected by the given specifications, reaching nominal mass resolution and LODs in the range of 1 ppbV for toluene in nitrogen. The RGA system allows the acquisition of selected mass range windows, which strongly reduces measurement time. In addition the obtained mass spectra are searchable in databases such as the NIST mass spectral database, since 70 eV electron ionization is strictly applied. The current analytical performance of the FT-QIT system has been summarized further above. It is expected that this performance will be strongly enhanced in the near future due to the targeted application of

e.g. SWIFT pulses and a precise determination of the actual ion trap load. For both benchmark instruments a degradation of the device surfaces is expected due to continuous exposition in e.g. hydrogen atmosphere. It is noted though that this issue is generally less important for these devices, since the analyzer region is constantly kept at high vacuum conditions. Table 13 summarizes the currently achievable performance of the three systems.

Table 13: Summary of analytical specifications of the benchmark instruments and the FT-QIT.

	<b>Tofwerk CTOF</b>	<b>MKS RGA</b>	<b>Zeiss FT-QIT</b>
<b>Considered setup</b>	Upstream pressure: 500 mbar; $\mu$ -plasma based ionization source in PT and CT mode	Upstream pressure: 500 mbar; 70 eV electron ionization	Upstream pressure: 10 mbar; In-trap electron ionization; Pulsed gas inlet
<b>Mass range</b>	10 – 300	1 – 300	10 – 200
<b>Mass resolution</b>	1000	Nominal mass	> 5000
<b>LOD</b>	< 10 pptV toluene	~ 1 ppbV toluene	< 1 ppbV toluene
<b>Measurement time</b>	30 s accumulation	3 ms per data point	max. 30 s
<b>Linear dynamic range</b>	5 orders of magnitude	> 4 orders of magnitude	> 4 orders of magnitude
<b>Robustness against corrosive gases</b>	Not known	Not known	Inert surfaces, robust against corrosives
<b>Special feature</b>	Ion transfer with Notch filter for removal of background/matrix ions	Spectra comparable to databases; short measurement time for small mass ranges	SWIFT for removal of background/matrix ions, possible repeated excitation of same ion population



## 6. Outlook

The results presented in this work allowed a critical evaluation of the performance and the characteristics of the FT-QIT in the current setup. Nonetheless further investigations are necessary.

SWIFT is a very promising tool for the application during ion storage phase and especially for ion excitation. However, SWIFT theory and the related calculations and simulations rely on ideal trap operating conditions. How far SWIFT theory can be transferred to the real system including the pulsed gas inlet calls for further in-depth studies. For this purpose the in-situ determination of the total ion load within the trap is required. Such a tool would allow experiments showing whether or not SWIFT actually leads to ion removal. The accurate determination of the total ion load is equally important with regard to the realization of a pre-scan feature. In future experiments a pre-scan may be used to actively control the ion load largely avoiding space charge induced effects. According to the trap load, ionization time, electron emission current or sample pressure can be adjusted. In addition, a comparison of results obtained from simulations and measured total ion loads allows the determination of acceptable maximum charge loads of the ion trap.

For quantitative measurements constant measurement conditions are necessary. This includes a constant electron emission current. A decrease of the electron emission current due to the addition of e.g. O<sub>2</sub> as presented in this work is not acceptable. Hence an active control of the electron emission current needs to be integrated in future devices.

It is assumed that the analytical performance can be strongly enhanced by the coupling of external ionization sources via an ion transfer stage to the QIT, since more controllable operational conditions can be applied. The coupling of an ion transfer stage will fairly compromise the compactness of the entire setup and it will depend on the application whether or not the resulting larger footprint is tolerable. If however an increased footprint can be tolerated different setups are conceivable based on a modular structure with the QIT chamber as main module.

Considering EI as favored ionization method, external electron ionization may be a solution for a number of applications. This requires the coupling of an upstream chamber held at constant pressure (approx.  $10^{-4}$  mbar) and necessitates ion transfer into the QIT. This

constitutes a significant advantage, as the gas load is strongly reduced and especially the charge load is controlled, allowing a trap operation at optimum conditions. In addition, since the electron energy is then adjustable the acquisition of mass spectra comparable to 70 eV databases is possible.

Enabling the utilization of a wider compendium of ionization methods as for example API based ion sources will certainly ask for more sophisticated ion transfer stages. The appropriate delivery of ions into the ion trap as well as the removal of e.g. matrix ions within the ion transfer stage will then be the most demanding tasks. However, an efficient ionization method and the removal of large ion ensembles within the transfer will enable FT-QIT operation under reasonable pressure conditions and without suffering from noticeable space charge effects. Hence, sensitive measurements with favorable mass resolution become feasible.

Since ion detection within the FT-QIT is non-destructive, the ion population remains in the trap, which may allow post ionization treatments of the primarily generated ion population with e.g. subsequent in-trap electron excitation. Thus, targeted fragmentation of primary generated ions may be feasible, potentially providing structural information.

## 7. Indexes

### 7.1. List of Figures

Figure 1:	Ionization cross sections determined for the ionization of CH <sub>4</sub> with electron impact [18].....	4
Figure 2:	Schematic of a linear quadrupole analyzer [9].....	10
Figure 3:	Left: Stability diagram [53]; right: Enlargement of stability diagram (reproduced from [56]).....	11
Figure 4:	Potential curve inside the quadrupole ion trap (reproduced from [70]).....	14
Figure 5:	Zoom into the stability diagram [68].....	16
Figure 6:	Photograph of the ion trajectories of charged particles in a quadrupole ion trap [72].....	17
Figure 7:	CEM in either a) straight or b) bended form [57]. ....	19
Figure 8:	Different varieties of MCPs. Left: Single MCP. Center: Chevron plate. Right: z-stack configuration [57]. ....	19
Figure 9:	Cutaway of the commercial Orbitrap from Thermo Fisher Scientific [83]. ....	23
Figure 10:	Number of transistors on newly developed processor chips in dependence of the launched year - in accordance with Moore's Law [90].....	25
Figure 11:	Schematic of Czochralski technique for growing of Si single crystals [92]. ....	27
Figure 12:	Process flow for the fabrication of an IC. Reproduced from [100]. ....	28
Figure 13:	Flow chart of the photolithography multi-step process. ....	30
Figure 14:	MKS Microvision 2 residual gas analyzer [140].....	40
Figure 15:	Schematic of the custom CTOF interface. ....	42
Figure 16:	Schematic of the capillary based analyte inlet to the ion source enabling measurements in CT and PT mode [142].....	43
Figure 17:	Signal response of toluene [M+H] <sup>+</sup> in dependence of the analyte mixing ratio. The ratio of CT vs PT products observed for xenon and toluene are plotted on the secondary axis [143].....	44
Figure 18:	Photograph of the ion trap with gold coated surfaces [145]. ....	46
Figure 19:	Photographs of the two applied gas inlet designs. Left: Bended metal tube pointing towards the hole in the endcap electrode. Right: Straight ceramic tube pointing towards the hole in the ring electrode.....	48
Figure 20:	Schematic of the measurement sequence in sample gas mode (top) and residual gas mode (bottom). ....	50
Figure 21:	Exemplary SWIFT signal for the excitation of a desired frequency range. Duration of the entire signal is 13 ms.....	51
Figure 22:	Screenshot of the GUI of the measurement software GammaProto. ProtoBox Setup is not displayed. ....	53
Figure 23:	Dependency of the excitation rate on the ion frequency for a 2 μs (blue) and a 4 μs (red) rectangular excitation pulse.....	55
Figure 24:	Schematic of the plasma source - QIT coupling [150].....	56

Figure 25:	Sketch of the response curve of the charge state amplifier. ....	60
Figure 26:	Linear regression line for calibration of ADC ratio and ADC offset yielding the mass calibration input data. ....	62
Figure 27:	Dependence of the analyte signal intensities for toluene on the focus voltage...	64
Figure 28:	Color map of the simulated ion signal response depending on the focus voltage (y-axis) and the RF voltage (x-axis) for a single oscillation of the trapping field [151]. ....	64
Figure 29:	Dependence of the analyte signal int. for toluene on the electron energy.....	65
Figure 30:	Selected electron trajectory simulations showing the modulation of the electron beam within a single RF oscillation. Orange color: $E_{kin} > 70$ eV. Light blue color: $E_{kin} 30 - 70$ eV. Dark blue color: $E_{kin} < 30$ eV. ....	66
Figure 31:	Influence of the trapping field voltage on the signal abundance of m/z 18 in a residual gas measurement. The loss in the ion signal is addressed to dips in the stability diagram. ....	67
Figure 32:	Signal intensity of $N_2^+$ (m/z 28) and $O_2^+$ (m/z 32) in dependence of the RF amplitude. Left: Uncorrected data. Right: Corrected data with respect to excitation rate and linearity of the charge state amplifier. Ratio of $O_2^+/(N_2^++O_2^+)$ is plotted on the secondary axis. ....	68
Figure 33:	Corrected signal intensities of m/z 28 and m/z 32 in dependence of the Dehmelt voltage. ....	69
Figure 34:	Left: Recorded ion signal abundances for m/z 28 and m/z 32 in dependence on the length of the excitation pulse, showing a constant relative abundance of m/z 32 over a wide range. Right: Calculated excitation rate for m/z 28 and m/z 32 in dependence of the length of the excitation pulse. ....	70
Figure 35:	Measured ion signal intensity for toluene in dependence on the length of the EI ionization pulse. ....	71
Figure 36:	Ion signal intensity for toluene in dependence on the filament current. ....	72
Figure 37:	Signal intensity of nitrogen and oxygen with $X(O_2)=0.8$ and an ionization of a) 5 ms and b) 35 ms. Signal intensity of nitrogen and oxygen with $X(O_2)=0.2$ and an ionization of c) 5 ms and d) 40 ms. ....	73
Figure 38:	Signal intensities for m/z 28 and m/z 32 in dependence of the length of the ionization pulse. ....	74
Figure 39:	Signal intensity of toluene (primary axis) and m/z ratio of the ion peak (secondary axis) in dependence of the length of the ionization pulse. ....	75
Figure 40:	Mass signal shift for the toluene $[M-H]^+$ at m/z 91 while varying the filament current. ....	76
Figure 41:	Signal intensity for m/z 28 and m/z 32 in dependence of the delay time until ion excitation. ....	77
Figure 42:	Signal intensity for m/z 28 and m/z 32 in dependence of the nitrogen/oxygen mixing ratio. ....	79
Figure 43:	Left: Ion signal intensity for toluene in dependence on the length of the EI ionization pulse with application of SWIFT. Right: Zoom into the dependency at short ionization times. ....	80
Figure 44:	Signal intensity of the toluene $[M-H]^+$ in dependence of the filament current with (orange trace) and without (blue trace) the application of SWIFT signals. ....	81

Figure 45:	Signal intensities of krypton diluted in nitrogen at a) 10 ppmV, b) 1 ppmV and c) 100 ppbV without the application of SWIFT and d), e) and f) with the application of SWIFT.....	82
Figure 46:	Observed mass shift in dependence of the length of the ionization pulse with and without the application of SWIFT.....	84
Figure 47:	Observed mass shift in dependence of the filament current with and without the application of SWIFT. ....	84
Figure 48:	Pressure profile measured with the pressure gauge for a 20 ms gas inlet with 2.5 mbar upstream pressure. ....	86
Figure 49:	Ion signal intensity profile at m/z 91 and m/z 92 upon application of a 20 ms gas pulse from 2.5 mbar. ....	87
Figure 50:	Left: Normalized signal abundance and pressure profile plotted on the same time scale. Right: Normalized signal abundance and a 10 ms shifted normalized pressure profile.....	87
Figure 51:	Analyte ion signal response (left) and pressure data response (right) in dependence of the length of the gas inlet pulse.....	88
Figure 52:	Normalized analyte ion signal response (left) and normalized pressure data response (right) in dependence of the length of the gas inlet pulse.....	89
Figure 53:	Comparison of the ion signal intensity and shifted pressure data for the three gas inlet pulse lengths. ....	89
Figure 54:	Transient pressure gauge data for different sample pressures. Right: Expanded region covering 0 to 0.15 s.....	90
Figure 55:	Transient normalized signal abundance and normalized shifted pressure data for different sample pressures.....	91
Figure 56:	Transient pressure gauge data recorded for different gas inlet lengths in nitrogen and hydrogen matrix, respectively.....	92
Figure 57:	Transient pressure profile with (red trace) and without (blue trace) the bended tube.....	93
Figure 58:	Left: Transient pressure gauge data recorded for different gas inlet lengths with the improved gas inlet design. Right: Logarithmic plot of the pressure gauge data shown in the left panel. Pressures $< 10^{-6}$ mbar are reached within 300 ms. ....	94
Figure 59:	Transient toluene ion signal intensities and pressure data for the improved gas inlet with 20 ms gas inlet length and 2.5 mbar upstream pressure.....	95
Figure 60:	Transient pressure gauge data for both gas inlet designs. With the bended tube the time until $p=10^6$ mbar is reached is two times longer. ....	96
Figure 61:	Transient analyte ion signal response compared for both gas inlet designs: Red trace bended tube, blue trace ceramic tube. ....	96
Figure 62:	Toluene signal intensity for m/z 91 in dependence on the upstream sample pressure. ....	98
Figure 63:	Sketch of the measurement sequence adapted to the transient pressure profile inside the ion trap. ....	100
Figure 64:	Transient ion signals recorded at $10^{-8}$ mbar (left) and $10^{-6}$ mbar (right). ....	101
Figure 65:	Transient ion signal showing a larger loss rate upon ion over-excitation.....	101
Figure 66:	Typical shape of the transient ion signal upon trap overload. ....	102

Figure 67:	Mass spectrum in residual gas mode showing ion signals of water ( $m/z$ 18) and nitrogen ( $m/z$ 28).....	103
Figure 68:	Long-term trend of the resonance frequency of $m/z$ 28 in a residual gas measurement (blue trace) and of the corresponding room temperature (orange trace). .....	104
Figure 69:	$m/z$ ratios for water recorded in a residual gas measurement at constant room temperature. ....	105
Figure 70:	Observed outliers in the $m/z$ calc. compared to the measured RF voltage. ....	105
Figure 71:	Histograms of the distribution of the determined $m/z$ ratios after elimination of the outliers for the first (left) and the second (right) measurement section. ....	106
Figure 72:	Trend of the signal intensities for $m/z$ 18 in residual gas mode.....	106
Figure 73:	Mass spectrum recorded with 1 ppmV diborane diluted in $H_2$ present. ....	107
Figure 74:	Mass spectrum recorded with 100 ppbV krypton diluted in $N_2$ present. ....	108
Figure 75:	Mass spectrum recorded with 50 ppbV xenon diluted in nitrogen present. ....	109
Figure 76:	Trend of the calculated $m/z$ ratio for toluene (91 Da) over time in pulsed sampling mode. ....	110
Figure 77:	Jitter in the $m/z$ ratio for consecutive measurements. ....	111
Figure 78:	Dilution series of toluene in nitrogen using normalized signal intensities. ....	113
Figure 79:	Mass spectrum recorded with 10 ppbV toluene diluted in nitrogen present leading to $[M-H]^+$ at $m/z$ 91. ....	113
Figure 80:	Signal to noise ratio of $m/z$ 91 in dependence of the toluene mixing ratio. ....	114
Figure 81:	Double logarithmic plot of the toluene dilution series using gas inlet design I with elevated ionization times using normalized signal intensities in dependence of the toluene mixing ratio. ....	115
Figure 82:	Mass spectrum recorded with 10 ppmV (red trace) and 100 ppbV (blue trace) of toluene diluted in nitrogen present (see text for details). ....	115
Figure 83:	Relative abundances of $m/z$ 92 (blue trace) and $m/z$ 93 (red trace) in dependence of the ionization length (see text for details). ....	116
Figure 84:	Correlation plot between signal peak areas and signal intensities. Both data sets are treated with previously described ionization length normalization. ....	117
Figure 85:	Trend in the signal int. for toluene at $m/z$ 91 for consecutive measurements... ..	118
Figure 86:	Variation of the amplitude and length of the stimulus SWIFT pulse showing areas of under- and over-excitation for $m/z$ 28 (left) and $m/z$ 44 (right). ....	120
Figure 87:	Mass spectrum recorded with 100 pptV toluene in nitrogen present as obtained with micro-plasma ion trap coupling. ....	121
Figure 88:	Signal intensities and peak areas (left) and signal to noise ratio (right) in dependence of the toluene mixing ratio. ....	122
Figure 89:	Temporal evolution of toluene ion species in repeated measurement experiments, showing an increase of $m/z$ 105 simultaneously to a decrease of $m/z$ 93. One cycle represents 9 seconds. ....	123
Figure 90:	Simulation of $m/z$ 35 and $m/z$ 37 for a total of 1000 particles present without the consideration of space charge interactions. Left: Calculated transient signal. Right: Calculated frequency spectrum. ....	124

Figure 91:	Simulation of $m/z$ 35 and $m/z$ 37 for a total of 1000 particles present with the consideration of space charge factor of 10. Left: Calculated transient signal. Right: Calculated frequency spectrum. ....	125
Figure 92:	Simulation of $m/z$ 35 and $m/z$ 37 for a total of 1000 particles present with a space charge factor of 100. Left: Calculated transient signal. Right: Calculated frequency spectrum. ....	125

## 7.2. *List of Tables*

Table 1:	Typical figures of merit for TOF mass analyzer[9, 47]. ....	8
Table 2:	Typical figures of merit for double focusing sector mass analyzer[47, 51]. ....	9
Table 3:	Typical figures of merit for linear quadrupole mass analyzers[47, 60]. ....	12
Table 4:	Typical figures of merit for linear quadrupole ion traps[47, 62]. ....	13
Table 5:	Typical figures of merit for three-dimensional quadrupole ion traps[47, 61]. ....	18
Table 6:	Typical figures of merit for FT-ICR instruments[47, 77]. ....	22
Table 7:	Typical figures of merit for Orbitrap mass analyzers[10, 86]. ....	24
Table 8:	Custom gas mixtures. ....	58
Table 9:	Input data for mass calibration. ....	61
Table 10:	Mass resolution of diborane dependent ion signals for two FFT windows. ....	108
Table 11:	Mass resolution of xenon isotope signals for two FFT windows. ....	109
Table 12:	Normalization of signal intensities. ....	112
Table 13:	Summary of analyt. specifications of the benchmark instr. and the FT-QIT. ....	130

### 7.3. Literature

1. Zweigenbaum, J. ed: Mass Spectrometry in Food Safety. Humana Press, Totowa, NJ (2011).
2. Niessen, W.M.A.: The Encyclopedia of mass spectrometry Volume 8 - Hyphenated Methods. (2006).
3. Ahrens, B.D., Starcevic, B., Butch, A.W.: Detection of Prohibited Substances by Liquid Chromatography Tandem Mass Spectrometry for Sports Doping Control. Presented at the (2012).
4. Lane, S.J., Boughtflower, R., Paterson, C., Underwood, T.: Capillary Electrochromatography/Mass Spectrometry: Principles and Potential for Application in the Pharmaceutical Industry. Rapid Commun. Mass Spectrom. 9, 1283–1287 (1995).
5. de Gouw, J.A., Goldan, P.D., Warneke, C., Kuster, W.C., Roberts, J.M., Marchewka, M., Bertman, S.B., Pszenny, A.A.P., Keene, W.C.: Validation of proton transfer reaction-mass spectrometry (PTR-MS) measurements of gas-phase organic compounds in the atmosphere during the New England Air Quality Study (NEAQS) in 2002. J. Geophys. Res. Atmos. 108, 1–9 (2003).
6. Cook, K.D., Bennett, K.H., Haddix, M.L.: On-Line Mass Spectrometry: A Faster Route to Process Monitoring and Control. Ind. Eng. Chem. Res. 38, 1192–1204 (1999).
7. Arkin, C.R., Griffin, T.P., Ottens, A.K., Diaz, J.A., Follistein, D.W., Adams, F.W., Helms, W.R.: Evaluation of small mass spectrometer systems for permanent gas analysis. J. Am. Soc. Mass Spectrom. 13, 1004–1012 (2002).
8. Zeiss SMT GmbH: iTrap by ZEISS Real time process control for semiconductor processes, [https://applications.zeiss.com/C1257A4B0045C6D1/0/101B8BA12EA40109C125805E0027541C/\\$FILE/ZEISS\\_iTrap\\_e-brochure.pdf](https://applications.zeiss.com/C1257A4B0045C6D1/0/101B8BA12EA40109C125805E0027541C/$FILE/ZEISS_iTrap_e-brochure.pdf).
9. Gross, J.H.: Massenspektrometrie - Ein Lehrbuch. Springer Spektrum, Berlin, Heidelberg (2013).
10. Hoffmann, E. De, Stroobant, V.: Mass Spectrometry - Principles and Applications. John Wiley & Sons, Ltd., West Sussex (2007).
11. Grayson, M.L.: Measuring Mass from positive rays to proteins. Chemical Heritage Press, Philadelphia (2002).
12. Krebs, H.A.: Chemical Composition of Blood Plasma and Serum. Annu. Rev. Biochem. 19, 409–430 (1950).
13. Chapman, J.R.: Practical Organic Mass Spectrometry. John Wiley & Sons, Inc., Chichester (1986).
14. Hübschmann, H.-J.: Handbuch der GC/MS. Wiley-VCH Verlag GmbH & Co. KGaA, Weinheim, FRG (1996).
15. Thomson, J.J.: Rays of positive electricity and their application to chemical analyses.



- Longmans, Green and co., London (1913).
16. Dempster, A.J.: Positive Ray Analysis of Lithium and Magnesium. *Phys. Rev.* 18, 415–422 (1921).
  17. Gross, M.L., Caprioli, R.M.: *The Encyclopedia of Mass Spectrometry - Ionization Methods*. Elsevier, Oxford (2007).
  18. Mark, T.D.: Fundamental aspects of electron impact ionization. *Int. J. Mass Spectrom. Ion Phys.* 45, 125–145 (1982).
  19. Bleakney, W.: A new method of positive ray analysis and its application to the measurement of ionization potentials in mercury vapor. *Phys. Rev.* 34, 157–160 (1929).
  20. Bell, K.L., Dalgarno, A., Kingston, A.E.: Penning ionization by metastable helium atoms. *J. Phys. B At. Mol. Phys.* 1, 303 (1968).
  21. Franklin, J.L.: *Ion-Molecule Reactions Volume 2*. Butterworths, London (1972).
  22. Sholette, W.P., Muschlitz, E.E.: Ionizing Collisions of Metastable Helium Atoms in Gases. *J. Chem. Phys.* 36, 3368 (1962).
  23. Richardson, W.C., Setser, D.W.: Penning ionization optical spectroscopy: Metastable helium ( $\text{He } 2^3\text{S}$ ) atoms with nitrogen, carbon monoxide, oxygen, hydrogen chloride, hydrogen bromide, and chlorine. *J. Chem. Phys.* 58, 1809–1825 (1973).
  24. Madison, T.A., Siska, P.E.: Penning ionization and ion fragmentation of formamide  $\text{HCONH}_2$  by  $\text{He}^*$ ,  $\text{Ne}^*$ , and  $\text{Ar}^*$  in molecular beams. *J. Chem. Phys.* 131, (2009).
  25. Munson, M.S.B., Field, F.H.: Chemical Ionization Mass Spectrometry. I. General Introduction. *J. Am. Chem. Soc.* 88, 2621–2630 (1966).
  26. Bruins, A.P.: Atmospheric-pressure-ionization spectrometry mass and ionization techniques. *Trends Anal. Chem.* 13, 37–43 (1994).
  27. Carroll, D.I., Dzidic, I., Horning, E.C., Stillwell, R.N.: Atmospheric Pressure Ionization Mass Spectrometry. *Appl. Spectrosc. Rev.* 17, 337–406 (1981).
  28. Grimsrud, E.P.: Vacuum Envelope for High Pressure Mass Spectrometry Applications. *Anal. Chem.* 50, 382–384 (1978).
  29. Reinsfelder, R.E., Denton, M.B.: Theory and characterization of a separator analyzer mass spectrometer. *Int. J. Mass Spectrom. Ion Phys.* 37, 241–250 (1981).
  30. Carroll, D.I., Dzidic, I., Stillwell, R.N., Horning, E.C.: Identification of positive reactant ions observed for nitrogen carrier gas in plasma chromatograph mobility studies. *Anal. Chem.* 47, 1956–1959 (1975).
  31. Shahin, M.M.: Ionic reactions in corona discharges of atmospheric gases. *Chem. React. Electr. Discharges.* 48–58 (1969).
  32. Dzidic, I., Carroll, D.I., Stillwell, R.N., Horning, E.C.: Comparison of positive ions formed in nickel-63 and corona discharge ion sources using nitrogen, argon, isobutane, ammonia and nitric oxide as reagents in atmospheric pressure ionization mass spectrometry. *Anal. Chem.* 48, 1763–1768 (1976).

33. Anicich, V.G.: Evaluated Bimolecular Ion-Molecule Gas Phase Kinetics of Positive Ions for Use in Modeling Planetary Atmospheres, Cometary Comae, and Interstellar Clouds. *J. Phys. Chem. Ref. Data.* 22, 1469–1569 (1993).
34. Blake, R.S., Monks, P.S., Ellis, A.M.: Proton-transfer reaction mass spectrometry. *Chem. Rev.* 109, 861–896 (2009).
35. Klee, S., Brockhaus, A., Wissdorf, W., Thinius, M., Hartmann, N., Benter, T.: Development of an ion activation stage for atmospheric pressure ionization sources. *Rapid Commun. Mass Spectrom.* 29, 143–154 (2015).
36. Benter, T., Klee, S., Derpmann, V., Kersten, H., Klopotoski, S., Brockmann, K.J., O'Brien, R.: On the pivotal role of ion bound clusters in Atmospheric Pressure Ionization Mass Spectrometry. In: 60<sup>th</sup> ASMS Conference on Mass Spectrometry and Allied Topics., Vancouver (2012).
37. Constapel, M., Schellenträger, M., Schmitz, O.J., Gäb, S., Brockmann, K.J., Giese, R., Benter, T.: Atmospheric-pressure laser ionization: a novel ionization method for liquid chromatography/mass spectrometry. *Rapid Commun. Mass Spectrom.* 19, 326–36 (2005).
38. Robb, D.B., Covey, T.R., Bruins, a. P.: Atmospheric pressure photoionization: An ionization method for liquid chromatography - Mass spectrometry. *Anal. Chem.* 72, 3653–3659 (2000).
39. Syage, J.A., Hanold, K.A., Lynn, T.C., Horner, J.A., Thakur, R.A.: Atmospheric pressure photoionization. *J. Chromatogr. A.* 1050, 137–149 (2004).
40. Schiewek, R., Schellenträger, M., Mönnikes, R., Lorenz, M., Giese, R., Brockmann, K.J., Gäb, S., Benter, T., Schmitz, O.J.: Ultrasensitive determination of polycyclic aromatic compounds with atmospheric-pressure laser ionization as an interface for GC/MS. *Anal. Chem.* 79, 4135–4140 (2007).
41. Kauppila, T.J., Kersten, H., Benter, T.: The ionization mechanisms in direct and dopant-assisted atmospheric pressure photoionization and atmospheric pressure laser ionization. *J. Am. Soc. Mass Spectrom.* 25, 1870–1881 (2014).
42. Weickhardt, C., Moritz, F., Grotemeyer, J., Chemie, P., Würzburg, U.: Multiphoton ionization mass spectrometry: principles and fields of application. *Eur. Mass Spectrom.* 2, 151–160 (1996).
43. Fenn, J.B.: Electrospray wings for molecular elephants (Nobel lecture). *Angew. Chemie - Int. Ed.* 42, 3871–3894 (2003).
44. Niessen, W.M.A.: Advances in instrumentation in liquid chromatography mass spectrometry and related liquid-introduction techniques. *J. Chromatogr. AA.* 794, 407–435 (1998).
45. Cole, R.B.: Electrospray ionization mass spectrometry - Fundamentals, instrumentation & applications. Wiley Interscience, New York, NY (1997).
46. Nier, K.A., Yergey, A.L., Gale, P.J.: The Encyclopedia of Mass Spectrometry - Historical Perspectives. Elsevier, Oxford (2016).

47. Hart-Smith, G., Blanksby, S.J.: Mass analysis. In: *Mass Spectrometry in Polymer Chemistry*. Wiley-VCH Verlag GmbH & Co. KGaA, Weinheim (2012).
48. Cotter, R.J.: *Time-of-Flight Mass Spectrometry Instrumentation and Applications in Biological Research*. ACS Professional Reference Books, Washington DC (1997).
49. Guilhaus, M.: Principles and Instrumentation in Time-of-flight Mass Spectrometry. *J. Mass Spectrom.* 30, 1519–1532 (1995).
50. Mamyrin, B.A., Karataev, V.I., Shmikk, D. V, Zagulin, V.A.: The mass-reflectron, a new nonmagnetic time-of-flight mass spectrometer with high resolution. *Sov. Phys. - JETP*. 37, 45–48 (1973).
51. Holland, J.F., Enke, C.G., Pinkston, J.D., Newcome, B., Watson, J.T.: Mass Spectrometry on the Chromatographic Time Scale: Realistic Expectations. *Anal. Chem.* 55, 997A–1012A (1983).
52. March, R.E., Todd, J.F.J.: *Quadrupole Ion Trap Mass Spectrometry*. John Wiley & Sons, Inc., Hoboken, NJ, USA (2005).
53. Dawson, P.: Quadrupole Mass Analysers: Performance, design and some recent applications. *Mass Spectrom. Rev.* 5, 1–37 (1986).
54. Miller, P.E., Denton, M.B.: The quadrupole mass filter: Basic operating concepts. *J. Chem. Educ.* 63, 617 (1986).
55. Mathieu, E.: Mémoire sur le mouvement vibratoire d'une membrane de forme elliptique. *J. Math. Pures Appliquées*. 13, 137–203 (1868).
56. Paul, W.: Electromagnetic Traps for Charged and Neutral Particles(Nobel Lecture). *Angew. Chemie Int. Ed. English*. 29, 739–748 (1990).
57. Gross, J.H.: *Mass Spectrometry: A Textbook*. Springer Berlin / Heidelberg (2004).
58. Ekroos, K., Chernushevich, I. V., Simons, K., Shevchenko, A.: Quantitative profiling of phospholipids by multiple precursor ion scanning on a hybrid quadrupole time-of-flight mass spectrometer. *Anal. Chem.* 74, 941–949 (2002).
59. McLafferty, F.: Tandem mass spectrometry. *Science* (80-. ). 214, 280–287 (1981).
60. MKS Instruments: *Microvision 2 Stability, accuracy and speed - The RGA your process can rely on. User Manual* (2009).
61. Douglas, D.J., Frank, A.J., Mao, D.: Linear ion traps in mass spectrometry. *Mass Spectrom. Rev.* 24, 1–29 (2005).
62. Hager, J.W.: A new linear ion trap mass spectrometer. *Rapid Commun. Mass Spectrom.* 16, 512–526 (2002).
63. Schwartz, J.C., Senko, M.W., Syka, J.E.P.: A two-dimensional quadrupole ion trap mass spectrometer. *J. Am. Soc. Mass Spectrom.* 13, 659–669 (2002).
64. Paul, W., Steinwedel, H.: Ein neues Massenspektrometer ohne Magnetfeld. *Zeitung für Naturforsch.* 8a, 448–450 (1953).
65. Paul, W., Steinwedel, H.: Apparatus for separating charged particles of different

- specific charges, (1960).
66. March, R.E.: An Introduction to Quadrupole Ion Trap Mass Spectrometry. *J. Mass Spectrom.* 32, 351–369 (1997).
  67. March, R.E.: Quadrupole ion trap mass spectrometry: theory, simulation, recent developments and applications. *Rapid Commun. Mass Spectrom.* 12, 1543–1554 (1998).
  68. Wong, P.S., Cooks, R.G.: Ion Trap Mass Spectrometry. *Bioanal. Syst.* 16, 85–92 (1997).
  69. March, R.E.: Quadrupole ion traps. *Mass Spectrom. Rev.* 28, 961–989 (2009).
  70. Aliman, M.A.: Ein Beitrag zur breitbandigen Massenspektrometrie mit elektrischen Ionenresonanzzellen (EIRZ). Dissertation, University of Wuppertal (1998).
  71. Thompson, R.I., Harmon, T.J., Ball, M.G.: The rotating-saddle trap: a mechanical analogy to RF-electric-quadrupole ion trapping? *Can. J. Phys.* 80, 1433–1448 (2002).
  72. Wuerker, R.F., Shelton, H., Langmuir, R. V.: Electrodynamic containment of charged particles. *J. Appl. Phys.* 30, 342–349 (1959).
  73. Koppelaar, D.W., Barinaga, C.J., Denton, M.B., Sperline, R.P., Hieftje, G.M., Schilling, G.D., Andrade, F.J., Barnes, J.H., IV, I.: MS Detectors. *Anal. Chem.* 77, 418 A–427 A (2005).
  74. Ladislav Wiza, J.: Microchannel plate detectors. *Nucl. Instruments Methods.* 162, 587–601 (1979).
  75. Jackson, G., Marshall, A.G., Hendrickson, C.L., Jackson, G.S.: Fourier transform ion cyclotron resonance mass spectrometry : a primer. *Mass Spectrom. Rev.* 17, 1–35 (1998).
  76. Hendrickson, C.L., Quinn, J.P., Kaiser, N.K., Smith, D.F., Blakney, G.T., Chen, T., Marshall, A.G., Weisbrod, C.R., Beu, S.C.: 21 Tesla Fourier Transform Ion Cyclotron Resonance Mass Spectrometer: A National Resource for Ultrahigh Resolution Mass Analysis. *J. Am. Soc. Mass Spectrom.* 26, 1626–1632 (2015).
  77. Ghaste, M., Mistrik, R., Shulaev, V.: Applications of fourier transform ion cyclotron resonance (FT-ICR) and orbitrap based high resolution mass spectrometry in metabolomics and lipidomics. *Int. J. Mol. Sci.* 17, (2016).
  78. Zubarev, R.A., Makarov, A.: Orbitrap Mass Spectrometry. *Anal. Chem.* 85, 5288–5296 (2013).
  79. Hu, Q., Noll, R.J., Li, H., Makarov, A., Hardman, M., Cooks, R.G.: The Orbitrap: A new mass spectrometer. *J. Mass Spectrom.* 40, 430–443 (2005).
  80. Knight, R.D.: Storage of ions from laser-produced plasmas. *Appl. Phys. Lett.* 38, 221–223 (1981).
  81. Makarov, A.: Electrostatic Axially Harmonic Orbital Trapping: A High-Performance Technique of Mass Analysis. *Anal. Chem.* 72, 1156–1162 (2000).
  82. Makarov, A., Denisov, E., Kholomeev, A., Balschun, W., Lange, O., Strupat, K., Horning, S.: Performance Evaluation of a Hybrid Linear Ion Trap / Orbitrap Mass Spectrometer. *Anal. Chem.* 78, 2113–2120 (2006).

83. Scigelova, M., Makarov, A.: Orbitrap mass analyzer - Overview and applications in proteomics. *Proteomics*. 1, 16–21 (2006).
84. Perry, R.H., Cooks, R.G., Noll, R.J.: Orbitrap mass spectrometry: Instrumentation, ion motion and applications. *Mass Spectrom. Rev.* 27, 661–699 (2008).
85. Michalski, a., Damoc, E., Lange, O., Denisov, E., Nolting, D., Muller, M., Viner, R., Schwartz, J., Remes, P., Belford, M., Dunyach, J.-J., Cox, J., Horning, S., Mann, M., Makarov, A.: Ultra High Resolution Linear Ion Trap Orbitrap Mass Spectrometer (Orbitrap Elite) Facilitates Top Down LC MS/MS and Versatile Peptide Fragmentation Modes. *Mol. Cell. Proteomics*. 11, (2012).
86. Wieghaus, A., Makarov, A., Froehlich, U., Kellmann, M., Denisov, E., Lange, O.: The Thermo Scientific Exactive Benchtop LC/MS Orbitrap Mass Spectrometer. <https://appslab.thermofisher.com/App/3240/thermo-scientific-exactive-benchtop-lcms-orbitrap-mass-spectrometer>. (2017).
87. May, G.S., Spanos, C.J.: *Fundamentals of semiconductor manufacturing and process control*. John Wiley & Sons, Inc., Hoboken, NJ, USA (2006).
88. Moore, G.E.: Cramming more components onto integrated circuits, Reprinted from *Electronics*, volume 38, number 8, April 19, 1965, pp.114 ff. *IEEE Solid-State Circuits Newsl.* 20, 33–35 (2006).
89. Schaller, R.R.: Moore’s law: past, present and future. *Spectrum, IEEE*. 34, 52–59 (1997).
90. ASML: Moore’s Law: [https://www.asml.com/enabling-innovation/kr/s45818?dfp\\_fragment=stratman\\_2](https://www.asml.com/enabling-innovation/kr/s45818?dfp_fragment=stratman_2). Accessed on 2017-03-11.
91. Binnewies, M., Finze, M., Jäckel, M., Schmidt, P., Willner, H., Rayner-Canham, G.: *Allgemeine und Anorganische Chemie*. Springer Berlin Heidelberg, Berlin, Heidelberg (2016).
92. Yu, P.Y., Cardona, M.: *Fundamentals of semiconductors: physics and materials properties*. Springer Berlin / Heidelberg (2005).
93. Koehler, A., Baessler, H.: *Electronic Processes in Organic Semiconductors: An Introduction*. Wiley-VCH Verlag GmbH & Co. KGaA, Weinheim (2015).
94. Wellmann, P.: *Materialien der Elektronik und Energietechnik*. Springer Fachmedien Wiesbaden, Wiesbaden (2017).
95. Huebener, R.: *Leiter, Halbleiter, Supraleiter*. Springer Berlin Heidelberg, Berlin, Heidelberg (2017).
96. Rahman, M.F., Patterson, D., Cheok, A., Betz, R.: *Power Electronics Handbook*. Elsevier, Oxford (2011).
97. Czochralski, J.: Ein neues Verfahren zur Messung der Kristallisationsgeschwindigkeit der Metalle. *Z. Phys. Chemie*. 92, 219–221 (1918).
98. Weiner, M.E., Lassota, D.T., Schwartz, B.: Liquid Encapsulated Czochralski Growth of GaAs. *J. Electrochem. Soc.* 118, 301 (1971).
99. Cheuvar, P., El-Hanani, U., Schneider, D., Triboulet, R.: Cdte and CdZnTe crystal

- growth by horizontal bridgman technique. *J. Cryst. Growth.* 101, 270–274 (1990).
100. Quirk, M., Serda, J.: *Semiconductor Manufacturing Technology Instructor's Manual.* Prentice Hall, Upper Saddle River, New Jersey (2001).
  101. Seshan, K.: *Handbook of Thin-Film Deposition Process and techniques.* Noyes Publications, Norwich, New York, USA (2002).
  102. Steigerwald, J.M., Murarka, S.P., Gutmann, R.J.: *Chemical Mechanical Planarization of Microelectronic Materials.* Wiley-VCH Verlag GmbH & Co. KGaA, Weinheim (2004).
  103. Dapkus, P.D., Manasevit, H.M., Hess, K.L., Low, T.S., Stillman, G.E.: High purity GaAs prepared from trimethylgallium and arsine. *J. Cryst. Growth.* 55, 10–23 (1981).
  104. Rai-Choudhury, P.: Epitaxial gallium arsenide from trimethyl gallium and arsine. *J. Electrochem. Soc.* 116, 1745–1746 (1969).
  105. Hampden-Smith, M.J., Kodas, T.T.: *Chemical Vapor Deposition of Metals: Part 1. An Overview of CVD Processes.* *Chem. Vap. Depos.* 1, 8–23 (1995).
  106. Joyce, B.A.: Molecular beam epitaxy. *Reports Prog. Phys.* 48, 1637–1697 (1985).
  107. Madou, M.J.: *Fundamentals of Microfabrication - The Science of Miniaturization.* CRC Press, Boca Raton (2002).
  108. Berkowski, K.L., Plunkett, K.N., Yu, Q., Moore, J.S.: Introduction to Photolithography: Preparation of Microscale Polymer Silhouettes. *J. Chem. Educ.* 82, 1365–1369 (2005).
  109. Levinson, H.J.: *Principles of Lithography.* SPIE The International Society for Optical Engineering (2005).
  110. Ito, T., Sakata, M., Yamashima, Y.: Negative resist material. Pat. US4826943A. (1989).
  111. Nojiri, K.: *Dry Etching Technology for Semiconductors.* Springer International Publishing, Cham (2015).
  112. Manos, D.M., Flamm, D.L.: *Plasma Etching.* Academic Press (1989).
  113. Williams, K.R., Muller, R.S.: Etch Rates for Micromachining Processing. *J. Micromechanical Syst.* 5, 256–269 (1996).
  114. Anders, A.: *Handbook of plasma immersion ion implantation and deposition.* John Wiley & Sons, Inc., New York, NY (2000).
  115. Williams, J.S.: Ion implantation of semiconductors. *Mater. Sci. Eng. A Struct. Mater. Prop. Microstruct. Process.* A253, 8–15 (1998).
  116. Maurice, F., Meny, L., Tixier, R.: *Microanalysis scanning electron microscopy.* Les Éditions de Physique, Orsay (1980).
  117. Chen, K.-N., Fan, A., Reif, R.: Microstructure Examination of Copper Wafer Bonding. *J. Electron. Mater.* 30, 331–335 (2001).
  118. Wagner, C., Harned, N.: EUV lithography: Lithography gets extreme. *Nat. Photonics.* 4, 24–26 (2010).

119. Wu, B., Kumar, A.: Extreme Ultraviolet Lithography. *IEEE J. Quantum Electron.* 35, 694–699 (2009).
120. Wu, B., Kumar, A.: Extreme ultraviolet lithography: A review. *J. Vac. Sci. Technol. B Microelectron. Nanom. Struct.* 25, 1743 (2007).
121. Bakshi, V.: *EUV Lithography*. SPIE & John Wiley & Sons, Inc., Bellingham / Hoboken (2009).
122. Syka, J.E.P., Fies, W. J., J.: A Fourier Transform Quadrupole Ion Trap Mass Spectrometer. In: 35 th ASMS Conference on Mass Spectrometry and Allied Topics. , Denver (1987).
123. Goeringer, D.E., Crutcher, R.I., McLuckey, S. a.: Ion Remeasurement in the Radio Frequency Quadrupole Ion Trap. *Anal. Chem.* 67, 4164–4169 (1995).
124. Soni, M., Frankevich, V., Nappi, M., Santini, R.E., Amy, J.W., Cooks, R.G.: Broad-band fourier transform quadrupole ion trap mass spectrometry. *Anal. Chem.* 68, 3314–3320 (1996).
125. Frankevich, V., Nappi, M., Santini, R.E., Amy, J.W., Cooks, R.G.: Non-destructive ion trap mass spectrometer and method. *Pat. US 5,625,186*. (1997).
126. Aliman, M., Glasmachers, A.: A Novel Electric Ion Resonance Cell Design with High Signal-to-Noise Ratio and Low Distortion for Fourier Transform Mass Spectrometry. *J. Am. Soc. Mass Spectrom.* 10, 1000–10007 (1999).
127. Cox, K.A., Cleven, C.D., Cooks, R.G.: Mass shifts and local space charge effects observed in the quadrupole ion trap at higher resolution. *Int. J. Mass Spectrom. Ion Process.* 144, 47–65 (1995).
128. Todd, J.F.J., Waldren, R.M., Mather, R.E.: The quadrupole ion store (quistor) part IX. space-charge and ion stability. a theoretical background and experimental results. *Int. J. Mass Spectrom. Ion Phys.* 34, 325–349 (1980).
129. Vedel, F., André, J.: Influence of space charge on the computed statistical properties of stored ions cooled by a buffer gas in a quadrupole rf trap. *Phys. Rev. A.* 29, 2098–2101 (1984).
130. Cleven, C.D., Cox, K.A., Graham Cooks, R., Bier, M.E.: Mass shifts due to ion/ion interactions in a quadrupole ion-trap mass spectrometer. *Rapid Commun. Mass Spectrom.* 8, 451–454 (1994).
131. Aizikov, K., Mathur, R., O'Connor, P.B.: The spontaneous loss of coherence catastrophe in fourier transform ion cyclotron resonance mass spectrometry. *J. Am. Soc. Mass Spectrom.* 20, 247–256 (2009).
132. Nikolaev, E.N., Heeren, R.M.A., Popov, A.M., Pozdnev, A. V., Chingin, K.S.: Realistic modeling of ion cloud motion in a Fourier transform ion cyclotron resonance cell by use of a particle-in-cell approach. *Rapid Commun. Mass Spectrom.* 21, 3527–3546 (2007).
133. Vladimirov, G., Hendrickson, C.L., Blakney, G.T., Marshall, A.G., Heeren, R.M.A., Nikolaev, E.N.: Fourier Transform Ion Cyclotron Resonance Mass Resolution and

- Dynamic Range Limits Calculated by Computer Modeling of Ion Cloud Motion. *J. Am. Soc. Mass Spectrom.* 23, 375–384 (2012).
134. Cooks, R.G., Cleven, C.D., Horn, L.A., Nappi, M., Well, C., Soni, M.H., Julian, R.K.: Non-destructive detection of ions in a quadrupole ion trap using a d.c. pulse to force coherent ion motion: a simulation study. *Int. J. Mass Spectrom. Ion Process.* 146-147, 147–163 (1995).
135. Nappi, M., Frankevich, V., Soni, M., Cooks, R.G.: Characteristics of a broad-band Fourier transform ion trap mass spectrometer. *Int. J. Mass Spectrom.* 177, 91–104 (1998).
136. Guan, S., Marshall, A.G.: Stored waveform inverse Fourier transform (SWIFT) ion excitation in trapped-ion mass spectrometry: Theory and applications. *Int. J. Mass Spectrom. Ion Process.* 157-158, 5–37 (1996).
137. Guan, S., McIver, R.T.: Optimal phase modulation in stored wave form inverse Fourier transform excitation for Fourier transform mass spectrometry. I. Basic algorithm. *J. Chem. Phys.* 92, 5841 (1990).
138. Guan, S.: General phase modulation method for stored waveform inverse Fourier transform excitation for Fourier transform ion cyclotron resonance mass spectrometry. *J. Chem. Phys.* 91, 775–777 (1989).
139. NIST Chemistry WebBook: <http://webbook.nist.gov/chemistry/>. Accessed March 2017.
140. MKS Instruments: <https://www.mksinst.com/product/Category.aspx?CategoryID=91>. Accessed March 2017.
141. TOFWERK CTOF: <http://www.tofwerk.com/ctof/>. Accessed March 2017.
142. Brockmann, K., Mueller, D., Brachthaeuser, Y., Kersten, H., Benter, T., von Keudell, A., Kuschel, T., Boeke, M., Winter, J., Aliman, M., Fedosenko, G., Reuter, R., Laue, A., Derpmann, V., Chung, H.Y.: A helium metastable seeded secondary plasma in the low mbar pressure regime - characterization and evaluation for mass spectrometric applications. In: 63<sup>rd</sup> Annual ASMS Conference on Mass Spectrometry and Allied Topics 2015 (2015).
143. Müller, D., Brachthäuser, Y., Kersten, H., Brockmann, K., Benter, T., Aliman, M., Fedosenko, G., Reuter, R., Laue, A., Derpmann, V., Chung, H.Y.: Proton Transfer Mass Spectrometry (PT-MS) with H<sub>3</sub><sup>+</sup> as reagent ions. In: 63<sup>rd</sup> Annual ASMS Conference on Mass Spectrometry and Allied Topics 2015 (2015).
144. Müller, D.: Currently unpublished dissertation. Bergische Univ. Wuppertal. (2017).
145. Brockhaus, A.: Proprietary report on SWIFT. (2015).
146. Valve, S.A.: <https://www.swagelok.com/downloads/WebCatalogs/en/MS-02-301.pdf>. Accessed March 2017.
147. Goodman, S., Hanna, A.: Method and Apparatus for producing an arbitrary excitation spectrum for Fourier transform mass spectrometry. Pat. US4945234. (1990).
148. Laue, A.P.: Sekundärionenmassenspektrometer für Elektronenmikroskope. Der andere Verlag, Uelvesbüll (2015).



149. Heintze, J., Bock, P.: Lehrbuch zur Experimentalphysik - Band 3: Elektrizität und Magnetismus. SpringerSpektrum, Berlin, Heidelberg (2016).
150. Brachthäuser, Y., Müller, D., Kersten, H., Brockmann, K., Benter, T., Aliman, M., Fedosenko, G., Reuter, R., Laue, A., Derpmann, V., Chung, H.Y.: Micro-plasma based pulsed direct charge transfer stage coupled to a FT-IT mass spectrometer. In: 63<sup>rd</sup> Annual ASMS Conference on Mass Spectrometry and Allied Topics 2015. p. 105 (2015).
151. Wissdorf, W.: Personal Communication. (2017).
152. Strohm, M., Hassman, M., Košata, B., Kodíček, M.: mMass data miner: an open source alternative for mass spectrometric data analysis. Rapid Commun. Mass Spectrom. 22, 905–908 (2008).
153. Brockhaus, A.: Personal Communication. (2015).
154. Aliman, M.A.: Personal Communication. (2015).
155. Guidugli, F., Traldi, P.: A phenomenological description of a black hole for collisionally induced decomposition products in ion-trap mass spectrometry. Rapid Commun. Mass Spectrom. 5, 343–348 (1991).
156. Guidugli, F., Traldi, P., Franklin, A.M., Langford, M.L., Murrell, J., Todd, J.F.J.: Letter to the editor. Rapid Commun. Mass Spectrom. 6, 229–231 (1992).
157. Alheit, R., Hennig, C., Morgenstern, R., Vedel, F., Werth, G.: Observation of instabilities in a Paul trap with higher-order anharmonicities. Appl. Phys. B Lasers Opt. 61, 277–283 (1995).
158. Dawson, P.H., Whetten, N.R.: Non-Linear Resonances in Quadrupole Mass Spectrometers Due To Imperfect Fields I. the Quadrupole Ion Trap. Int. J. Mass Spectrom. Ion Phys. 2, 45–59 (1969).
159. March, R.E.: Quadrupole ion trap mass spectrometry: a view at the turn of the century. Int. J. Mass Spectrom. 200, 285–312 (2000).
160. Electron impact cross sections for N<sub>2</sub> and O<sub>2</sub>: <http://physics.nist.gov/PhysRefData/Ionization/molTable.html>. Accessed March 2017.
161. Anicich, V.: An index of the literature for bimolecular gas phase cation-molecule reaction kinetics. JPL Publ. 03-19. 1172 (2003).
162. Becker, J. a., Brandes, R.G.: On the Adsorption of Oxygen on Tungsten as Revealed in the Field Emission Electron Microscope. J. Chem. Phys. 23, 1323 (1955).
163. Langmuir, I., Villars, D.S.: Oxygen films on tungsten I. A study of stability by means of electron emission in presence of cesium vapor. J. Am. Chem. Soc. 53, 486–497 (1931).
164. Lide, D.R.: CRC Handbook of Chemistry and Physics, 84<sup>th</sup> Edition, 2003-2004. Handb. Chem. Phys. 53, 2616 (2003).
165. NIST diborane Spectrum: <http://webbook.nist.gov/cgi/cbook.cgi?ID=C19287457&Units=SI&Mask=200#Mass-Spec>. Accessed March 2017.

166. Kaiser, H., Specker, H.: Bewertung und Vergleich von Analysenverfahren [Validation and comparison of analytical methods.]. *Fresenius. J. Anal. Chem.* 149, 46–66 (1956).
167. Milligan, D.B., Wilson, P.F., Freeman, C.G., Meot-Ner, M., McEwan, M.J.: Dissociative Proton Transfer Reactions of  $\text{H}_3^+$ ,  $\text{N}_2\text{H}^+$ , and  $\text{H}_3\text{O}^+$  with Acyclic, Cyclic, and Aromatic Hydrocarbons and Nitrogen Compounds, and Astrochemical Implications †. *J. Phys. Chem. A* 106, 9745–9755 (2002).
168. Ausloos, P., Jackson, J.-A.A., Lias, S.G.: Reactions of benzyl ions with alkanes, alkenes, and aromatic compounds. *Int. J. Mass Spectrom. Ion Phys.* 33, 269–283 (1980).
169. Bartmess, J.E.: Gas-phase ion chemistry of 5-methylene-1,3-cyclohexadiene (o-isotoluene) and 3-methylene-1,4-cyclohexadiene (p-isotoluene). *J. Am. Chem. Soc.* 104, 335–337 (1982).
170. Kuck, D.: Mass spectrometry of alkylbenzenes and related compounds. Part I. Gas phase ion chemistry of alkylbenzene radical cations. *Mass Spectrom. Rev.* 9, 187–233 (1990).